Dynamic behavior of industrial fixed bed reactors for the manufacture of maleic anhydride

Dissertation

zur Erlangung des Doktorgrades

der Ingenieurwissenschaften

vorgelegt von

David Lesser

aus Karlsruhe

genehmigt von der Fakultät für Mathematik/Informatik und Maschinenbau

der Technischen Universität Clausthal,

Tag der mündlichen Prüfung

28.10.2016

Dekan
Prof. Dr.-Ing. Volker Wesling

Vorsitzender der Promotionskommission
Prof. Dr. rer. nat. Alfred Weber

Betreuer
Prof. Dr.-Ing. Thomas Turek

Gutachter
Prof. Dr.-Ing. Gunther Brenner
PD Dr. habil. Gerhard Mestl

Abstract

Maleic anhydride (MA) is an important intermediate in the chemical industry. It is synthesized by the catalytic oxidation of *n*-butane with air. Mainly tubular fixed bed reactors are used for this strongly exothermal reaction, where the reaction heat is removed by molten salt. The catalysts consist of vanadium phosphorous oxides (VPO) and are employed as pelletized full body shapes. The main side products of the reaction are CO and CO_2.

Even after many years of investigation, the reaction mechanism and the nature of the active sites are not fully understood. An important subject of discussion is the assumption that water interacts with the VPO surface forming separated phosphate groups. The slowly progressing loss of these phosphates from the catalyst shifts conversion and MA selectivity to commercially unattractive regions. Therefore, it is industrial practice to add several ppm of an organic phosphorous compound to the reactor feed. The distribution of the phosphorous within the catalyst bed is supported by further addition of steam.

For the investigation of these processes the inlet concentrations of water and trimethyl phosphate (TMP) were dynamically varied in experiments in an industrial-scale pilot reactor filled with full body shaped VPO catalysts. Various, partially opposing effects were observed occurring at different time scales. Variations of these feed components caused e.g. slow changes in shape and height of the forming temperature profiles and in product composition, respectively.

As reported so far, kinetic models have been derived primarily from experiments in which significant changes in catalyst activity were not observed. Additionally, there are no studies reported with TMP feed under industrial reaction conditions. Thus, the scope of this work is developing a model which is able to describe all observed effects during complete test periods of several weeks.

According to findings in the literature, a novel kinetic model for MA formation was derived which accounts for all observed interactions between TMP and water on the VPO surface. The kinetic model was integrated into a two-dimensional, heterogeneous reactor model (gPROMS®) that includes intra particle heat and mass transfer resistances, pressure drop, and radial heat transport from the catalyst bed to the cooling medium. This reactor model could be successfully applied for parameter estimations. Kinetic and heat transport parameters were adapted to the pilot reactor experiments. The model is able to describe well up to 500 h time on stream including many variations of the operating conditions. The dynamically changing activity profiles reflect the evolution of temperature profiles and product compositions in the pilot reactor with only minor deviations.

Acknowledgements

Die vorliegende Arbeit entstand im Department Selective Oxidation der Clariant Produkte Deutschland GmbH am R&D Standort in Heufeld unter der Leitung von Gerhard Mestl, in Zusammenarbeit mit dem Institut für Chemische und Elektrochemische Verfahrenstechnik der Technischen Universität Clausthal unter der Leitung von Prof. Thomas Turek. Mein Dank gilt allen Mitarbeitern der Süd-Chemie AG/Clariant Produkte Deutschland GmbH, die diese Arbeit ermöglicht haben.

Besonders bedanken möchte ich mich bei Prof. Dr. Thomas Turek für die großartige fachliche Betreuung seitens der TU Clausthal und die vielen fruchtvollen und zielführenden Diskussionen.

Weiter danke ich insbesondere Gerhard Mestl für die Bereitstellung des Themas, die vielseitige Unterstützung, die konstruktive Kritik und die ständige Bereitschaft zur Diskussion.

Die experimentellen Ergebnisse dieser Arbeit entstanden zwischen 2011 und 2014 im Katalyselabor in Heufeld und wären ohne die aktive Mithilfe der dortigen Mitarbeiter nicht möglich gewesen. Mein spezieller Dank gilt daher Gabi Donabauer, Nadine Fromm, Markus Niedermeier, Werner Pitschi und Peter Schinke, sowie dem Rest des Oxidationsteams, und weiterhin René Geiler, Mike Bacher, Stefan Hofmeister, Andi Schwimmer, Hans Bichler und Ioannis Mashas aus der Werkstatt.

Abschließend gilt mein Dank natürlich meiner Familie, meinen Freunden und Esther für die liebevolle und moralische Unterstützung.

Table of Contents

1 Introduction

Maleic anhydride (MA) is an important intermediate in the chemical industry. In 2006, the production in USA, Europe and Japan together was about 698,000 metric tons [1]. Individual plants attain production rates over 100,000 metric tons per annum. The cyclic structure of the MA molecule containing a conjugated double bond and two carboxyl groups (Fig. 1) opens a variety of opportunities for further utilization. Over half of the global demand is used for the manufacture of unsaturated polyester resins. MA is further an important intermediate in the production of agricultural chemicals and lubricant oil additives, and is also a component of several copolymers.

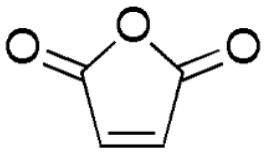

Fig. 1: Maleic anhydride molecule.

While in the past the industrial manufacture of MA was carried out by selective oxidation of benzene, today it is produced primarily by gas phase selective oxidation of *n*-butane over vanadium phosphorus oxide (VPO) catalysts [2,3]. Side products are acrylic and acetic acid with selectivities below 5 %, as well as CO and CO_2. The latter generally form by overoxidation of organic compounds, reaching selectivities in the range of 30-40 %. Reaction network and mechanism are discussed in more detail in chapter 2.

Commercial *n*-butane based manufacturing processes comprise feed preparation, reaction system and product recovery and purification [1,3]. The feed preparation includes supply systems for *n*-butane, air and promoters such as trimethyl phosphate (TMP), and water. MA in the reactor effluent is recovered by partial condensation and absorption in either aqueous or organic solvents [2,4]. Subsequent distillation finally yields purities over 99 %.

For the strongly exothermal selective oxidation of *n*-butane ($\Delta_R H°$ = -1236 kJ/mol), most widely multi tubular fixed bed reactors are used [1,2,5]. Up to 30,000 tubes are welded in a tank which contains molten salt for removal of the reaction heat. The tubes have diameters around 20-25 mm and lengths of 3-6 m. The reactor tubes contain fillings of mostly ring shaped catalyst particles, whereas the aspect ratio is rather small, in the range of 3 to 6. Because of diffusional limitations on the effective reaction rates, the selection of an adequate particle shape is determined by finding a compromise between surface area and pressure drop. Head pressures in commercial fixed bed reactors vary between 1 and 2 barg and salt bath temperatures (SBT) between 390 and 430°C. The inlet concentration of *n*-butane is typically maintained below 1.8 vol% due to reasons of explosion prevention [2], although in some cases slightly higher

values are permitted. The insufficient removal of the reaction heat by the salt bath causes the formation of hot spots in the catalyst bed with temperature differences of up to 70 K. Temperature control in the reactor is essential for economic operation since it has a major influence on the product distribution at the reactor outlet. Debt to the above mentioned network of parallel and consecutive reactions, a yield maximum arises at *n*-butane conversions around 85 %.

Beside fixed bed reactors also fluidized bed reactors are industrially applied, but to a minor extent [2,5]. Fluidized bed reactors offer the advantages of an easier temperature control and the operation with higher *n*-butane concentrations as the fluidized bed constitutes an effective flame barrier. On the other hand, back mixing effects reduce MA selectivity and further problems arise due to the high mechanical stress on the catalyst particles. An attempt to separate hydrocarbon conversion in an oxygen free atmosphere and catalyst reoxidation in air in an industrial scale transport bed reactor was fraught with difficulties and was finally abandoned in 2004 [1,5].

In this work the fixed bed technology is focused. The dominant phase of commercial VPO catalysts is vanadyl pyrophosphate (VPP), $(VO)_2P_2O_7$. Its synthesis starts with the reaction of vanadium oxide and phosphoric acid in either organic or aqueous medium, producing vanadyl hydrogen phosphate hemihydrate, $VOHPO_4 \cdot 0.5\ H_2O$ (Fig. 2) [5]. A model organic synthesis implies the formation of $VOPO_4 \cdot 2\ H_2O$ in aqueous medium which is then reduced by an alcohol in a separate step [6]. Depending on the synthesis route, VPP with different morphology is obtained. A preferred solvent is isobutyl alcohol since such organic solvents were found to have a beneficial effect on the surface area, activity and selectivity of the final catalyst. The vanadyl hydrogen phosphate hemihydrate precursor is then calcined forming VPP by elimination of water. The activation can be performed *in situ* with reaction gas or *ex situ* in hydrocarbon free atmosphere whereas temperature and gas composition have significant impact on the final catalyst structure and performance [7,8]. This aspect is more thoroughly discussed in chapter 1.

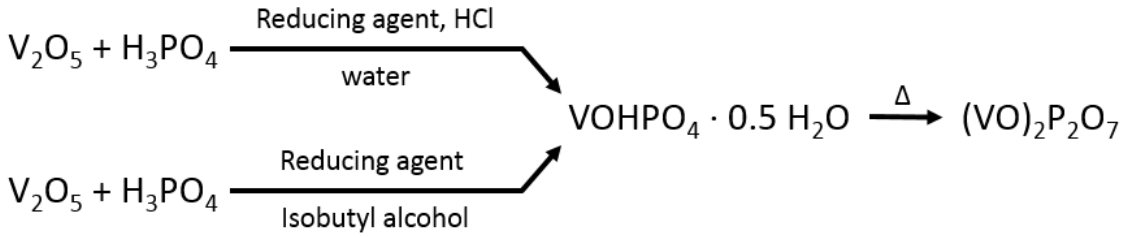

Fig. 2: Synthesis of vanadyl pyrophosphate [5].

Another important criterion in the synthesis of commercial VPO catalysts is the usage of a slight excess of phosphorus with respect to the stoichiometric amount. Resulting P/V ratios are in the

range of 1.01-1.10 [6]. Excess phosphorus affects the catalyst performance as it limits activity and increases selectivity. Since many decades reaction mechanism and nature of sites which are active in the complex conversion of *n*-butane to MA have been debated and are still not completely resolved. A thorough resume of the controversial discussions about reaction mechanism and the role of the P/V ratio is presented in chapter 1. There is also a large number of literature studies, which focus on the kinetic description of the selective *n*-butane oxidation. A variety of steady state and dynamic kinetic models have been proposed. The literature models are based on different assumptions about reaction network and mechanism, and also on the different applied reactor setups and experimental conditions. An overview is presented in chapter 3.

A number of patents reveal some important aspects of the commercial application of VPO-catalysts for the production of maleic anhydride from *n*-butane [9–13]. Apparently, the catalyst performance declines with time as its selectivity decreases with simultaneously increasing activity. As a consequence the MA yield diminishes and the reactor operation shifts towards less stable regions. Because of the general assumption that a loss of phosphorus from the catalyst is responsible for this unwanted behavior [3,12], a variety of technologies are claimed compensating this loss in order to ensure optimum operation of commercial reactors. This implies the addition of an organic phosphorus compound, such as trimethyl phosphate (TMP) to the reactor feed. Furthermore, the addition of water seems to play an important role for an adequate distribution of phosphorus in the catalyst bed [10,11]. Chapter 1 includes a more detailed discussion about this particular aspect of the commercial application of VPO catalysts for the manufacture of MA.

Despite its high industrial importance this subject hardly has been considered in the scientific literature. Previous literature models of the active VPO surface mostly are not able to account for such effects. From a commercial point of view however, the profitability of the process can be reduced significantly if the reactor is operated away from the yield optimum. Therefore, there is a big interest in a feasible mathematical description of the phosphorous dynamics in a detailed model for an industrial fixed bed reactor, which is the purpose of this work.

In the first part of the presented study the reaction network of the selective oxidation of *n*-butane to MA was investigated in a laboratory reactor under steady state conditions which minimize phosphorus related dynamic changes in performance (chapter 2). These experiments were used in order to estimate kinetic parameters (chapter 3). Applying different full body catalyst particle shapes during the kinetic experiments not only allowed to quantify the influence of pore diffusional resistances, but also to directly obtain a feasible kinetic model for different VPO catalyst shapes as they are commonly applied in industry.

The procedure of evaluating experiments with kinetic modeling was then also pursued for the phosphorus dynamics. These were investigated in an industrial scale fixed bed pilot reactor, in which commercial-like catalyst shapes were tested under typical industrial reaction conditions (chapter 1). During the experiments dynamic changes in catalyst performance were induced by addition of TMP and water. The experimental observations were discussed in the light of the

scientific literature about the reaction mechanism. The findings were further used as a base for the deduction of mathematical expressions for the phosphorus dynamics which were then implemented in a model for the applied pilot reactor (chapter 5). For the achievement of the final objective of this work, the last step was the estimation of the activity parameters by simulating the performed experiments.

2 Reaction network

Reaction network and steady state kinetics were investigated in a bench scale reactor with different full body catalyst shapes. In general full body catalyst shapes are not used for such studies since they may involve the interference by intra particle heat and mass transport. In the present study this was accepted because of the following considerations. Most commercial catalysts are ring-shaped and consist entirely of active VPO material. Due to the wall thickness of the ring shapes (> 1 mm) and small average pore diameters (<100 nm), *n*-butane conversion and product distribution are likely influenced by diffusion of the reacting compounds inside the catalyst particles. In that case, a more feasible determination of the intrinsic reaction kinetics would require micro reactor studies with crushed catalyst particles, in which the influence of pore diffusion is negligible.

The scale-up of the intrinsic reaction kinetics to more complex geometries, as are the commercial catalyst shapes, involves further the use of appropriate diffusion models. However, this is not a trivial matter due to the variety of diffusion models available in the literature, e.g. the Maxwell-Stefan relations for multicomponent systems and the more classical Fickian diffusion model. Also for the calculation of the required molecular diffusion coefficients various correlations have been presented in the literature [14,15]. Another controversial parameter is the tortuosity factor for the calculation of effective diffusion coefficients in porous systems. Typical values are between 3 and 7 [16] and have to be determined experimentally, although there are also estimation methods based on the evaluation of pore size distribution data [17].

If finally the intrinsic kinetic parameters have been determined, it is still necessary to examine experimentally if their combination with the respective diffusion models in a heterogeneous model fits well the description of the full body catalyst shapes. Although this methodology would deliver more detailed insights concerning intrinsic kinetics, pore diffusion and scale-up to industrial catalyst shapes, the additional experimental effort would go beyond the scope of this work. In the present work, the kinetic experiments were hence carried out directly with full-body catalyst shapes. The influence of pore diffusion was taken into account by applying a heterogeneous reactor model for the description of the bench scale reactor including a one-dimensional pellet model. In order to assure the validity of the applied diffusion model, different catalyst shapes were used for the experiments. Hence, this strategy permits a possible influence or falsification of the determined intrinsic kinetic parameters with the advantage of disposing directly of a kinetic model which is applicable to a variety of full body catalyst shapes as they are commercially applied.

In the following sections of this work, the below listed definitions account:

- Conversion (*X*) relates to the fraction of the introduced moles of *n*-butane which are converted to any products ($\dot{n}_i$ is the molar flow of compound *i* in moles/s)

$$X = 1 - \frac{\dot{n}_{Bu}}{\dot{n}_{Bu,0}} \quad (2\text{-}1)$$

- Selectivity of compound *i* (S_i) is the carbon based relation of product *i* to converted *n*-butane (ϵ_i is the number of carbon atoms of compound *i*)

$$S_i = \frac{\epsilon_i}{4} \frac{\dot{n}_i - \dot{n}_{i,0}}{\dot{n}_{Bu,0} - \dot{n}_{Bu}} \quad (2\text{-}2)$$

- Yield of compound *i* (Y_i) is the product of selectivity and conversion

$$Y_i = S_i \cdot X \quad (2\text{-}3)$$

- *CO/CO₂* relates to the ratio between the selectivities to CO and CO_2 respectively

$$CO/CO_2 = \frac{S_{CO}}{S_{CO_2}} \quad (2\text{-}4)$$

2.1 Literature overview

The conversion of *n*-butane to MA requires the shift of 14 electrons, the abstraction of eight hydrogen atoms, the introduction of three oxygen atoms, as well as a ring closing. Hence, it is likely the case that the reaction proceeds via a series of intermediates. However, such intermediates only have been detected under special reaction conditions, such as vacuum and high C_4/O_2-ratios, but not under conditions, which approach those of industrial reactors ($p \geq 1$ atm, $T > 350$°C) [18].

Some reaction mechanisms which have been proposed and discussed in the literature are resumed in [18]. The widest support carries the consecutive alkenyl mechanism, according to which MA is formed by adsorbed *n*-butane through a variety of adsorbed intermediates such as *n*-butenes and furan. This mechanism is also called cyclic route, as the ring closing occurs through the oxidation of butadiene to 2,5-dihydrofurane. The respective intermediates were detected by Centi *et al.* [19] and Kubias *et al.* [20] in temporal analysis of products (*TAP*) reactors which again operate far from industrial reaction conditions. Lattice oxygen is supposed to be active according to the Mars-van-Krevelen mechanism [18]. There are controversies whether the initial abstraction of hydrogen or the replenishment of oxygen is the rate determining step. Brandstädter and Kraushaar-Czarnetzki [21] found ten times higher rate constants for *n*-butene oxidation than for *n*-butane from which they concluded that the activation of *n*-butane is rate limiting. On the other hand, Cheng and Goddard [22] calculated the highest activation barrier for the ring closing step by means of density functional theory (*DFT*) modeling. Additionally,

there is uncertainty if the oxidations of *n*-butane and *n*-butenes follow the same reaction mechanism as the latter produces various detectable organic reaction products [18,23].

Another, more recently discussed mechanism is the consecutive alkoxide mechanism [18] which proceeds via more strongly adsorbed alkoxide intermediates. In this case, lattice and adsorbed oxygen were discussed as active species. A noncyclic alkoxide route was derived by Xue and Schrader [24] who carried out FTIR studies under transient conditions. Their proposed reaction scheme is shown in Fig. 3.

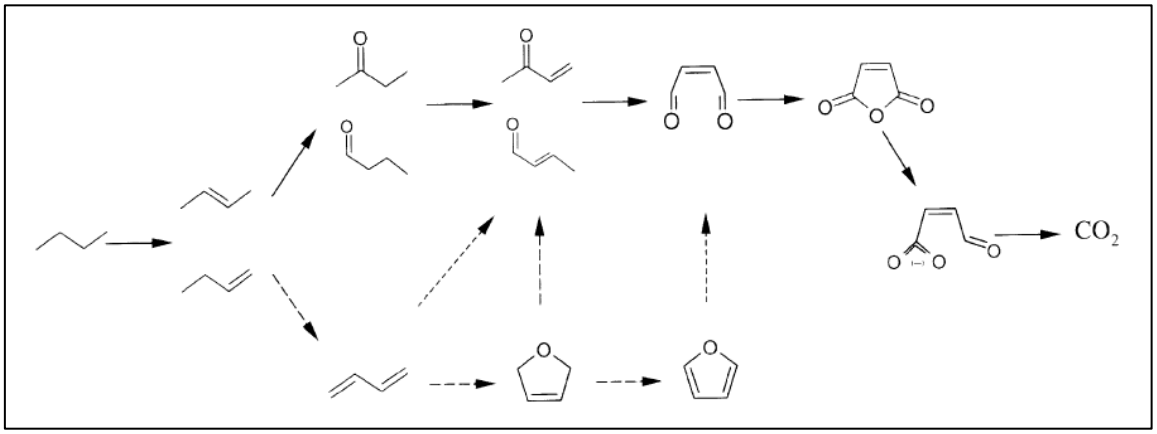

Fig. 3: Proposed reaction pathway for *n*-butane oxidation to MA [11].

Further proposed mechanisms are the concerted reaction mechanism and the redox couple mechanism [18]. The concerted mechanism is based on theoretical calculations. *n*-Butane is supposed to adsorb on the (100) plane of VPP, forming bonds which are strong enough to anchor the C_4 until the complete reaction via butadiene. The redox couple mechanism suggests the activation of *n*-butane on a V^{3+}/V^{4+}-couple, while the oxidation to MA proceeds on V^{4+}/V^{5+}-couples. This mechanism was deduced from experiments with high C_4/O_2-ratio during which alkenes were detected in the gas phase.

The main carbon containing by-products which are found under industrial reaction conditions are CO and CO_2, and in lower quantities also acrylic and acetic acid [3,25,26]. However, these compounds are most likely not intermediates in the path towards MA since their formation requires a C-C cleavage. For kinetic studies, Dente *et al.* [25] applied a reaction network which included the formation of acrylic acid and acetic acid in parallel reactions from *n*-butane, as well as their oxidation to CO and CO_2. On the other hand, Huang *et al.* [26] detected acrylic acid and acetic acid also as decomposition products of MA when oxygen and MA were co-fed.

Only few authors did also find other intermediates and by-products under conditions, which are similar to those applied in industrial reactors. During studies in a micro fixed bed reactor at 2 bar and 372-440°C with 3-12 % *n*-butane and 5-15 % oxygen, Huang *et al.* [26] detected additionally trace amounts of butene, furan, 2,5-dihydrofurane and even benzene and methylbenzene. In a

similar reactor, Hess *et al.* [27] fed 2-8 % *n*-butane in air at 400-440°C. Beside CO_x, they detected furan in the outlet gas stream with up to 10 % selectivity at low *n*-butane conversions. However, in both presented works, the additional intermediates were only observed at high *n*-butane concentrations as they may be found in fluidized bed reactors, while in fixed bed reactors the inlet concentration is usually kept below 1.8 vol%.

It is generally reported that the selectivity to MA is limited and decreases with rising *n*-butane conversion, while CO_x-formation increases [3,18]. This is debt to the presence of parallel reaction paths towards CO, CO_2, acrylic acid and acetic acid, and on the consecutive oxidation of MA to CO and CO_2 [18]. The presence of the latter was experimentally confirmed by various authors [25,26,28]. All reactions are irreversible. The relation between selectivity and conversion is qualitatively sketched in Fig. 4. Maximum MA-yields are about 50-60 mol% at around 85 % conversion [5].

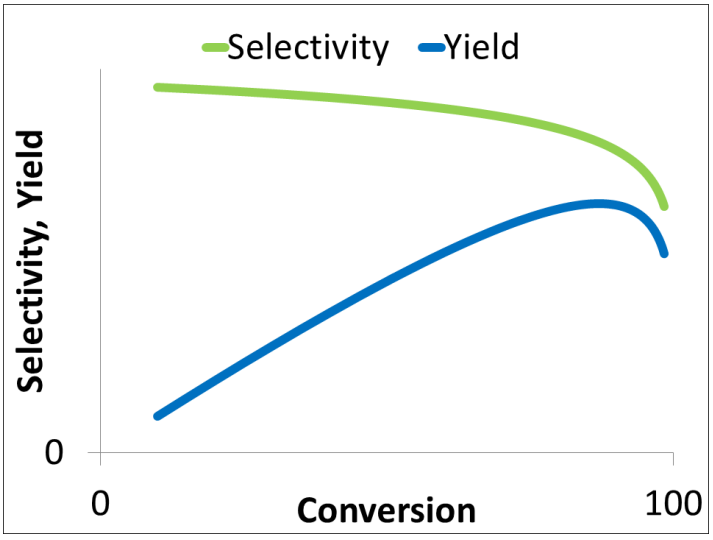

Fig. 4: Qualitative relation between MA selectivity, yield and *n*-butane conversion.

Taken into account the absence of intermediates and the uncertainty about the reaction mechanism, the selective oxidation of *n*-butane is generally described by a network of overall reactions (Fig. 5) which includes the selective reaction path, as well as the nonselective oxidations of *n*-butane and MA to CO and CO_2 [3]. Some authors even consider the oxidation of CO to CO_2 [3,29,30], although Dente *et al.* [25] did not find CO_2 in the outlet gas after feeding CO during studies in a micro fixed bed reactor. As organic by-products are formed only in minor amounts, they are generally neglected.

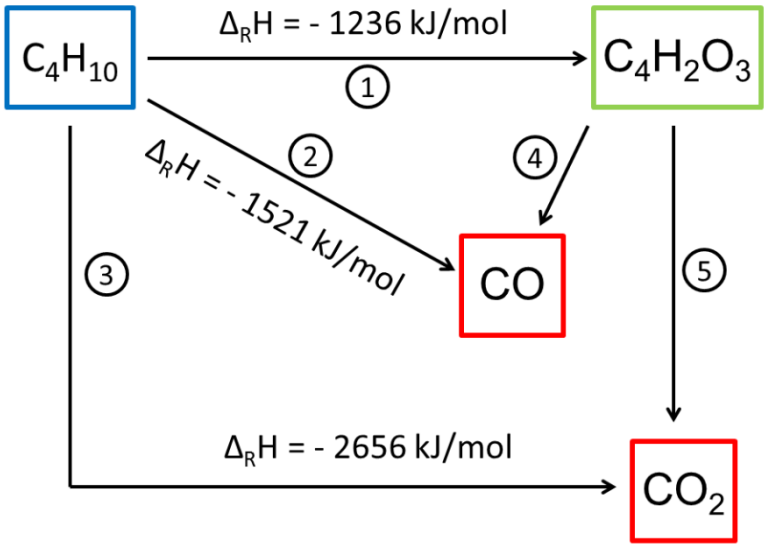

Fig. 5: Generally applied reaction network for the selective oxidation of *n*-butane.

In the literature, some discrepancies appear in the treatment of the carbon oxides. For kinetic studies, many authors lump them together into one hypothetical CO_x-species [8,31,32], obtaining the often cited triangular reaction network. Other authors, who apply this triangular network, take into account the ratio between formed CO and CO_2 as a fixed value [28] or by introducing stoichiometric parameters which are estimated experimentally [23,33,34]. In this case, the unselective side-reactions take a form as presented below [23], whereas the stoichiometric variables s_{Bu} and s_{MA} determine the relative amounts of CO and CO_2 which are produced by the unselective oxidations of *n*-butane and MA respectively. Other authors consider CO and CO_2 in separated reactions according to the scheme in Fig. 5 [35–37].

$$C_4H_{10} + (6.5 - 2\,s_{Bu})\,O_2 \rightarrow 4s_{Bu}\,CO + 4\,(1 - s_{Bu})\,CO_2 + 5\,H_2O \qquad (2\text{-i})$$

$$C_4H_2O_3 + (3 - 2s_{MA})\,O_2 \rightarrow 4s_{MA}\,CO + 4\,(1 - s_{MA})\,CO_2 + H_2O \qquad (2\text{-ii})$$

Further inconsistencies exist about the significance of the different formation paths of CO and CO_2. Contractor and Sleight [38] and Brandstädter [23] found that the oxidation of *n*-butane forms more CO than CO_2, while the decomposition of MA produces more CO_2. On the other hand, the kinetic studies of Sharma *et al.* [33] and Becker [34] suggest that the oxidation of MA produces only CO while the CO/CO_2 ratio from *n*-butane oxidation was found to be one [33] and 1/3 [34] respectively. Also Centi *et al.* [35] did not find CO at low conversions and considered its formation exclusively by oxidation of MA, while in the network of Gascón *et al.* [36], CO is only

produced by oxidation of *n*-butane. Schneider *et al.* [37] neglected the oxidation of MA completely and found higher formation rates for CO_2 than for CO.

Another issue, which strongly relates to the discussion about the formation of by-products, is the number of active sites involved and their function in the different reaction pathways. There is a considerable number of research works [6,7,28,39–43] which suggest that more than only one active site are present on the catalyst surface, and that they show different activities in the various reaction paths.

Coulston *et al.* [42] suggested that V^{5+} species may play an important role in the initial hydrogen abstraction and in the formation of MA, while V^{4+} species may be responsible for by-product formation. This concept was also partially seized by Bej and Rao [31] and Lorences *et al.* [43], who assumed in their kinetic studies that the nonselective oxidation of *n*-butane takes place on V^{4+}-sites while the selective reaction path and the decomposition of MA should occur on V^{5+}-sites. Cavani *et al.* [39,40] found different active surfaces showing different selectivities as a function of temperature and phosphorus content of the catalyst. The transient change in selectivity after treatment with water, as observed by Arnold and Sundaresan [41] and Uihlein [28], supports this assumption of different kinds of active sites. Wilkinson *et al.* [8], moreover, needed a second, different activity factor for the oxidation of MA to CO_x for their initial deactivation modeling. Centi *et al.* [44] even speculated about three types of active site for the selective and unselective oxidation of *n*-butane, and for the consecutive oxidation of MA respectively.

However, the cited works do not further distinguish between the nonselective products. Different authors could indeed identify differences in the reaction paths to CO and CO_2. Uihlein [28] found a reduced selectivity to CO at constant conversion in the presence of water. Comparable observations were reported by Contractor *et al.* [45] who found decreased CO/CO_2 ratios in the presence of water under anaerobic conditions. However, these results leave open if different surface sites are active in the formation of CO and CO_2, or in the nonselective oxidations of *n*-butane and MA, which produce constant CO/CO_2 ratios according to the triangular reaction scheme. The latter was recommended by Contractor *et al.* [45] who proposed that steam is active in stripping nonselective oxygen species from the catalyst surface, affecting preferentially the decomposition of *n*-butane, which produces more CO. On the other hand, Schlögl [46] discussed mechanistic aspects of the oxidation of propane over mixed oxides. He suggested that the formation of CO occurs on different active sites as compared to the conversion to selective oxidation products and CO_2, which may be transferred to other oxidation reactions.

Following the conclusions of Contractor *et al.* [45], various authors have also discussed about the presence and activity of different oxygen species [6,47,48]. Based on $^{18}O_2$ labeling studies, Rodemerck *et al.* [47] suggested that a strict redox mechanism operates in the selective oxidation path, while adsorbed oxygen is involved in the formation of CO_2. On the other hand, Abon *et al.* [48] concluded from similar experiments that the formation of CO_x is performed by lattice oxygen. Huang *et al.* [26] assumed in their kinetic model that only the selective reaction

requires lattice oxygen, while the formation of CO and CO_2 is carried out by adsorbed oxygen species. Other authors suggested that weakly adsorbed oxygen species may also contribute to the initial activation of *n*-butane [44]. In further kinetic studies, Gascón *et al.* [36] considered several parallel reaction paths to MA and CO_2 by adsorbed and surface lattice oxygen, while CO is formed only from the oxidation of adsorbed *n*-butane by surface lattice oxygen.

2.2 Bench reactor

Kinetic experiments were carried out in a continuous flow fixed bed reactor, which is schematically presented in Fig. 6. The core of the reactor comprises four tubes of about 1.4 m length and 21 mm inner diameter, which are welded in a stirred tank containing molten salt. Heating elements permit precise control of the salt bath temperature (SBT) between 350 and 450°C. Each tube contains an axial multi-point thermocouple of 3 mm diameter, which measures the temperature at eight points along the catalyst bed. However, the exact axial positions of the measurement sensors in the tubes are not known precisely.

The catalyst loading comprises full-body catalyst shapes, which are mixed with inert rings of 3.7/3/2 mm ($d_a/h/d_i$) in order to approach isothermal conditions. Inert sections before and after the catalyst bed ensure an optimum preheating and mixing of the reaction gas.

The feed section comprises only *n*-butane and air, but no water and no phosphorus compound. The flow rates are controlled by mass flow controllers with thermal measurement principle (Brooks). A central low pressure air system in which air is compressed to 7 bar and subsequently dried guarantees its continuous supply. *n*-Butane proceeds from a heated 70 kg-cylinder.

The outlet gas streams lead to a catalytic combustion unit, which oxidizes CO and any organic compounds to CO_2 and water before venting to the atmosphere. Branches of all inlet and outlet lines unite at one multiport valve whose outlet line connects to the analytics. In order to avoid condensation of any compounds, all lines are heated to 230°C.

The analytics comprise an infrared (IR, Emerson NGA2000) analyzer for the measurement of *n*-butane, CO and CO_2, as well as a gas chromatograph (GC, Agilent6820N with capillary column Restek RTX1701, 30 m) for the measurement of *n*-butane, MA and acrylic and acetic acid. The sample gas, which proceeds from the multiport valve, passes through a 6-port-2-position valve including a sample loop. Behind the 6/2-valve is a water flushed condenser, where any heavy organic components are precipitated at ambient temperature. Before entering the IR analyzer the gas is dried and filtered in a gas cooler. When the measurement signals in the IR analyzer are constant and the variance falls below a certain value, the 6/2-valve is automatically switched and a helium stream pushes the content of the sample loop towards the GC.

The complete control of reactor and analytics including industrial safety standards is fully automated (LabVIEW, National Instruments) and permits the control of complex experimental

sequences, ensuring non-stop operation. According to the programed experimental sequence, the reactor consecutively triggers the respective operating conditions and the composition of the outlet gas is analyzed in the IR analyzer. When steady state is reached, the control system commands the subsequent data acquisition of all reactor inlet and outlet sample lines until every sample line has been measured twice. At continuation, mass flow controllers and SBT are switched to the next operating state.

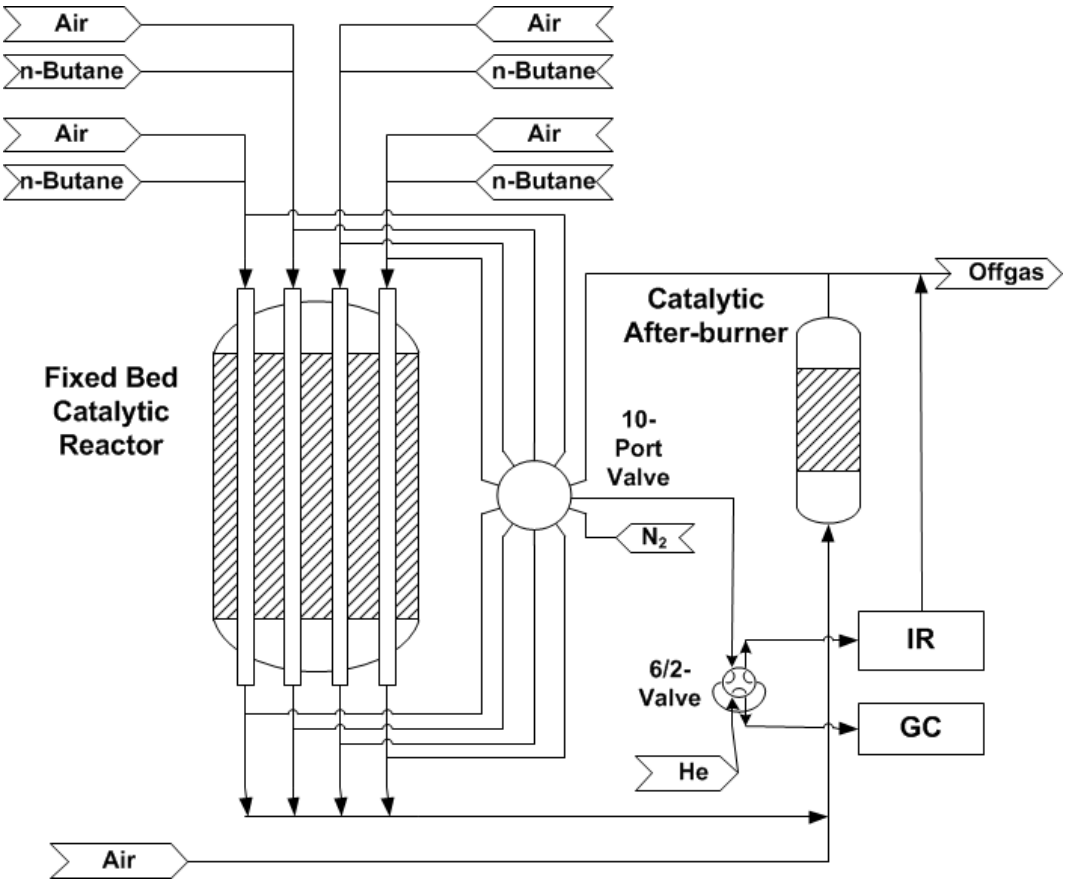

Fig. 6: Process flow diagram of the pilot reactor.

2.3 Catalysts

In total, six different cylindrical and ring shaped catalysts (*C1-C6*) were used for the kinetic experiments which were all made from the same catalyst powder. The powder was produced according to the organic synthesis route, followed by calcination in air. The activation step comprises a thermal treatment in a steam containing atmosphere. Shapes *C1* and *C2* are solid cylinders while samples *C3-C6* are ring shaped. The catalyst bodies differentiate further in

specific surface area, particle density, BET surface area and pore dimensions (Tab. 1). The mean P/V-ratio was about 1.1 and the mean oxidation state of vanadium was in the range 4.1-4.2.

Tab. 1: Normalized properties* of catalysts used for kinetic experiments

	Catalyst Shape	Normalized specific surface area	Normalized particle density	Normalized BET surface area	Normalized pore radius	Normalized pellet porosity
		$\bar{S}_v$	$\bar{\rho}_p$	$\overline{BET}$	$\bar{r}_p$	$\bar{\varepsilon}_p$
C1	Cylinder	1.0	1.0	1.0	1.0	1.0
C2	Cylinder	0.7	0.9	1.0	1.4	1.1
C3	Ring	0.9	0.9	1.0	1.5	1.1
C4	Ring	0.8	0.8	1.1	1.8	1.2
C5	Ring	0.9	0.9	1.0	1.9	1.0
C6	Ring	0.8	0.9	1.2	1.5	1.1

* The normalized value $\bar{A}_i$ of a parameter A_i is defined as the ratio between A_i and a reference value A_i^{ref}.

2.4 Experimental setup

With the catalysts presented in the previous section, four bench experiments were carried out with catalyst beds of 1 m length, which contained 5-15 wt% catalyst mixed with inert steatite particles of 3.7 mm diameter. The amounts of the different catalyst shapes in the reactor tubes differed in the tests. Varying additionally the total flow rate between 100 and 300 NL/h, the resulting mass related gas hourly space velocity ($GHSV_m$) ranged between 1800 and 14800 NL/h/kGC_{at}. The experiments were performed at pressures close to atmospheric pressure. The inlet concentration of *n*-butane and the SBT were varied between 0.7 and 2.0 vol% and 410 and 440°C, respectively.

Each test was equilibrated during a period of three days at constant operating conditions (410°C SBT, 2500 NL/h/kGC_{at} $GHSV_m$ and 1.5 vol% of *n*-butane in air). At continuation, the process conditions were varied stepwise. About 30 min after setting some new operating conditions, the inlet and outlet concentrations of the four reactor tubes were consecutively measured. After measuring the last tube, the sequence was repeated once more before changing the operating

conditions. Every time after having performed several variations of *n*-butane concentration and gas flow rate at one SBT, the equilibrating conditions were reset before switching to a new SBT, in order to identify any irreversible changes of the catalyst performance.

A frequent phenomenon in diluted catalyst beds is slipping, which means that part of the reaction gas passes through reactor sections without getting in contact with the catalyst. The effect on catalyst performance was investigated, amongst others, by Berger *et al.* [49,50]. They found that slipping may enhance the axial dispersion which leads to falsifications of the observed conversions. In order to estimate the resulting deviation (*Δ*), which should be less than 5 %, the authors proposed the following relation.

$$\Delta = \left(\frac{b}{1-b}\right) \cdot \frac{X \cdot d_P}{2L} \tag{2-5}$$

In this equation, *b* is the dilution, *X* the conversion, d_P the particle diameter and *L* the catalyst bed length. In the presented experiments, this 5 %-criterion was generally satisfied. Only in case of the highest dilution with cylinders, the deviation was up to 7 %. However, in contrast to the reactor applied in this work, Berger *et al.* [49,50] deduced their relation from experiments in a micro fixed bed with crushed catalyst particles because of which the results should be treated with caution. Another criterion for the absence of slipping is presented in [16]. In the presented experiments, also this 2nd relation (2-6) is satisfied, even for the highest dilution and an assumed experimental error (*e*) of 1 %.

$$\frac{m_{inert}}{(m_{inert}+m_{cat})} \cdot \frac{d_P}{L \cdot e} < 4 \cdot 10^{-3} \tag{2-6}$$

2.5 Experimental results

2.5.1 General aspects

The applied experimental setup and process conditions permitted an investigation of the reaction in a conversion interval from 10 to 90 %. Altogether, around 1100 data points were collected. The GC measurements showed only peaks, which can be related to *n*-butane, MA, acrylic acid and acetic acid.

Temperature measurements revealed that the average reaction temperature along the catalyst bed was up to 10°C higher than the SBT (Fig. 7), and hot spots up to 25°C were observed at high *n*-butane concentrations and SBT*s*. Hence, the applied dilution of the catalyst was not sufficient to achieve fully isothermal conditions. Furthermore, the measured inlet concentrations of *n*-

butane in each reactor tube were observed to deviate up to 0.3 vol% (absolute) as compared to the set point (Fig. 8), which has an additional effect on the resulting selectivity-conversion-plots. These aspects must be taken into account during the evaluation of experimental results.

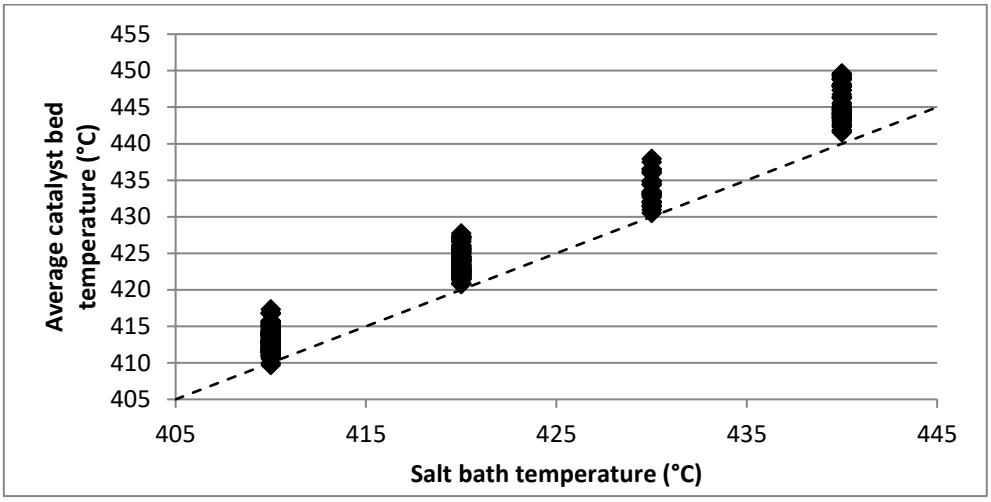

Fig. 7: Measured, average catalyst bed temperature (♦) at different salt bath temperatures (dashed line is the angle bisector).

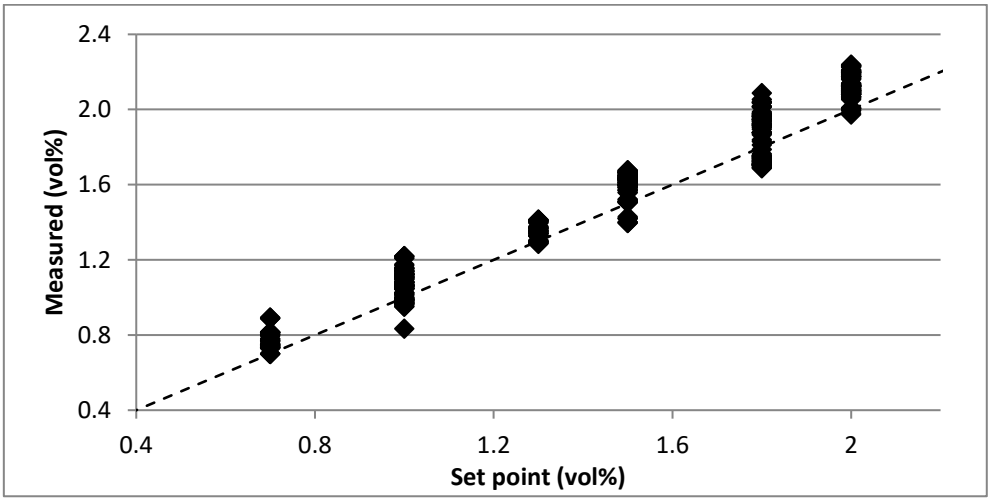

Fig. 8: Measured *n*-butane feed concentrations (♦) for different set points (dashed line is the angle bisector which represents the set point).

For the applied flow rates of 100-300 NL/h the particle related Reynolds number (2-7) at the lowest temperature (410°C) ranged between 10 and 60. At equilibrating conditions (GHSV = 2500 NL/h/kGC_{at}) however, the Reynolds number fell down to 5 in case of high catalyst dilution (5 wt%) of the *C1* sample. Fig. 9 shows the progression of conversion during the

equilibration of the 2nd test, in which three tubes were filled with 5, 10 and 15 wt% of *C1*. The respective Reynolds numbers were about 5.5, 10.1 and 12.2. While the conversion in the tubes with 10 and 15 wt% catalyst is almost equal, it is about 3 % lower in the tube which contained only 5 wt% catalyst. This indicates the presence of mass transfer limitations between gas and solid at conditions in which the Reynolds number falls below 10. However, such low Reynolds numbers appeared only during equilibration of the catalyst. Additionally, it must be taken into account that the measured inlet concentration of *n*-butane was about 0.1 vol% higher in this tube, which also should effect reduced conversions if the reaction order with respect to *n*-butane is different from one.

$$Re_P = \frac{u_z \cdot \rho_{fl} \cdot d_P}{\eta} \tag{2-7}$$

Fig. 9 and Fig. 10 show that during initial operation, the conversion generally decreased slightly while the MA selectivity increased. In the literature, the changing catalytic performance of a freshly activated catalyst during the initial operation is mostly referred to as “conditioning” or “equilibration”. A number of works on this subject are reviewed in [6–8]. It is generally assumed that the loss in activity is debt to the reduction of V^{5+}-phases to V^{4+}, obtaining highly crystallized VPP with high BET surface areas [6–8,48,51]. Wilkinson *et al.* [8] found a sharp decline in catalyst activity only during the first 5 h of operation, while the oxidation state of the catalyst started declining afterwards. In the presented bench reactor experiments it was not possible to collect more measurement data during the first 5 h of operation. Hence, the results do not serve for a suitable comparison with literature studies. A more extended discussion of that subject will follow in chapter 1.

With respect to the reproducibility measurements at equilibrating conditions, various significant deviations were observed. In some cases, the conversion continued declining throughout the test. During the 4th bench test which was carried out with ring-shaped catalysts, this was observed to a minor extent for *C6*, and more pronounced in case of *C5* (Fig. 11). Analysis of *post mortem* samples revealed reduced BET surface areas for all catalysts as compared to the fresh samples (Tab. 2), while the pellet porosity increased, except in the tube containing 7 % of *C6*. No significant changes in the elemental compositions were found. The slightly reduced oxidation state of vanadium is debt to the reduction of the catalyst under reaction conditions.

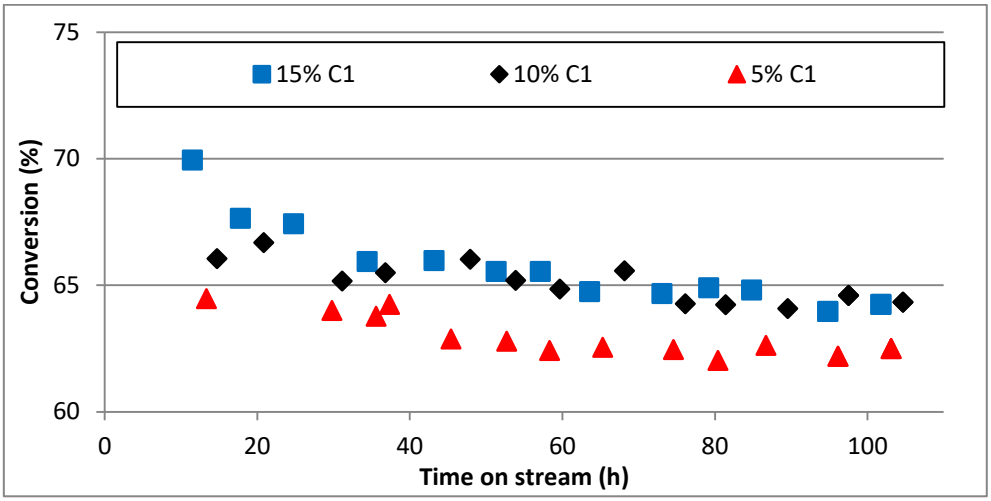

Fig. 9: *n*-Butane conversion during equilibration of the 2nd bench test loaded with 5, 10 and 15 wt% of catalyst *C1*.

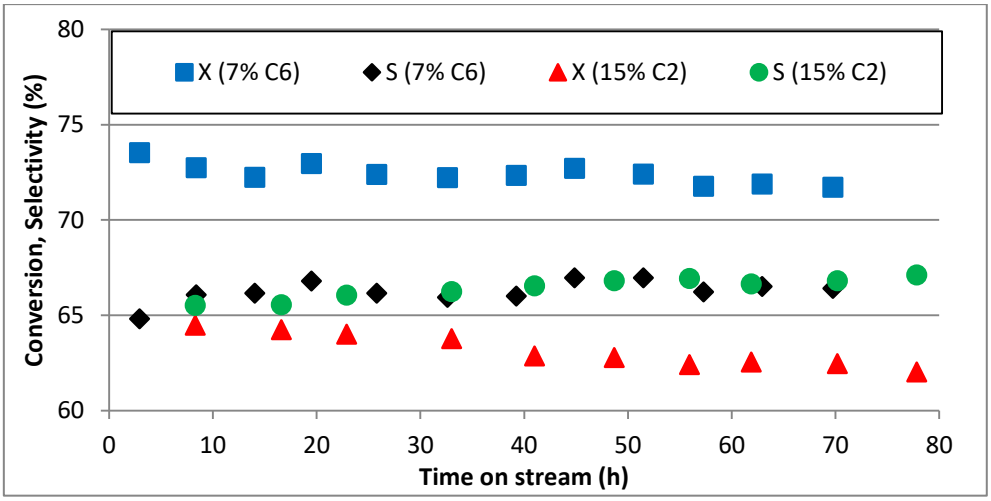

Fig. 10: Catalyst performance during equilibration of two bench tests loaded with 7 wt% *C6* and 15 wt% *C2* respectively.

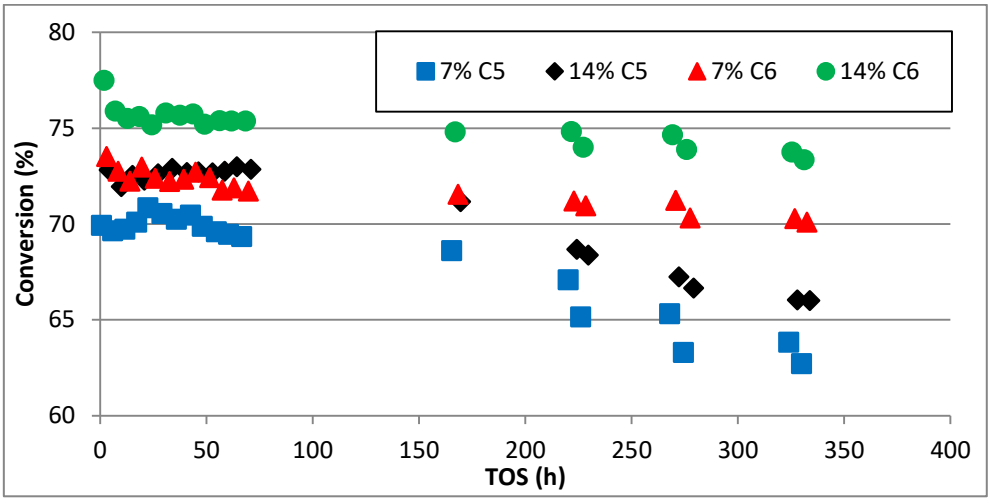

Fig. 11: *n*-Butane conversion at equilibrating conditions during the 4th bench test loaded with 7 and 14 % *C5* and 7 and 14 % *C6* respectively.

Tab. 2: Analysis of fresh and used samples (4th bench test) of *C5* and *C6* (normalized values*)

	C5			*C6*		
	Fresh catalyst	Dilution with 14 wt% catalyst	Dilution with 7 wt% catalyst	Fresh catalyst	Dilution with 7 wt% catalyst	Dilution with 14 wt% catalyst
$\overline{BET}$	0.99	0.86	0.86	1.15	1.03	0.99
$\bar{\varepsilon}_p$	1.05	1.12	1.22	1.12	1.10	1.13
$\overline{P/V}$	1.002	1.001	0.998	1.015	1.009	1.011
$\bar{V}_{ox}$	0.998	0.952	0.955	0.990	0.957	0.952

* The normalized value $\bar{A}_i$ of a parameter A_i is defined as the ratio between A_i and a reference value A_i^{ref}.

On the other hand, the 2nd bench test with full cylinders showed a long-term activation, which was relatively high in the tubes containing 10 and 15 wt% *C1* (Fig. 12). It is worth noting that during this 2nd test some failures of the reactor control system caused very long operating times of the reactor at 440°C SBT. Analysis of *post mortem* samples of the 2nd test revealed a slight decline of the P/V-ratio for the tubes which contained 10 and 15 % catalyst, as well as increased pellet porosities for all samples (Tab. 3). The BET surface area remained almost constant. According to the literature, the P/V ratio of the catalyst is strongly correlated with its activity, as

excess phosphorus prevents the oxidation of the catalyst [6,52,53]. A more detailed discussion of this subject will follow in chapter 1. However, in this light, it is rather curious that no activation was observed in case of the *C2* sample which also showed a reduced P/V-ratio after the test. The variation in pellet porosity and BET surface area indicate the progress of structural changes which the catalyst undergoes in reacting atmosphere, as also observed by Arnold and Sundaresan [41].

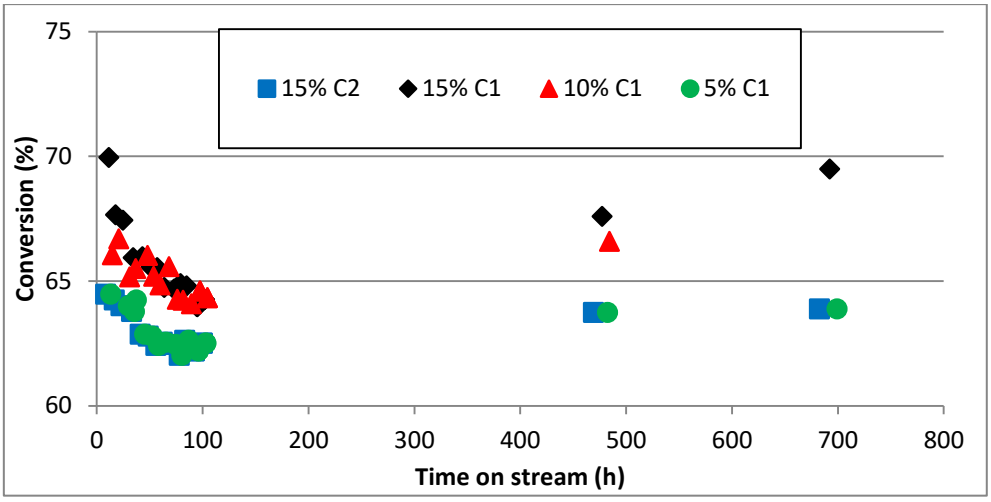

Fig. 12: *n*-Butane conversion at equilibrating conditions during the 2nd bench test loaded with 15 % *C2* and 5, 10 and 15 % *C1*.

Tab. 3: Analysis of fresh and used samples (2nd bench test) of *C1* and *C2* (normalized values*)

	C1				*C2*	
	Fresh catalyst	Dilution with 15 wt% catalyst	Dilution with 10 wt% catalyst	Dilution with 5 wt% catalyst	Fresh catalyst	Dilution with 15 wt% catalyst
$\overline{BET}$	1.00	0.99	0.99	0.99	1.00	0.99
$\bar{\varepsilon}_p$	1.00	1.08	1.09	1.07	1.15	1.26
$\overline{P/V}$	0.978	0.951	0.947	0.979	1.000	0.945
$\bar{V}_{ox}$	0.967	0.952	0.950	0.955	0.967	0.955

* The normalized value $\bar{A}_i$ of a parameter A_i is defined as the ratio between A_i and a reference value A_i^{ref}.

It may be resumed that due to various effects, which were observed throughout the experiments, the interpretation of the experimental results are to be taken with caution. Although for kinetic evaluation the quantitative impact of the non-isothermal reactor behavior and of deviations between real process conditions and set points can be taken into account in the reactor model, the description of changes in catalyst properties and activity are a more critical subject.

2.5.2 Product distribution

The selectivity-conversion plots for the *C1* samples at 410°C (Fig. 13) and 440°C (Fig. 14) show that the MA selectivity generally declines with increasing *n*-butane conversion, while the selectivities to CO and CO_2 increase. An extrapolation to zero conversion of the selectivity profiles of MA, CO and CO_2 appears to give non-zero values. Hence, MA behaves as a primary intermediate, while CO and CO_2 are final products, which are formed in reaction paths parallel to MA, but probably also from the consecutive oxidation of reaction intermediates. These results are in accordance with the literature [3,18,23] and the reaction scheme in Fig. 5.

As also reported in the literature [23], only minor amounts of acrylic and acetic acid are formed during the selective oxidation of *n*-butane. In the presented experiments, these selectivities were constantly below 1 % at all conditions (Fig. 13 and Fig. 14). As the slopes of the selectivity profiles decreased with increasing conversion, it may be concluded that both intermediates are finally oxidized to CO and/or CO_2. The profile of acrylic acid is similar to that of a primary gas phase intermediate, which is produced by *n*-butane on a reaction path parallel to that of MA. On the other hand, the selectivity to acetic acid seems to have a maximum, which is characteristic for secondary or higher intermediates, which form on consecutive reaction paths. However, it cannot be stated unambiguously whether the extrapolation to zero conversion of both side products gives zero selectivity. More precise experiments at low conversions, which would support such fundamental investigations of the reaction network, were not performed, since the focus of this work is the phosphorus dynamics in industrial reactors.

Acetic and acrylic acid as secondary reaction products would be in agreement with the results of Huang *et al.* [26], who found traces of both compounds as decomposition products of MA. A reaction network which includes only parallel reaction paths from *n*-butane to acetic and acrylic acid, as applied by Dente *et al.* [25], cannot account for the observed selectivity profile of acetic acid. It is again accented that more profound investigations of the reaction network were not focused in the present work.

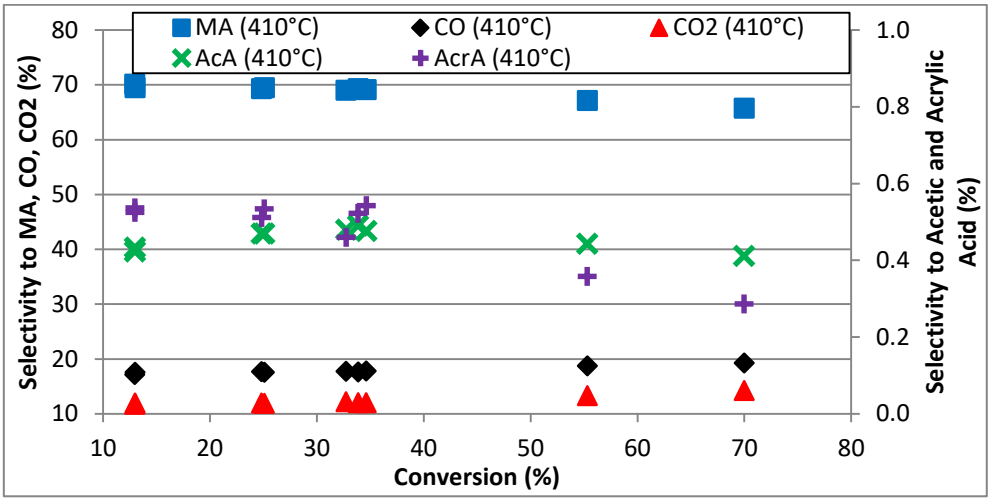

Fig. 13: Selectivity-conversion plots for catalyst *C1* at 410°C with 1.8 vol% *n*-butane.

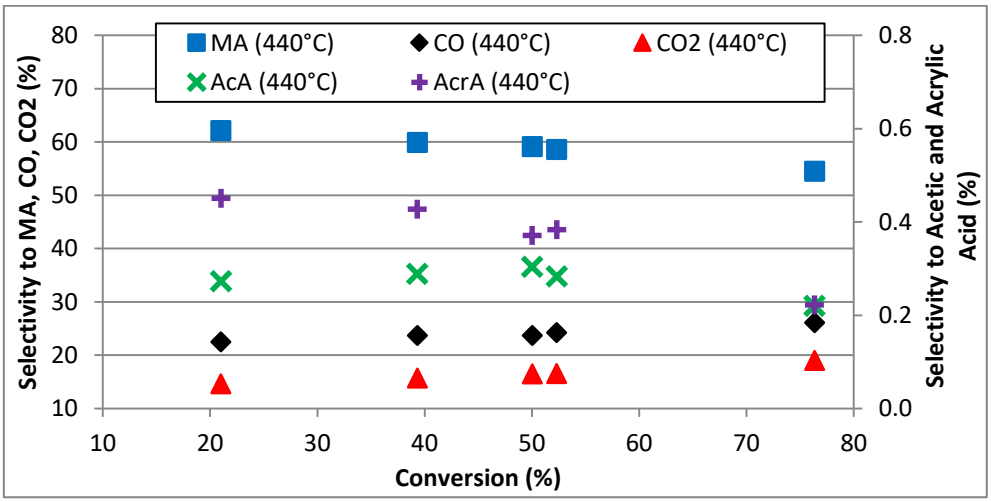

Fig. 14: Selectivity-conversion plots for catalyst *C1* at 440°C with 1.8 vol% *n*-butane.

As shown for the *C1* catalyst sample in Fig. 15 and Fig. 16, the selectivity to MA declines with rising temperature and with reducing inlet concentration of *n*-butane, while the conversion increases. The form of the selectivity profile remains constant in each case. The observed temperature dependence of the selectivity is in agreement with the findings in the literature that the non-selective reactions present higher activation energies [18,23].

As the selectivity-conversion plots for different inlet concentrations in Fig. 16 were obtained from measurements with the same set of residence times, it appears further that the *n*-butane conversion decreases with increasing inlet concentration. Hence, the reaction order with respect to *n*-butane is different from one. This is in accordance with various kinetic studies in

the literature, which obtained reaction orders less than one [29,33] or included an inhibition by *n*-butane in their reaction rate equations [23,28].

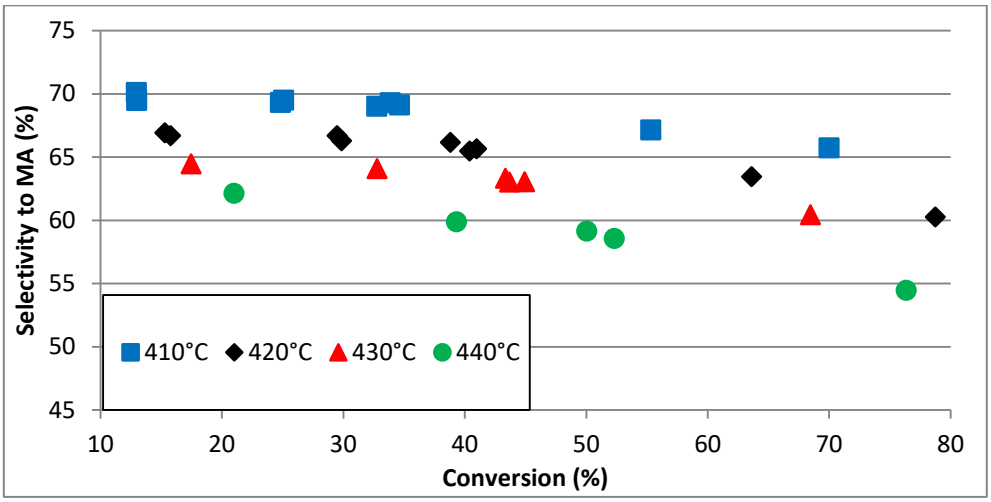

Fig. 15: MA selectivity-conversion plots for catalyst sample *C1* at different temperatures with 1.8 vol% *n*-butane.

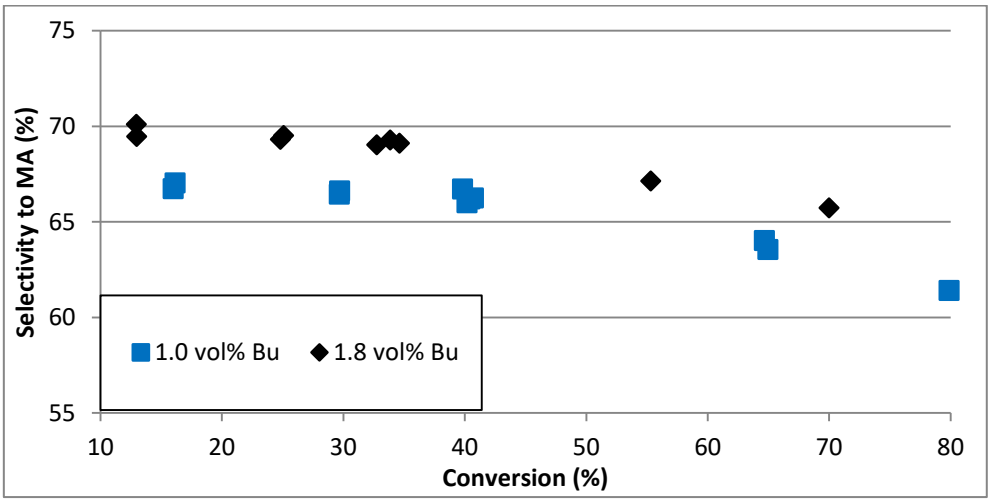

Fig. 16: MA selectivity-conversion plots for catalyst sample *C1* at different *n*-butane inlet concentrations at 410°C.

The CO/CO_2 ratio varied between about 1.2 and 1.8 during the experiments. As shown in Fig. 17 and Fig. 18, the ratio increases with increasing temperature and with decreasing inlet concentration of *n*-butane. Furthermore, the CO/CO_2 ratio declines with increasing conversion, but there seems to be a maximum at conversions between 10 and 40 %, depending on the reaction conditions. However, this maximum cannot be confirmed doubtlessly as there are too

few data points at low conversions. Additionally, the range of the observed effect approaches the experimental accuracy. The same accounts for the appearance that an extrapolation to zero gives different values for the CO/CO_2 ratio, depending again on temperature and on inlet concentration of *n*-butane.

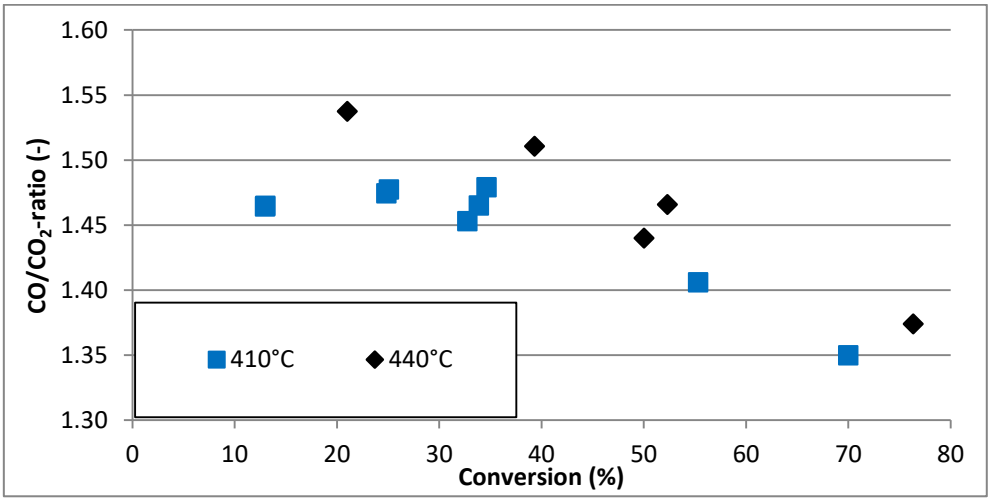

Fig. 17: CO/CO_2-conversion plots for catalyst sample *C1* at different temperatures with 1.8 % *n*-butane.

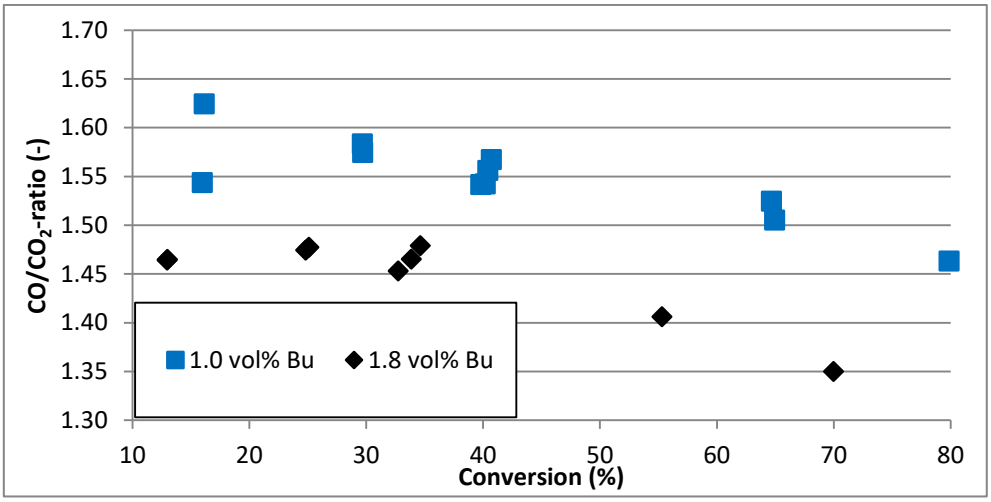

Fig. 18: CO/CO_2-conversion plots for catalyst sample *C1* at different *n*-butane inlet concentrations at 410°C.

Together with the fact, that the CO/CO_2 ratio is constantly higher than one, the declining trend at higher conversions indicates that the consecutive oxidation of MA produces more CO_2 than CO, while the nonselective oxidation of *n*-butane produces more CO. These observations agree

with the findings of Buchanan and Sundaresan [32], Contractor and Sleight [38], and Brandstädter [23], but not with those of Sharma *et al.* [33] and Becker [34], who found that the CO/CO_2 ratio increased with increasing conversion, taking values smaller than one in the inlet zone of the reactor. However, no literature studies were found, which report of an inversion of the gradient of the CO/CO_2 profile at lower conversions, or of the observed relation between CO/CO_2 ratio and *n*-butane feed. This behavior may be debt either to the presence of the consecutive oxidation of CO to CO_2, to polytropic effects, or to the existence of different active sites or reaction mechanisms for the formation of CO and CO_2.

A catalytic oxidation of CO to CO_2 by lattice or adsorbed oxygen is conceivable according to the extended reaction schemes presented in [3,29,30]. The negative slope of the CO/CO_2 profile at higher conversions, as well as the higher CO/CO_2 ratios at lower inlet concentrations of *n*-butane may indicate further that this reaction is enhanced by the presence of water, or even that it occurs according to a water-gas-shift type mechanism. This is because the water concentration in the system increases with increasing conversion and inlet concentration of *n*-butane and thus, the equilibrium of the water-gas-shift-like reaction shifts towards CO_2. Dente *et al.* [25] fed CO under reacting conditions and observed that its oxidation to CO_2 is negligible. However, the authors did not feed CO and water simultaneously. These considerations about the unselective reaction paths clearly underline the necessity of further investigations, which however were not focus of the present work.

The polytropic character of the test reactor causes the formation of hot spots within the catalyst bed, which are more or less pronounced depending on the process conditions and on the heat transfer properties of the reactor. The influence of the temperature profile on the CO/CO_2 profile depends then on the activation energies of the undesired side reactions. The observed increase of the CO/CO_2 ratio with increasing temperature suggests that the activation energy for the formation of CO is higher than for CO_2. This would also explain the changing gradient of the CO/CO_2 profile, if this was located in the hot spot. However, higher *n*-butane concentrations cause higher reaction temperatures in a polytropic reactor, and more heat is released. Hence, the observation that the CO/CO_2 ratio declines with increasing inlet concentration, suggests that it is the CO_2 formation, which exhibits the higher activation energy. This was indeed confirmed by most kinetic studies which are found in the literature and which distinguish between CO and CO_2 [23,26,37], but it does not account for the observed relation between CO/CO_2 ratio and temperature.

The most reasonable explication for the observed trends of the CO/CO_2 profile is thus the presence of different active sites or different reaction mechanisms for the formation of CO and CO_2. It is worth noting that most literature kinetic models are not able to explain the observations of the presented experiments, as they formulate equal rate equations for the parallel oxidations of *n*-butane. In the case of the triangular model, which was applied by Brandstädter [23] and Becker [34], this is explained as follows. If there was only one parallel reaction, which produces CO and CO_2, the ratio of this reaction would be always constant and determined by the stoichiometric parameter (SBT_α in equation 2-i). Hence, the extrapolation to

zero of the CO/CO_2 profile gives the same constant value, independent of the reaction conditions. In contrast, the presented experiments indicate that the initial CO/CO_2 ratio is function of both, *n*-butane and temperature. The dependence on temperature thus, requires separated reactions for the unselective oxidation of *n*-butane with different activation energies, according to works of Schneider *et al.* [37], Huang *et al.* [26] and Gascón *et al.* [36].

On the other hand, Schneider *et al.* [37] and Huang *et al.* [26] used the same rate equations for the unselective parallel reactions. Obviously, the resulting initial value of the CO/CO_2 ratio is the quotient of the respective reaction rates. Hence, if the rate equations have equal forms, the CO/CO_2 ratio results in the quotient of only the rate constants, which are solely function of temperature, but not of the concentration of any compounds. In the end, these models too, cannot account for the observed declining CO/CO_2 ratio with increasing *n*-butane feed concentration. However, if different surface sites or oxygen species were active in the conversions of *n*-butane to CO and CO_2, this would require different rate equations for the respective reactions. Gascón *et al.* [36] considered two parallel reaction paths for the formation of CO_2 from *n*-butane via adsorbed and lattice oxygen, while CO is only formed from lattice oxygen. Depending on their final rate equations, their model could thus account for the observed dependence of the CO/CO_2 ratio on the inlet concentration of *n*-butane.

The observation that the CO/CO_2 ratio increases with decreasing *n*-butane feed indicates that the formation of CO is more strongly inhibited by *n*-butane than that of CO_2. On the other hand, higher *n*-butane feeds lead also to higher amounts of water and other reaction products in the reactor, because of which the product inhibition may also be different in each reaction path. A different inhibition by water would agree with the findings of Contractor *et al.* [45] and Uihlein [28], who observed reduced CO formation at constant conversion after adding water to the reaction. In accordance with the concept of different active sites, the authors of [38] suggest that water is active in stripping nonselective oxygen species from the catalyst surface. Uihlein [28] could improve his kinetic parameter estimation by introducing different inhibition constants, but at the expense of parameter significance. Further researchers who observed a relation between the addition of water and MA selectivity [39–41] did not focus their studies on the CO/CO_2 ratio, but on modifications of the forming active catalyst surface. Their works will be discussed in chapter 1.

It can be concluded that based on the presented experiments it is not possible to receive unambiguous evidence about the formation mechanisms of CO and CO_2. However, inconsistencies in the state of knowledge and parallels to literature studies are obvious. A further investigation requires more measurements at low conversions, so as of course experiments, where reaction products are fed, which was not possible with the experimental setup and not the goal with of the present work.

2.5.3 Influence of transport limitations

In order to illustrate the influence of diffusional limitations, Fig. 19 and Fig. 20 show the selectivity-conversion plots for the different catalyst shapes at 410°C (Fig. 19) and 430°C (Fig. 20) SBT. While at 410°C the profiles are very close to each other, the differences become more visible at 430°C. Actually, this is the first indication for the existence of diffusional resistances, as catalyst efficiency factors generally decline with increasing temperature. In terms of efficiency factor and comparing the two ring shaped samples, *C5* and *C6* with the two full cylinders *C1* and *C2*, the following trend is observed:

$$C6 > C5 > C1 \approx C2$$

The mass transport properties of a porous material are mainly influenced by its porosity, the pore size and the diffusion length, which is characterized by the specific surface area of the shape body. The tortuosity of the porous body may play an additional role, but this parameter should be similar for all catalysts of the present study and is therefore excluded for the following considerations. According to Tab. 1, the order related to good mass transfer properties is as follows:

According to the specific surface area:	$C1 > C5 > C6 > C2$
According to the pellet porosity:	$C6 > C2 > C5 > C1$
According to the average pore radius:	$C5 > C6 > C2 > C1$

It appears thus that the unfavorable pore structure of the *C1* sample in terms of porosity and pore diameter is compensated by its higher surface area, which is why these particles perform similar to the *C2* shape, which has the lowest geometric surface area and an intermediate pore structure. In contrast, the *C6* particles compensate their smaller surface area with a higher porosity, as compared to *C5*. In general, it seems that the beneficial pore structure of the ring shapes is responsible for their better performance. On the other hand, it is worth noting that the observed performance order actually reproduces the order of the BET surface areas (Tab. 1). However, the BET surface area should affect primarily the activity of the catalyst, as it is related to the number of surface sites, which may be active in the catalytic process. A relation between the BET surface area and diffusion properties in terms of tortuosity may also be conceivable, but no related scientific literature could be found.

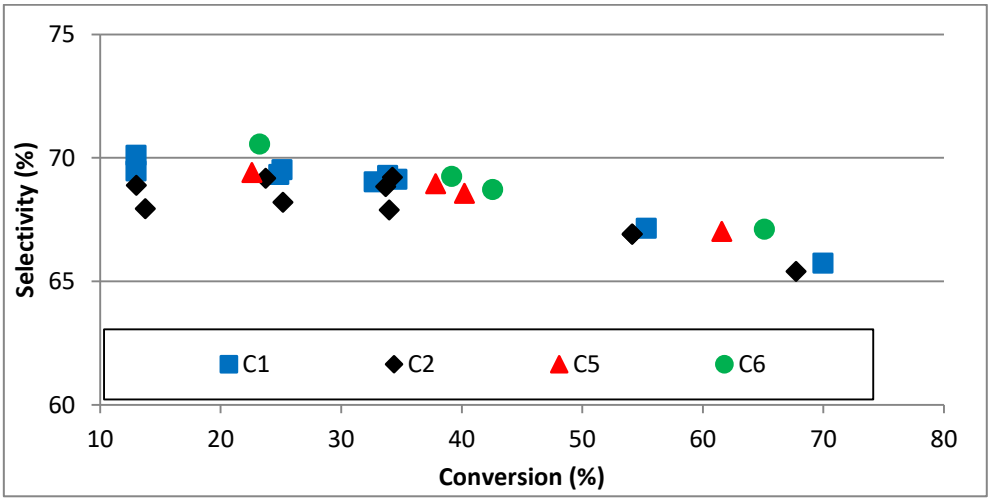

Fig. 19: MA selectivity-conversion plots for different catalyst shapes at 1.8 vol% *n*-butane and 410°C SBT.

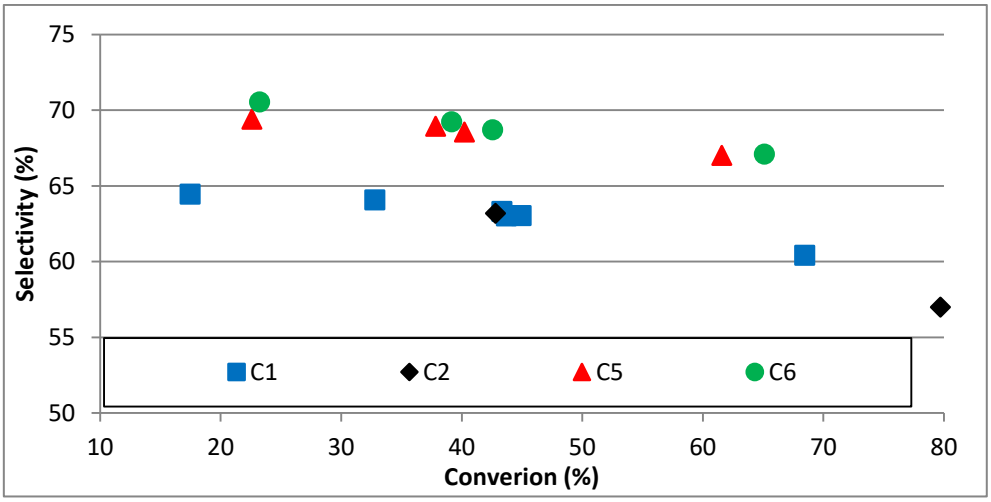

Fig. 20: MA selectivity-conversion plots for different catalyst shapes at 1.8 vol% *n*-butane and 430°C SBT.

Notwithstanding the previous reflections it has to be recalled that the interpretation of Fig. 19 and Fig. 20 is to be treated with caution because of the polytropic behavior of the bench reactor (Fig. 7) and the deviations between intended and real process conditions (Fig. 8). The simulation of the bench reactor experiments should provide more reliable information about the role of diffusional resistances in the catalytic reaction.

3 Kinetic modeling

In order to obtain the reaction kinetics of the selective oxidation of *n*-butane on the applied VPO catalyst shapes, the presented bench reactor experiments were used for kinetic modeling. Based on the experimental findings concerning reaction network and mechanism, different kinetic models were derived and discriminated.

3.1 Bench reactor model

Because of the dilution of the catalyst bed in the bench reactor, the exothermic reactions caused only small hot spots and significant radial temperature gradients are not expected. On the other hand, the experiments confirmed the presence of mass transfer resistances in the applied catalysts, because of which intra-particle diffusion must be taken into account. Hence, the reactor model is non-isothermal, one-dimensional and heterogeneous including a 1D-cylindrical model for the catalyst particles. Additionally, due to the low gas velocities applied during the experiments the Bodenstein numbers (3-1, [16]) were close to the transition range of 100, below which mixing effects may be significant. Therefore, axial dispersion was also included in the reactor model.

$$Bo = \frac{u_z \cdot L}{\mathcal{D}_{ax}} \tag{3-1}$$

A general reactor model was deduced for spherical and cylindrical catalyst pellets, with the respective geometric factor in the catalyst balances, φ_{geo}, which takes the values 1 for full cylinders and rings, and 2 for spheres. The balanced phases are the solid phase (*s*), the fluid phase (*f*) and the fluid solid interface (*sf*). The latter further distinguishes between inner (*isf*) and outer (*osf*) surface of the ring shape, being the fraction of outer surface (f^{osf}) the characteristic parameter for their distinction. For full cylinders and spheres it is 1, while for ring shapes it takes values between 0 and 1. The model was written in gPROMS® (Model Builder Version 3.6, Process Systems Enterprise Ltd., London, 2012) and the steady state model equations are presented below. A detailed derivation of the balance equations can be found in the annex A.2. Given the moderate temperatures and pressures, the concentration terms were expressed by means of the ideal gas assumption.

- **Overall mass balance gas phase:**

$$\frac{\partial}{\partial z}\left(\rho_{fl} \cdot u_z\right) = 0 \tag{3-2}$$

- **Momentum balance:**

$$-\frac{\partial p}{\partial z} = 150 \cdot \frac{(1-\varepsilon_B)^2}{{\varepsilon_B}^3} \cdot \frac{\eta_{fl} \cdot u_z}{d_p^2} + 1.75 \cdot \frac{(1-\varepsilon_B)}{{\varepsilon_B}^3} \cdot \frac{\rho_{fl} \cdot {u_z}^2}{d_p} \quad (3\text{-}3)$$

- **Material balance fluid:**

$$\frac{\partial}{\partial z}\left(\dot{N}_{i,z}^{f,conv} + \dot{N}_{i,z}^{f,disp}\right) - a_p \cdot \dot{N}_i^{sf} = 0 \quad (3\text{-}4)$$

Material flux by dispersion:

$$\dot{N}_{i,z}^{f,disp} = -c_{fl}^f \cdot D_{i,ax}^f \cdot \frac{\partial x_i^f}{\partial z} \quad (3\text{-}5)$$

Material flux between fluid and catalyst surface:

$$\dot{N}_i^{sf} = \beta_i \cdot c_{fl}^f \cdot \left[f^{osf} \cdot \left(x_i^{osf} - x_i^f\right) + \left(1 - f^{osf}\right) \cdot \left(x_i^{isf} - x_i^f\right)\right] \quad (3\text{-}6)$$

- **Material balance solid:**

$$-\frac{\partial \dot{N}_i^s}{\partial r_p} - \frac{\varphi_{geo}}{r_p} \cdot \dot{N}_i^s + \sum_j \nu_{i,j} \cdot r_j \cdot \rho_p = 0 \quad (3\text{-}7)$$

Material flux by diffusion:

$$\dot{N}_i^s = -c_f^s \cdot D_i^{s,eff} \cdot \frac{\partial x_i^s}{\partial r_p} \quad (3\text{-}8)$$

- **Energy balance fluid:**

$$-\frac{\partial}{\partial z}\left(\dot{H}^{f,conv} + \dot{H}^{f,disp} + \dot{Q}^{f,cond}\right) + a_p \cdot \left(\dot{H}^{sf} + \dot{Q}^{sf}\right) - \frac{2}{R_T} \cdot \dot{Q}^w = 0 \quad (3\text{-}9)$$

Heat flux by axial conduction:

$$\dot{Q}^{f,cond} = -\lambda_z^f \cdot \frac{\partial T^f}{\partial z} \quad (3\text{-}10)$$

Heat transfer to the coolant (salt bath):

$$\dot{Q}^w = U_W \cdot \left(T^f - T^{SB}\right) \quad (3\text{-}11)$$

Heat transfer between fluid and solid:

$$\dot{Q}^{sf} = \alpha_p \cdot \left(T^{sf} - T^f\right) \tag{3-12}$$

$$T^{sf} = T^{osf} = T^{isf} \tag{3-13}$$

- **Energy balance catalyst particle:**

$$\frac{\partial}{\partial r_p}\left(\dot{Q}^s + \dot{H}^s\right) + \frac{\varphi_{geo}}{r_p} \cdot \left(\dot{Q}^s + \dot{H}^s\right) + \sum_i \sum_j \nu_{i,j} \cdot r_j \cdot \rho_p \cdot \Delta_F H_i^* = 0 \tag{3-14}$$

Heat conduction in the solid:

$$\dot{Q}^s = -\lambda_r^s \cdot \frac{\partial T^s}{\partial r_p} \tag{3-15}$$

- **Boundary conditions solid:**

$r_p = R_{p,outer}$:

$$\dot{N}_i^s|_{Rp,outer} = \dot{N}_i^{osf} = \beta_i \cdot c_{fl}^f \cdot \left(x_i^{osf} - x_i^f\right) \tag{3-16}$$

$$\dot{Q}^s|_{Rp,outer} = \dot{Q}^{osf} = \alpha_p \cdot \left(T^{sf} - T^f\right) \tag{3-17}$$

$r_p = R_{p,inner}$:

Rings:

$$\dot{N}_i^s|_{R_{p,inner}} = \dot{N}_i^{isf} = \beta_i \cdot c_{fluid}^f \cdot \left(x_i^{isf} - x_i^f\right) \tag{3-18}$$

$$\dot{Q}^s|_{R_{p,inner}} = \dot{Q}^{isf} = \alpha_p \cdot \left(T^{sf} - T^f\right) \tag{3-19}$$

Full cylinders and spheres:

$$\frac{\partial x_i^s}{\partial r_p}|_{r_p=0} = \frac{\partial x_i^{isf}}{\partial r_p} = 0 \tag{3-20}$$

$$\frac{\partial T^s}{\partial r_p}|_{r_p=0} = \frac{\partial T^{isf}}{\partial r_p} = 0 \tag{3-21}$$

- **Boundary conditions reactor inlet:**

$$\dot{N}_i^f|_{z=0} = \dot{N}_{i0}^f \tag{3-22}$$

$$T^f|_{z=0} = T^s|_{z=0} = T^{SB} \tag{3-23}$$

In the heat balances, the terms denominated by $\dot{Q}$ refer to heat transfer by conduction or convection, while $\dot{H}$ is the conserved quantity by mass transport. In the case of the ring shapes the temperature at the inner and outer ring wall are assumed to be equal as the intra-particle temperature gradients generally are of minor significance as compared to the external differences [54,55]. On the other hand, significant concentration gradients inside the catalyst particle may effect different concentrations at the inner (x_i^{isf}) and outer surface of the ring (x_i^{osf}).

An important issue is the geometrical description of the catalyst particles, which affects the material and energy balances of the solid phase (equation (3-7) and (3-14)). For ideal spheres, cylinders, and plates, the geometric factor, φ_{geo}, is 2, 1 and 0 respectively. However, the applied full cylinders and rings cannot at all be considered as ideal shapes, as they present low height-to-diameter ratios, while for ideal cylinders the ratio is infinitely large. On the other hand, taking into account the real particle surface-to-volume ratio, S_v, which characterizes the diffusion path in the catalyst pellet, the real catalyst geometry can be transformed into that of an equivalent ideal shape. In case of rings, the fraction of outer surface, f^{osf}, of the real shape must be additionally taken into account. Finally, the equivalent radii, which have to be used for simulation, are calculated according to equations (3-24) to (3-26).

- Spheres:

$$R_P^{eq} = \frac{3}{S_v} \tag{3-24}$$

- Full cylinders (f^{osf} = 1) and rings (f^{osf} < 1):

$$R_{P,outer}^{eq} = \frac{2}{S_v} \cdot \frac{f^{osf}}{2 \cdot f^{osf} - 1} \tag{3-25}$$

$$R_{P,inner}^{eq} = R_{P,outer}^{eq} \cdot \frac{1 - f^{osf}}{f^{osf}} \tag{3-26}$$

A geometry characteristic which may serve as an indicator for which model to choose, is the sphericity of a particle which is defined as the ratio of the area of a volume equivalent sphere to the area of the particle. For the full cylinder shapes of the present work the sphericity was about 0.9, while for the ring shapes it was around 0.6. This suggests that the sphere model may describe the applied full cylinders, but in case of the rings, the cylindrical model may fit better. However, it finally has to be tested during the simulations, which is the best option for each shape.

As the reactor operates at relatively high temperature and low pressure, ideal gas behavior was assumed. The material properties were derived from the DIPPR database accounting for their dependence on temperature, pressure and gas phase composition.

The coefficients for heat and mass transfer between gas and solid, as well as the coefficients for axial dispersion are calculated according to the correlations found in [56,57] (see annex A.3). Because of the high dilution of the reacting compounds in air, the diffusion in the catalyst pellet is described by the classical Fickian model with an effective diffusion coefficient expressed by equation (3-27) in which $D_{i,mix}$ contains the molecular diffusion according to Fuller [15] with the mixing rule according to Wilke [55]. For the applied catalyst and operating conditions, the Knudson diffusion term was estimated to have no major influence on the overall diffusivity being in the same order of magnitude as the term for molecular diffusion (1.5-3.0*10^{-5} m²/s) in case of all components. The unknown thermal conductivity of the catalyst was assumed to 0.1 W/m/K which is within the range of typical values [14,16].

$$D_i^{eff} = \left(\frac{1}{D_{i,mix}} + \frac{1}{D_{K,i}}\right)^{-1} \cdot \frac{\varepsilon_p}{\tau} \qquad (3\text{-}27)$$

Fig. 21 shows some simulated profiles of the concentrations of *n*-butane and MA, and of the temperature inside the catalyst for the spherical and the ring shape model. In case of the ring shaped particles the profiles present a maximum/minimum close to the center of the ring wall ($r_p/(R_{p,outer} - R_{p,inner}) > 0$), while for the spherical particles the gradients are zero at the center of the sphere ($r_p/R_p = 0$). The faintly visible maximum of the MA concentration at about $r_p/R_p = 0.6$ is debt to temperature effects. The maximum predicted temperature gradients are around 3 K.

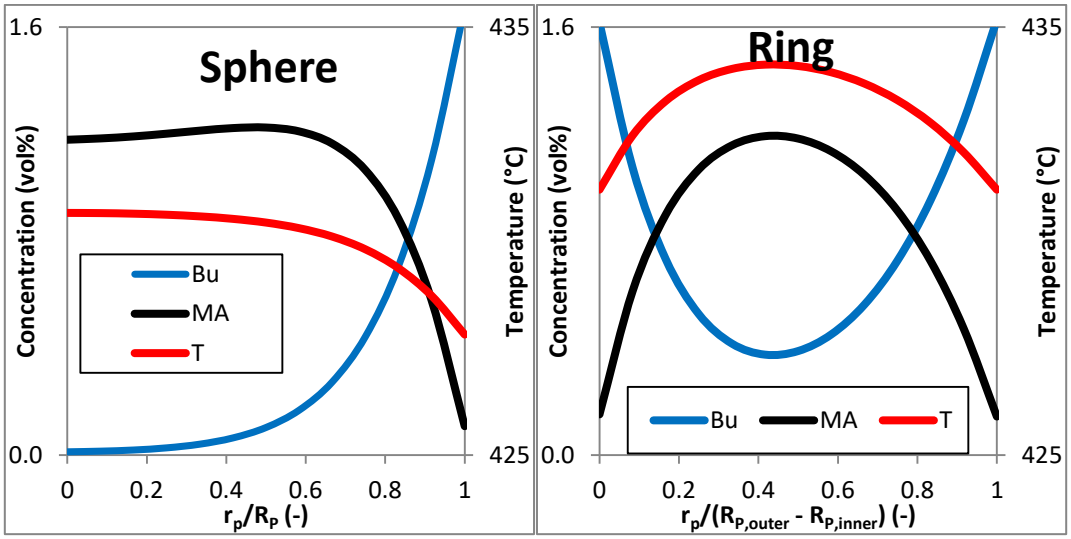

Fig. 21: Simulated concentration and temperature profiles for the spherical (left) and the ring shape model (right). Simulation conditions: 2680 NL/h/kGC$_{at}$ GHSV, 1.8 vol% *n*-butane and 410°C SBT.

In general, models for packed beds must account for the radial heat transport through both, the fluid and the solid phase. In case of pseudo homogeneous reactor models, which do not distinct between fluid and solid phase, this is usually done by lumping together the contribution of both phases into one effective heat conductivity parameter. In contrast, heterogeneous models, which imply separate balances for fluid and solid, theoretically require two heat conductivity parameters. However, as global heat transfer parameters for packed beds are usually derived from pseudo homogeneous models, a common method in case of one-dimensional and heterogeneous reactor models is describing the radial heat transport only through the gas phase [16,55], using the above mentioned effective parameter. This procedure was also applied in the presented model for the bench reactor. The solid only exchanges heat with the gas phase, which then carries out the heat transfer to the reactor wall. According to [55], the final heat transfer coefficient, U_W, which describes the overall temperature gradient between catalyst bed and coolant in one-dimensional reactor models, consists of a series connection of the following resistances: the effective radial conductivity of the catalyst bed (λ_r^{eff}), the heat transfer between catalyst and reactor wall (α_W), the conductive heat transport through the wall (λ_r^w) and heat transfer between wall and coolant (α_{SB}). In the presented reactor model λ_r^{eff} and α_W were calculated according to the correlations found in [56] (see annex A.3). The series connection gives:

$$\frac{1}{U_W} = \frac{R}{4 \cdot \lambda_r^{eff}} + \frac{1}{\alpha_W} + \frac{R_{T,outer} \cdot ln\left(R_{T,outer}/R\right)}{\lambda_r^w} + \frac{1}{\alpha_{SB}} \tag{3-28}$$

The resulting simulated temperature profiles are of the form as presented in Fig. 22. After reaching the hot spot temperature with a high initial slope, the gradient in the remaining section is lower due to the dilution of the catalyst. It is worth noting that the simulated maximum temperature differences are in the same range as the values, which were measured during the experiments. However, a more precise evaluation is not possible as the exact positions of the temperature sensors in the catalyst bed were unknown.

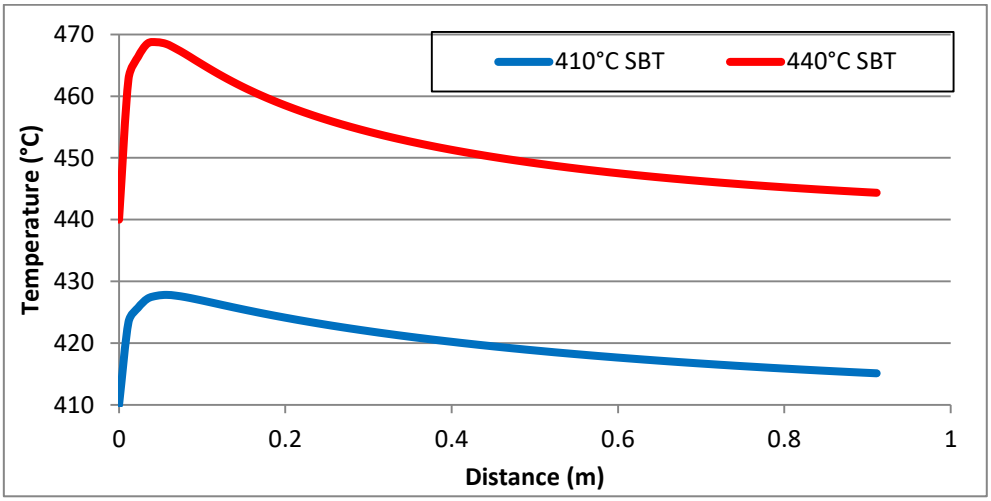

Fig. 22: Simulated catalyst temperature profiles at 410 and 440°C SBT at the following conditions: 2680 NL/h/kGC$_{at}$ GHSV, 1.8 vol% *n*-butane.

3.2 Kinetic model

There are various ways to categorize the large number of kinetic studies, which have been published since the early 1980s. Different Hougen-Watson and redox type approaches have been presented for the description of steady state kinetic experiments, while several authors also derived more detailed redox models from transient experiments. Further differences in the scientific literature arise from varying considerations about reaction scheme and mechanism.

As presented in section 2.1, steady state Hougen-Watson type equations were applied for the triangular reaction scheme by Sharma *et al.* [33], Uihlein [28], Becker [34] and Brandstädter [23]. The general form of these equations is

$$r_{i,j} = \frac{k_{i,j} \cdot p_i^{o_{1,i,j}} \cdot p_{O2}^{o_{2,i,j}}}{(1+\sum_k K_k \cdot p_k)^{o_{3,i,j}}} \quad i = n\text{-Bu, MA} \quad j = \text{MA, CO}_x \quad k = n\text{-Bu, H}_2\text{O, MA} \qquad (3\text{-}29)$$

In the works of Uihlein [28], Becker [34] and Brandstädter [23] the reaction order of the hydrocarbon ($o_{1,i,j}$) is one and that of oxygen ($o_{2,i,j}$) is 0.5. Only Uihlein [28] used 0.25 for the oxidation of MA. In the same works, the reaction is inhibited by *n*-butane and water, while the exponent of the denominator ($o_{3,i,j}$) is one. Their resulting kinetic model may be derived according to an Eley-Rideal mechanism, where the gas phase hydrocarbon reacts with adsorbed oxygen, which competes with water and *n*-butane for free adsorption sites. All adsorption constants were considered independent of temperature. It should be pointed out that the

complex conversion of *n*-butane to MA unlikely occurs by single collision between *n*-butane and adsorbed oxygen, which is the fundamental assumption of the Eley-Rideal mechanism. In this case it rather means that the rate determining step is the activation of *n*-butane from gas phase on an oxidized site. The validity of such simple Hougen-Watson type models for this reaction further bases on a sufficiently good description of experimental observations. The same accounts for the apparent temperature independence of adsorption constants.

In the model of Sharma *et al.* [33], only product inhibition by MA was included and the exponent of the denominator of the decomposition reaction (o_{3,MA,CO_x}) is 2. However, the authors did not feed MA to their test reactor. Taking into account that the concentration profiles of MA and water are increasing along the reactor, their estimated product inhibition may thus actually refer to water, as it was observed by several authors [28,41,45]. An inhibition by MA was experimentally confirmed by Buchanan and Sundaresan [32], and even excluded by Uihlein [28]. The reaction order of *n*-butane in the model of Sharma *et al.* [33] is 0.54 and all reaction rates are independent of the oxygen concentration.

Langmuir-Hinshelwood-Hougen-Watson type rate equations were also applied by Dente *et al.* [25]. The authors included additionally the formation and decomposition of acrylic and acetic acid in their reaction scheme, and CO and CO_2 were considered separately. Unfortunately, neither the final rate equations nor kinetic parameters were presented in their paper.

Different redox approaches for the triangular reaction scheme were applied by Buchanan and Sundaresan [32], Bej and Rao [31] and Lorences *et al.* [43]. The model of Buchanan and Sundaresan [32] may be deduced according to the standard Mars-van-Krevelen mechanism. The rate equations take the form

$$r_{i,j} = \frac{k_{i,j} \cdot c_i}{1+\sum_i K_i {}^{c_i}/_{c_{O_2}}} \qquad i = n\text{-Bu, MA} \quad j = \text{MA, CO}_x \qquad (3\text{-}30)$$

The authors observed product inhibition by MA and water, which was lumped together into one inhibition constant. Assuming either 0.5 or 1 for the exponent of the oxygen concentration gave results of similar quality. Uihlein [28] did also try a more detailed form of the Mars-van-Krevelen model according to equation (3-31), which contained an additional inhibition by water. However, he obtained better results with the Eley-Rideal model. Obviously, the form of equation (3-30) may be obtained by dividing equation (3-31) by the rate of catalyst oxidation.

$$r_{i,j} = \frac{k_{i,j} \cdot k_{ox} p_i \cdot p_{O2}^{0.5}}{(1+K_{H2O} \cdot p_{H2O}) \cdot [\sum_j k_{Bu,j} \cdot p_{Bu} + k_{MA,CO_x} \cdot p_{MA}] + k_{ox} \cdot p_{O2}^{0.5}} \quad i = n\text{-Bu, MA} \quad j = \text{MA, CO}_x \quad (3\text{-}31)$$

The steady state redox model of Bej and Rao [31] is more complex as it includes different active sites for the selective and unselective reaction paths. While MA is produced on V^{5+}-sites, the decomposition of *n*-butane and MA to CO_x occurs on V^{4+}-sites which are further reduced to V^{3+}.

Lorences *et al.* [43] observed CO overshoots after switching from reducing to oxidizing atmosphere during dynamic experiments, from which they assumed that the unselective parallel reaction occurs through chemisorbed *n*-butane on V^{4+}-sites which react with gas phase oxygen. The selective oxidation and the decomposition of MA are carried out on V^{5+}-sites. Although they could not confirm the same behavior for CO_2 because of analytical limitations, CO and CO_2 were lumped together according to the triangular reaction scheme. Including the catalyst oxidation and the irreversible chemisorption of *n*-butane the final kinetic model was composed of five elementary reactions with first order rate laws.

Hess *et al.* [27] observed furan selectivities up to 10 % during steady state experiments under fuel rich conditions, which was hence included in their kinetic model as an intermediate. According to the redox models of Buchanan and Sundaresan [32] and Uihlein [28], all hydrocarbon oxidation reactions were considered to be performed by the same lattice oxygen site, which is subsequently reoxidized by gas phase oxygen. Each reaction rate is of first order with respect to the gas phase compound and the catalyst surface site. The authors could further simulate unsteady state experiments with their model. Thereby, the course of selectivities to furan and MA fit well with the simulated dynamics of oxygen storage in the catalyst.

Wang *et al.* [29,30] carried out separated oxidation and reduction experiments in an oscillating microbalance reactor. For the reduction of the catalyst a reaction scheme was proposed which combined the selective and unselective oxidation of *n*-butane by lattice oxygen into only one reaction with adjustable stoichiometric parameters. The decomposition of MA, so as the oxidation of CO by lattice oxygen were neglected for kinetic modeling. The authors found that the reaction order of the catalyst reduction is 0.4 with respect to *n*-butane and 4 with respect to lattice oxygen. A mechanistic explanation of these numbers was not given. The reoxidation has the order 0.55 with respect to gas phase oxygen. The latter finding was supposed to be debt to an intermediate adsorption of molecular oxygen. The authors further estimated that the total oxygen capacity corresponds to the reduction of vanadium of about five surface layers, whereas the diffusion of lattice oxygen is not a limiting factor.

More detailed redox models which consider CO and CO_2 separately were presented by Huang *et al.* [26] and Gascón *et al.* [36]. They considered different mechanistic steps and expressed the respective reaction rates by first order laws. Huang *et al.* [26] assumed that MA is formed by lattice oxygen while the unselective oxidation of *n*-butane and MA to CO and CO_2 occurs through adsorbed oxygen. Their kinetic model includes thus, the adsorption of oxygen, which consecutively reacts with the surface to form lattice oxygen, and additionally, the diffusion of lattice oxygen into the bulk. Furthermore, *n*-butane was assumed to react with first order from the gas phase, while MA decomposes from an adsorbed state. Their final kinetic model includes nine reactions.

The model of Gascón *et al.* [36] includes the same oxygen species as [26] and also comprises nine reactions. Accordingly, *n*-butane can be oxidized from the gas phase by adsorbed oxygen or from an adsorbed state by surface lattice oxygen. The former gives only MA and CO_2, while the latter additionally produces CO. The decomposition of MA was only considered according to one reaction between gas phase and surface lattice oxygen, which produces only CO_2.

Discrepancies in the presented kinetic models may arise among other things from the catalyst and the investigated reaction conditions, as well as from the fact if whether dynamic or steady state experiments were evaluated. For example, Buchanan and Sundaresan [32] found different kinetic parameters for two tested catalysts as a function of the P/V ratio. Lorences *et al.* [43] reported that they could not describe transient and steady state experiments with the same kinetic parameters. One reason may be the proper dynamic of complex structural changes which occur on the active surface as a function of reaction conditions and catalyst properties [39,40]. Another reason is surely the lack of knowledge about the real reaction mechanism.

For the purpose of developing a kinetic model for the description of the experiments of the present work, a couple of requirements may be deduced from the statements in section 2.5.2:

- The only products to be considered are MA, CO, CO_2 and water, while acrylic and acetic acid may be neglected.
- CO and CO_2 must be considered separately.
- The mechanism of CO formation is different as compared to the formation of CO_2.
- The reaction is inhibited by *n*-butane
- As found by different authors [28,41,45] and in own pilot reactor experiments which will be presented in chapter 1, the reaction is inhibited by water.

The 1st condition results from the measured product distribution, whereas the selectivity to acrylic and acetic acid was constantly below 1 mol%. The 2nd and the 3rd conclusion yield from the observed trends of the CO/CO_2 profiles. Additionally, a correct treatment of the unselective side reactions should be of major importance for the simulation of industrial scale reactors. This is because of the strongly different reaction enthalpies (CO from *n*-butane: -1521 kJ/mol, CO_2 from *n*-butane: -2656 kJ/mol) which will significantly determine form and height of the temperature profile.

It is worth noting again that none of the above presented literature models is able to account for all these requirements. Although the dynamic models of [26,36] may provide some ideas for a more detailed description of the CO and CO_2 reaction paths, they include too many parameters and they do not account for the influence of water. At continuation, some new simple steady state models are proposed which are similar to those of Uihlein [28] and Buchanan and Sundaresan [32], but which account for the above listed requirements. The consequence of the different mechanism of the CO formation is then a different kinetic expression as compared to

the other reactions. The proposed models are listed in Tab. 4. A detailed derivation of the proposed rate equations can be found in the appendices. The five considered reactions are shown below ((3-i)-(3-v)). The simulations showed that the inclusion of the oxidation of CO to CO_2 was not necessary.

Tab. 4: Proposed kinetic models

Model	**Reaction rate equations**
HW1	$r_{i,j} = \frac{k_{i,j} \cdot p_i \cdot p_{O_2}^{0.5}}{1+K_{Bu,1} \cdot p_{Bu}+K_{H_2O} \cdot p_{H_2O}}$ *i* = Bu, MA ; *j* = MA, CO, CO_2; $i \neq j$ (3-32)
HW2	$r_{i,j} = \frac{k_{i,j} \cdot p_i \cdot p_{O_2}^{0.5}}{1+K_{Bu,1} \cdot p_{Bu}+K_{H_2O} \cdot p_{H_2O}}$ *i* = Bu, MA; *j* = MA, CO_2; $i \neq j$ (3-33) $r_{Bu,CO} = \frac{k_{Bu,CO} \cdot p_{Bu} \cdot p_{O_2}^{0.5}}{\left(1+K_{Bu,1} \cdot p_{Bu}+K_{H_2O} \cdot p_{H_2O}\right)^2}$ (3-34) $r_{MA,CO} = \frac{k_{MA,CO} \cdot p_{MA} \cdot p_{O_2}^{0.5}}{1+K_{Bu,1} \cdot p_{Bu}+K_{H_2O} \cdot p_{H_2O}}$ (3-35)
HW3	$r_{i,j} = \frac{k_{i,j} \cdot p_i \cdot p_{O_2}^{0.5}}{1+K_{Bu,1} \cdot p_{Bu}+K_{H_2O} \cdot p_{H_2O}}$ *i* = Bu, MA; *j* = MA, CO_2; $i \neq j$ (3-36) $r_{i,j} = \frac{k_{i,j} \cdot p_i \cdot p_{O_2}^{0.5}}{1+K_{Bu,2} \cdot p_{Bu}+K_{H_2O} \cdot p_{H_2O}}$ *i* = Bu, MA; *j* = CO (3-37)
RO	$r_{i,j} = \frac{k_{i,j} \cdot p_i}{2+K_{Bu,1} \frac{p_{Bu}}{p_{O_2}^{0.5}} \cdot \left(1+K_{H_2O} \cdot p_{H_2O}\right)}$ *i* = Bu, MA; *j* = MA, CO_2; $i \neq j$ (3-38) $r_{i,j} = \frac{k_{i,j} \cdot p_i}{2+K_{Bu,2} \frac{p_{Bu}}{p_{O_2}^{0.5}} \cdot \left(1+K_{H_2O} \cdot p_{H_2O}\right)}$ *i* = Bu, MA; *j* = CO (3-39)

$C_4H_{10} + 3.5\ O_2 \rightarrow C_4H_2O_3 + 4\ H_2O$ (3-i)

$C_4H_{10} + 4.5\ O_2 \rightarrow 4\ CO + 5\ H_2O$ (3-ii)

$C_4H_{10} + 6.5\ O_2 \rightarrow 4\ CO_2 + 5\ H_2O$ (3-iii)

$C_4H_2O_3 + O_2 \rightarrow 4\ CO + H_2O$ (3-iv)

$C_4H_2O_3 + 3\ O_2 \rightarrow 4\ CO_2 + H_2O$ (3-v)

The first Hougen-Watson type kinetic model which corresponds to the Eley-Rideal approach of Uihlein [28], Becker [34] and Brandstädter [23] is hereafter denominated *HW1*. It includes the adsorption of water and *n*-butane on free surface sites while the surface concentration of adsorbed oxygen is supposed to be negligible. In all derived Hougen-Watson type kinetic models, the reaction step is rate determining.

The second Hougen-Watson type model, *HW2*, is obtained analogously to *HW1*. The only difference is that the formation of CO from *n*-butane is performed by the reaction of adsorbed *n*-butane and oxygen according to a Langmuir-Hinshelwood mechanism.

Another option is to apply the Eley-Rideal approach to all five reactions, according to the works of [23,28,34], but with different inhibition constants for the CO formation. Actually, Uihlein [28] could improve the simulation of his experiments by introducing different adsorption constants, although at the cost of reduced statistical quality of the parameter estimation results. The assigned *HW3* model assumes that the CO formation takes place on different active sites and is differently inhibited by *n*-butane, while the inhibition of water is equal for all reactions. Also the redox type model, *RO*, postulates that two different sites are formed by the catalyst oxidation reaction. One of these sites produces CO and the other produces MA and CO_2 by reaction with gas phase hydrocarbon. The quasi steady state principle applies for the oxidized sites, while water adsorption on reduced sites reaches equilibrium.

Neglecting the dependence on temperature of any inhibition constants, the *HW1* and *HW2* model include seven parameters, while the *HW2* and the *RO* model include eight. Except of *HW1*, all kinetic approaches are able to account for the experimental finding that the CO/CO_2 ratio is higher than one, but increases with decreasing inlet concentration of *n*-butane. They even may describe the observation of Uihlein [28], and Contractor *et al.* [45] that the CO/CO_2 ratio is reduced at higher inlet concentrations of water. In the *HW2* model, these properties are obvious as the denominator for the formation of CO by *n*-butane is squared. In case of the *HW3* and the *RO* model, the effects of *n*-butane and water on the CO formation can be described if $K_{Bu,2}$ is higher than $K_{Bu,1}$.

3.3 Parameter estimations

Parameter estimations for the above presented kinetic models were conducted with the parameter estimation module of gPROMS®. In total, 390 steady state analyses were used. The respective solution algorithm of gPROMS® implies the solution of the reactor model for each

respective operating conditions and compares the simulated concentrations to the experimental values. The numerical solver for parameter estimations then varies the model parameters according to a combined search and gradient method, and resolves the model again. The objective function to be minimized is the maximum likelihood function (3-40).

$$\psi = \frac{N}{2} \cdot ln(2\pi) + \frac{1}{2} \cdot min\left\{\sum_i ln\left(\sigma_i^2\right) + \frac{\tilde{x}_i - x_i}{\sigma_i^2}\right\} \quad (3\text{-}40)$$

In this function N is the total number of measurements, σ_i is the variance of measured variable *i*, and $\tilde{x}_i$ and x_i are calculated and experimental value of measured variable *i*.

As described in the experimental section, the formation of acrylic and acetic acid may be neglected. Therefore, it can be assumed that all converted *n*-butane, which does not react towards CO or CO_2, produces MA. As further on, the six components of the considered reaction system (*n*-butane, MA, CO, CO_2, oxygen and water) may all be expressed by the general formula $C_xH_yO_z$, the concentrations of only three key components suffice for the description of the measured product distribution. Hence, the outlet concentrations of *n*-butane, CO and CO_2, which were measured in the IR-analyzer, are sufficient for data evaluation. The concentrations of MA, water and oxygen are then calculated according to the elemental balances of carbon, hydrogen and oxygen respectively. As compared to the GC analysis, the committed error in the determination of the MA concentration was always below 5 %.

For the measured concentrations, a linear variance model was chosen according to equation (3-41). The relative error, *γ,* was assumed to be 1 % and the offset, *δ,* was set to 0.03 %, as it is specified by the manufacturer of the IR-analyzer.

$$\sigma_i^2 = (\gamma \cdot x_i + \delta)^2 \quad (3\text{-}41)$$

An Arrhenius type dependency was assumed and the kinetic constants were re-parametrized according to equation (3-42) in which $k_{i,j}^{ref}$ is the kinetic constant at a reference temperature, T^{ref}, for which 420°C was chosen. As the employed catalyst samples presented different BET surface areas, the kinetic constants were further multiplied by the normalized actual BET surface area for each catalyst shape respectively (equation (3-43)). According to similar, above presented literature models [23,28], the temperature dependence of the inhibition constants in all applied kinetic models was found to be not significant during the parameter estimations and were hence neglected. The parameters to be estimated were the five kinetic constants at reference temperature, $k_{i,j}^{ref}$, with the corresponding activation energies, $E_{i,j}$, the inhibition constants, K_k, as well as the tortuosity factor as this could not be estimated separately.

$$k_{i,j} = k_{i,j}^{ref} \cdot exp\left[-\frac{E_{i,j}^{A}}{R} \cdot \left(\frac{1}{T} - \frac{1}{T^{ref}}\right)\right] \quad (3\text{-}42)$$

$$k_{i,j}^{*} = k_{i,j} \cdot \overline{BET} \quad (3\text{-}43)$$

It is worth noting that the kinetic modeling in this part considers steady state only. That means that no dynamic effects are included. Irreversible ongoing changes in catalyst performance as they were observed in some cases will thus reduce the model accuracy.

3.4 Results

With respect to the choice of the pellet model, the best fit was obtained, when full cylinder and ring shapes were described with the cylindrical model. The dimensions of the real particles were transformed according to equations (3-25) and (3-26). In terms of objective function, all proposed kinetic models were able to describe the experiments similarly well, varying the sums of weighted residuals (3rd term in equation (3-40)) in a range of 5 % (Tab. 5). It is remarkable that the *HW1* model, which is the only one that cannot account for the observed CO/CO_2 profiles, gives still slightly better results than models *HW2* and *RO1*. The best fit was obtained with the *HW3* model, although the objective function is only 2 % lower than that of *HW1*. The reason for this may be the existence of too few measurements at low conversions in addition to the similar magnitude of real effect and experimental deviation. Therefore, the slight increase in CO/CO_2 ratio with decreasing *n*-butane concentration, so as the apparent changing slope of the CO/CO_2 profiles at low conversions may appear statistically not significant.

Tab. 5: Relative values of the sum of weighted residuals for the different kinetic models

	HW1	*HW2*	*HW3*	*RO1*
Weighted residuals (relative value)	1.03	1.04	1.00	1.05

Fig. 23 compares the measured profiles with those simulated using *HW3* for the three cases, which had been discussed in section 2.5.2 (Fig. 17 and Fig. 18). Actually, the observed trends are not reproduced appropriately by the model. Obviously, the lines for 1.8 % and 1.0 % *n*-butane at 410°C are almost identical, although the 1.0 % curve should be higher. The simulated CO/CO_2 profile for 440°C is also too high. However, it must be taken into account that the measured

points of one set of SBT and *n*-butane concentration correspond to the analysis at different total flow rates and catalyst dilutions. Consequently, each measurement was generated at different profiles of heat generation and temperature. Therefore, a comparison to the measured profiles is to be taken with caution. On the other hand, the measured selectivity profiles can be reproduced very well by the model *HW3* (Fig. 24). It is worth noting that the deviations with the other models were significantly higher in terms of both, qualitative trends and absolute values (see Annex A.5). As discussed in section 3.2, a quantitative correct description of the selectivity profiles is considered to be essential for further simulations of polytropic industrial reactors because of which in this work is proceeded with the *HW3* model.

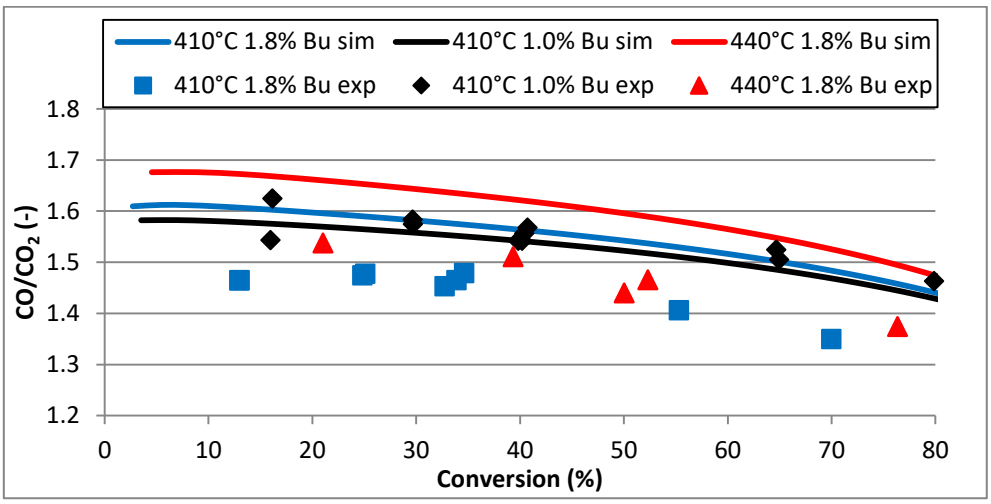

Fig. 23: Measured and simulated CO/CO_2 profiles at different SBT and *n*-butane inlet concentrations. Simulation: *HW3* model, 165 kg/m³ catalyst *C1*.

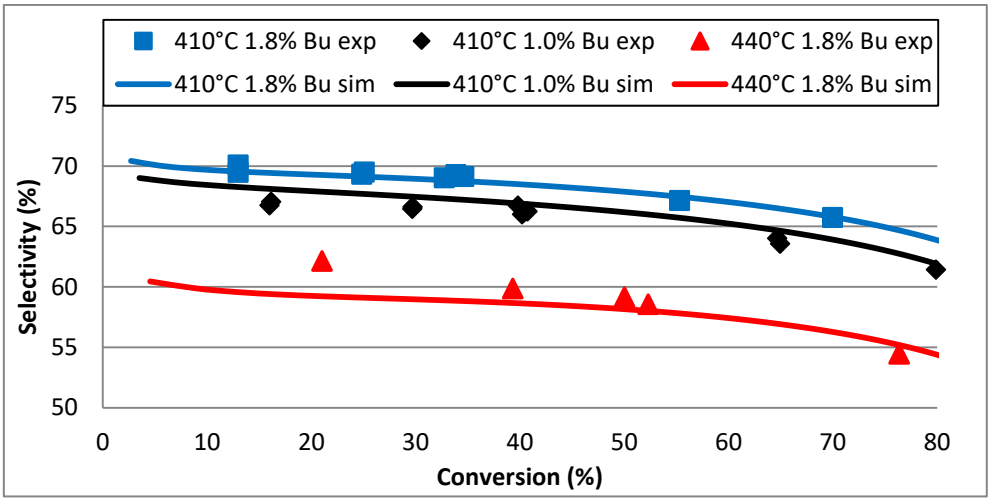

Fig. 24: Measured and simulated MA selectivity-conversion plots at different SBT and *n*-butane inlet concentrations. Simulation: *HW3* model, 165 kg/m³ catalyst *C1*.

The parity plots too, which are shown for the *HW3* model in Fig. 25, indicate very good fits as deviations between model and experimental values are mostly within 10 % (solid lines). This also suggests that a too high variance of the CO and CO_2 analysis and the too low number of measurements at low conversions eliminate the statistical significance of the experimental observations in the CO/CO_2 profiles.

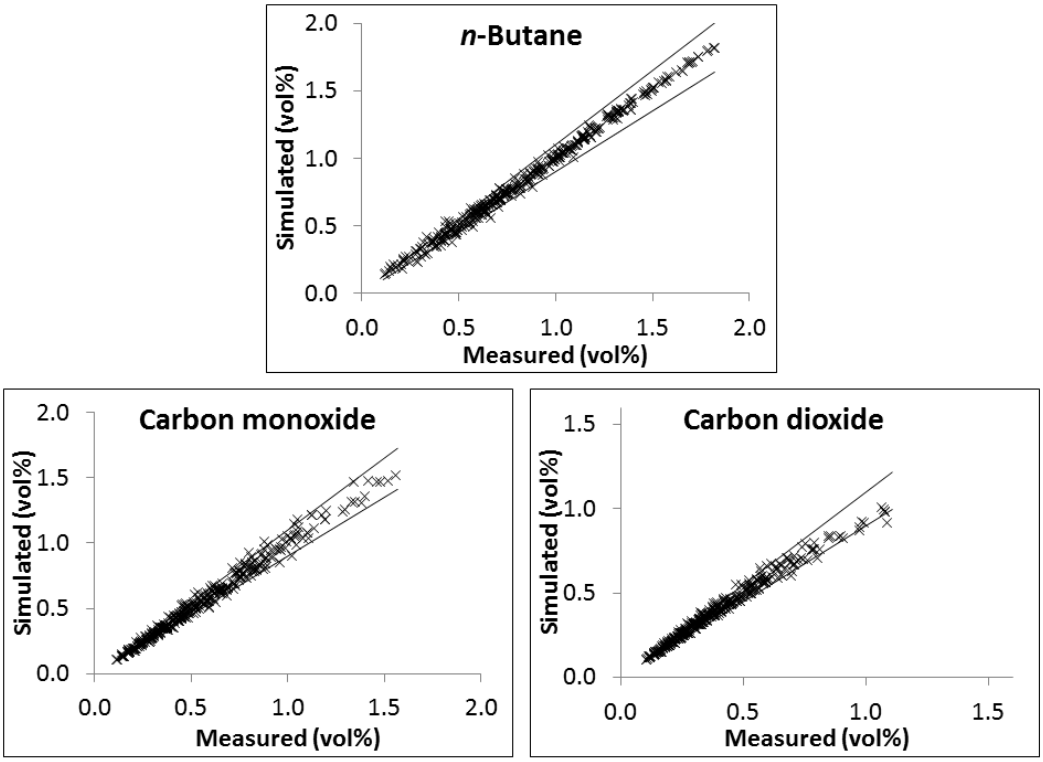

Fig. 25: Parity plot of the measured outlet concentrations of *n*-butane, CO and CO_2 for the *HW3*-model (solid lines mean 10 % deviation).

The optimum parameters are given in Tab. 6. As the purpose of the presented kinetic study however is the simulation of the applied pilot reactor in which significant temperature profiles form, a quantitatively correct description of the selectivity profiles is considered to be of high importance. This is debt to the huge differences in reaction enthalpy of the MA, CO and CO_2 formation reactions, which thus have an important influence on form and magnitude of the temperature profile in the industrial reactor. Hence, the *HW3* model should be most suitable for this purpose. For the sake of completeness the parameter estimation results for the other models can be found in the appendices (A.5).

The 95 % confidence intervals appear relatively high, marking deviations up to 40 % of the optimum estimates. The determined activation energies are in the same range as compared to literature steady state kinetic models [23,28,33]. According to the findings of Brandstädter [23],

and Sharma *et al.* [33], and also in agreement with the experimental observations in this work (2.5.2), the non-selective oxidations present higher activation energies than the selective reaction path. Also the lower value of the inhibition constant for water as compared to *n*-butane was reported in the works of [23,28]. The *n*-butane inhibition of the CO producing reactions is only slightly higher than that for the other reactions. According to Fig. 23 this difference is not sufficient in order to correctly describe the observed CO_x-profiles which was the initial purpose of introducing this additional inhibition constant. On the other hand, the *HW3* model still gives the best results in terms of parity plots and reproduction of selectivity profiles.

Tab. 6: Parameter estimation results for the *HW3* model

	Parameter	Unit	Optimal Estimate	Confidence Interval (95%)
1	$E^A_{Bu,MA}$	kJ/mol	86.6	7
2	$E^A_{Bu,CO}$	kJ/mol	105.3	8
3	E^A_{Bu,CO_2}	kJ/mol	108.2	14
4	$E^A_{MA,CO}$	kJ/mol	105.5	44
5	E^A_{MA,CO_2}	kJ/mol	119.7	32
6	$K_{Bu,2}$	bar^{-1}	429.3	130
7	K_{H_2O}	bar^{-1}	88.4	18
8	$K_{Bu,1}$	bar^{-1}	399.2	120
9	$k^{ref}_{Bu,MA}$	10^{-3} mol/s/kg/$bar^{1.5}$	663.0	150
10	$k^{ref}_{Bu,CO}$	10^{-3} mol/s/kg/$bar^{1.5}$	114.5	43
11	k^{ref}_{Bu,CO_2}	10^{-3} mol/s/kg/$bar^{1.5}$	68.2	19
12	$k^{ref}_{MA,CO}$	10^{-3} mol/s/kg/$bar^{1.5}$	35.6	4
13	k^{ref}_{MA,CO_2}	10^{-3} mol/s/kg/$bar^{1.5}$	29.4	3
14	τ	-	2.5	0.3

Minor correlations appeared when any of the kinetic models was applied. In case of *HW3*, correlations appeared between the inhibition constant $K_{Bu,1}$ and the kinetic constants for the formations of MA and CO_2 from *n*-butane, $k^{ref}_{Bu,MA}$ and k^{ref}_{Bu,CO_2}, as well as between the activation energies of both CO producing reactions (Tab. 7). Beside of the huge number of included measurements, which should imply higher measurement variances, the reasons for

these statistical inconsistencies may be various. One is certainly the lack of experiments in which MA and water are fed, as this was not possible with the employed bench reactor. Such experiments would surely improve the estimation of inhibition constants, so as the kinetics of MA decomposition. Also the observed activating and deactivating effects during the different bench tests (section 2.5.1) should have an influence on the parameter estimation results.

With respect to the influence of pore diffusion on the overall reaction rates, the estimated value for the tortuosity factor is 2.53, which is within the typical range [16]. In order to quantify the diffusional resistances for each catalyst shape, pore efficiency factors may be calculated according to equation (3-44). Values ranged between 23 % and 55 %, whereas the lower bound corresponds to high reaction temperatures. Average pore efficiency factors at 410°C SBT are presented in Tab. 8. Obviously, the observed performance order (section 2.5.3) is not reproduced by the pore efficiency factor, but by the BET surface area. This means that the higher BET surface area of the *C5* shape improves both, activity and selectivity of the catalyst.

$$\eta_{i,j}^{P} = \frac{\frac{1}{V_p}\int r_{i,j} dV_p}{r_{i,j}^{sf}} \tag{3-44}$$

It can be concluded that the available bench reactor configuration, whose purpose is the screening of catalysts, is not completely suitable for detailed kinetic modeling because of the following reasons. It was not possible to establish isothermal conditions without risking channeling effects in the diluted catalyst beds. Additionally, the reactor setup did not permit the dosage of reaction products to the reactor, which would be necessary in order to doubtlessly identify the reaction network, as well as the influence of reaction products on particular reaction paths and product distribution. It would also serve for a more accurate determination of the MA decomposition kinetics. Another important aspect is the apparently changing catalyst performance with time on stream during some of the experiments. The limited availability of the reactor may be mentioned as a further constraint. Because of high utilization of the reactor for different research purposes, no further experiments at low conversions could be performed.

Nevertheless, it must be emphasized that despite these constraints, the variety of experiments could be described very well by the model developed. Taking into account the large number of included experiments, the parity plots (Fig. 25) confirm a very good fit. Although the exact trends in the observed CO/CO_2 profiles could not be reproduced completely, the quantitative deviations are minor. Additionally, the excellent description of pore diffusion limitations must be highlighted. Applying an effective Fickian diffusion model, various different particle geometries could be described with one kinetic model. This was possible by using spherical and cylindrical pellet models with equivalent particle geometries for the different shapes.

Tab. 7: Correlation matrix for the *HW3* model

	1	**2**	**3**	**4**	**5**	**6**	**7**	**8**	**9**	**10**	**11**	**12**	**13**	**14**
1	1.00													
2	-0.39	1.00												
3	-0.40	0.15	1.00											
4	0.49	0.94	-0.17	1.00										
5	0.42	-0.15	-0.95	0.20	1.00									
6	-0.10	-0.15	0.03	0.05	-0.07	1.00								
7	0.20	0.12	0.03	0.02	0.05	-0.30	1.00							
8	0.10	0.12	0.01	0.01	0.07	-0.64	0.78	1.00						
9	0.12	0.17	0.04	-0.02	0.04	-0.60	0.88	0.95	1.00					
10	0.01	-0.21	0.03	0.19	-0.01	0.78	0.27	-0.02	-0.01	1.00				
11	0.18	0.09	-0.19	0.04	0.28	-0.59	0.78	0.96	0.91	0.01	1.00			
12	0.12	0.40	0.03	-0.29	0.03	-0.78	0.67	0.71	0.80	-0.47	0.68	1.00		
13	0.05	0.13	0.44	-0.05	-0.45	-0.04	0.68	0.36	0.54	0.25	0.20	0.44	1.00	
14	0.24	0.04	-0.03	0.08	0.09	-0.32	0.34	0.43	0.56	-0.04	0.43	0.45	0.29	1.00

Tab. 8: Average pore efficiency factors at 410°C SBT, 165 kg/m³ catalyst and 1.8 vol% *n*-butane

Catalyst shape	Observed performance	Efficiency factor $\eta^{P}_{Bu,MA}$	Normalized BET surface area $\overline{BET}$
		%	m²/g
C6	1	41.5	1.15
C5	2	50.8	1.02
C1	3	43.6	1.00
C2	4	38.0	1.00

* The normalized value $\bar{A}_i$ of a parameter A_i is defined as the ratio between A_i and a reference value A_i^{ref}. BET^{ref} = 24.3 m²/g.

As the purpose of the kinetic experiments was to obtain a simple kinetic model, which can be applied to different VPO catalyst shapes in an industrial scale fixed bed pilot reactor, the modeling results of this section are thus absolutely satisfactory. For more detailed studies of micro kinetics and reaction mechanism, different kind of experiments would be necessary in more appropriate reactor types, such as differential reactors or micro-structured reactors which present improved heat and internal mass transfer characteristics as shown by Guettel and Turek [58].

4 Phosphorus Dynamics

4.1 Introduction

The patent literature offers some clues about the causes and consequences of the dynamic behavior of VPO catalysts in the commercial MA production. Becker *et al.* [9] found that the MA yield can be optimized at established reactor operation, introducing continuously an amount of a suitable phosphorus compound. They assume that the catalyst loses phosphorus at a small level and that this loss is associated with a decreasing catalyst performance. Thereby, the selectivity and the temperature necessary to obtain the desired conversion decrease. The authors observed that the addition of phosphorus prevents a decline in selectivity without increasing significantly the necessary reactor temperature.

Click *et al.* [10] claimed steam regeneration of their phosphorus treated VPO catalysts in a fixed-bed reactor. They found that after the successive treatment with a phosphorus compound and steam the temperature profile of the fresh catalyst could substantially be restored increasing again selectivity and yield. The steam was supposed to remove phosphorus from the inlet part distributing it to the remainder of the catalyst bed.

Edwards *et al.* [11] claimed continuous regeneration of the catalyst in a fixed-bed reactor by feeding a hydrocarbon ester of phosphoric acid together with water. The addition of these compounds would serve to deactivate high temperature regions moving the hot spot towards the center. The resulting more isothermal temperature profile would facilitate a further increase of the MA-yield.

Ebner *et al.* [12] found an optimum range for the dosage of trimethyl phosphate (TMP) in the fixed bed reactor in order improve the performance of the VPO catalyst. They also assumed loss of phosphorus of the catalyst displacing the P/V-ratio into a region less favorable to selectivity. The sorption of the added phosphorus may restore the optimum P/V-ratio. The incorporation of moisture into the feed was supposed to promote the distribution of phosphorus over the catalyst bed as it would adsorb excessively in the inlet zone if water in the gas stream was absent.

Haddad *et al.* [13] improved the performance of a fluidized bed reactor by adding catalyst particles to the reactor, previously impregnated with an alkyl ester of phosphoric acid. This procedure presented the advantage of not having to increase the reaction temperature as it is necessary in case of a continuous phosphorus addition.

Reaction mechanism and nature of the active vanadium phases on the VPO surface have been debated for decades but they are still not fully resolved. Several faces of the vanadium pyrophosphate crystals and different redox couples have been proposed while during the last decades different orthophosphate species and their role in the reaction mechanism were discussed [6,7,18,22,39,40,42,59–63]. A particular subject of the debate, however, is the theory that a highly dynamic surface forms on the vanadium pyrophosphate (VPP) precursor under reacting conditions, which is composed of various VPO phases [39,40,64] as a function of

operating conditions. With respect to the phosphorus issue in the commercial application, an important aspect of this view on the catalyst surface is the role of water during these dynamic changes. It is supposed that water promotes the formation of surface phosphates which in turn may be released to the gas phase [24,64–66].

Regarding the relation between phosphorus content and catalyst performance, it is generally assumed that excess phosphorus prevents the oxidation of VPP (V^{4+}) to V^{5+}-species [6,40,52,67] which often have been detected under reacting conditions [39,40,59,60]. On the other hand, an irreversible loss of phosphorus was related to catalyst deactivation by formation of V_2O_5 [68]. Selectivity too was found to depend on the P/V ratio of the catalyst [7,18,39,40]. Important, more recent works on this topic are those of Cavani *et al.* [39,40], who found varying surface compositions with different activity-selectivity relationships as a function of P/V ratio and reaction conditions. It is worth noting that commercial VPO catalysts usually have a slight excess of phosphorus as compared to the stoichiometric amount (P/V 1) [3].

From a variety of *in situ* analyses of the working VPO surface it was additionally concluded that structure and composition of the active VPO surface vary as a function of reaction conditions [24,39,40,64–66,69]. A significant enrichment of phosphorus on the surface is an important observation [64–66]. Further, the influence of water, which is always present as a reaction product, on the surface dynamics is strongly related to these findings. On the one hand, water was found to reduce reaction rates and to affect the selectivity by adsorption on surface sites [28,41,45]. Furthermore, water was reported to facilitate re-oxidation of the catalyst [65,66,70] and to promote the formation of separated phosphate species on the surface [24,64], which is in turn related to the phosphorus enrichment [65,66]. The works of Cavani *et al.* [39,40] additionally suggest a direct influence of water on the appearance of different orthophosphates.

Debating the role of water for the mobility of phosphorus in the catalyst, Cavani *et al.* [40] proved the ability of removing phosphorus from the catalyst by treatment with water. This finding thus is directly related to the conclusion of the patent literature that the addition of water is necessary for an adequate distribution of phosphorus in the catalyst bed [10,11].

However, beyond the information provided by patents, scientific literature could not be found on more precise investigations with respect to the addition of phosphorus to fixed bed reactors. In the area of micro-scale reactor studies [40,65], there are only a few studies which touch this subject. In addition, the operating conditions which were typically applied in laboratory reactors generally permit long-term operation without significant changes of the catalyst activity [43].

In this work, elaborated experiments in an industrial scale fixed bed pilot reactor are presented during which the influences of phosphorus and water on the transient reactor behavior were studied. To this end, an industry-like VPO catalyst was used. The experimental observations are discussed in the frame of the apparently contradictory debates in the scientific literature about the functionality of the VPO surface during *n*-butane oxidation.

4.2 Experimental

Dynamic experiments were carried out in a continuous flow fixed bed pilot reactor of industrial dimensions, which is schematically presented in Fig. 26. The reactor tube has an inner diameter of 21 mm and is welded into a stirred tank containing molten salt. The reactor loading consists of a preheating zone comprising inert rings, the catalyst bed, and finally another inert section. The preheating zone assured that the gas reached the temperature of the salt bath before entering the catalyst bed. A movable single-point thermocouple is centered in a 3 mm well along the tube axis (Fig. 27) and facilitates the measurement of axial temperature profiles. These measurements are automated in a manner, which allows the recording of complete temperature profiles in certain time intervals.

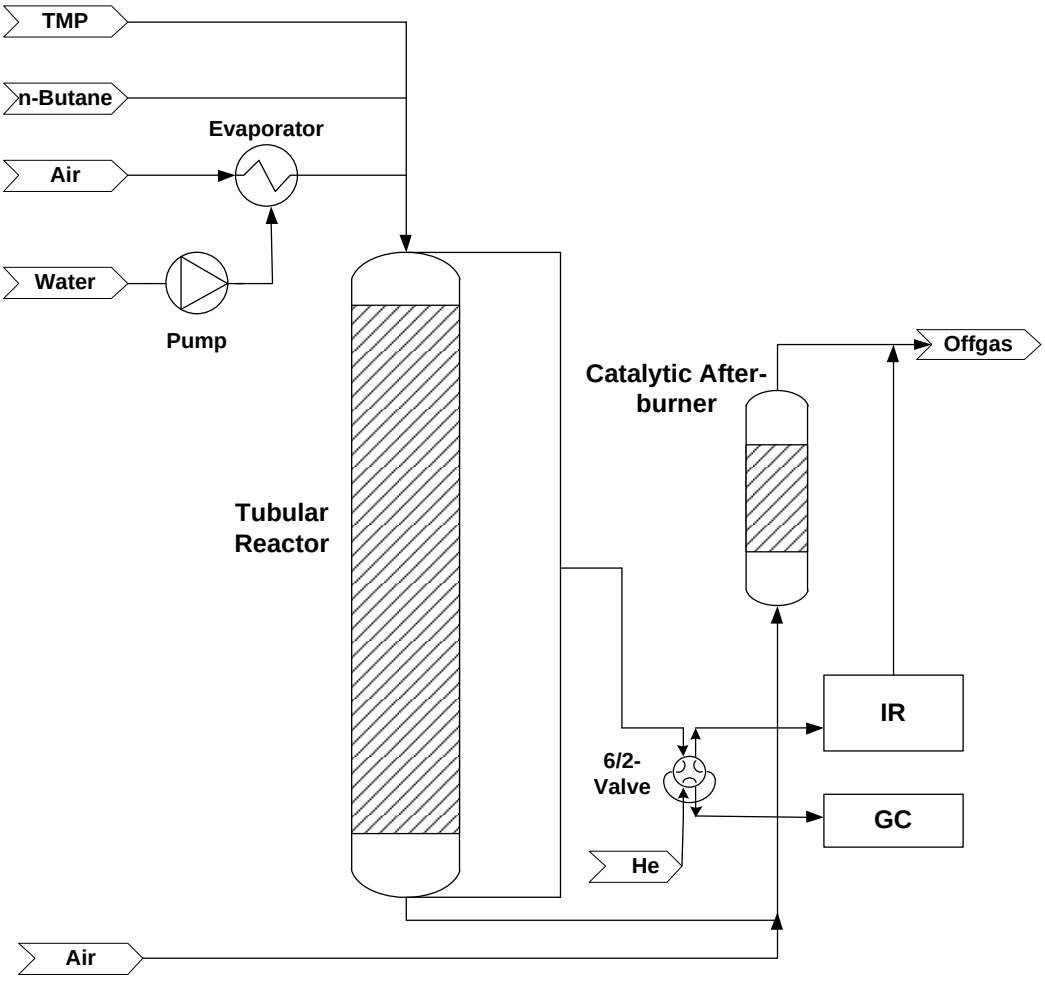

Fig. 26: Process flow diagram of the pilot reactor.

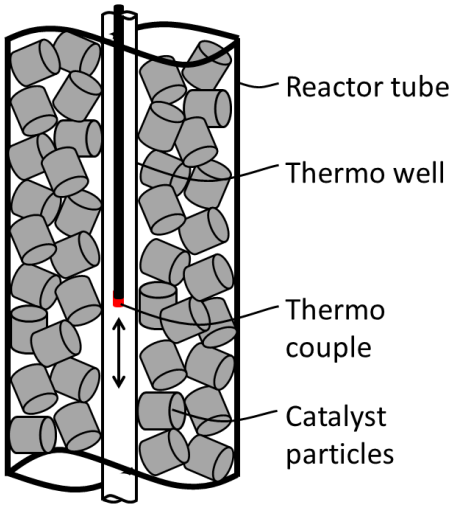

Fig. 27: Sketch of the interior of the reactor tube.

The feed section comprises four components for the delivering of air, *n*-butane, steam and trimethyl phosphate (TMP) which serves as phosphorus source. The flow rates of air and *n*-butane are controlled by mass flow controllers (Brooks). The steam feed is generated at 120°C in an evaporator filled with silicon carbide particles. Demineralized water is supplied by a HPLC pump. The TMP saturator consists of a storage tank from where the TMP is pushed by nitrogen into a temperature-controlled, double-walled glass cylinder. The TMP partial pressure is adjusted by the temperature of the water heating jacket. Vapor pressure calculations are based on the Antoine equation with constants for trimethyl phosphate found in [71]. Due to the lack of appropriate analysis devices, the real TMP concentration could not be detected, either at the entrance or at the outlet of the reactor. If the TMP stock reaches its minimum filling level the nitrogen flow has to be interrupted during the refilling process which may take up to 5 min. All inlet and outlet lines are heated in order to avoid condensation of any compounds.

A catalytic total combustion unit downstream the reactor oxidizes CO and any organics to CO_2 and water before venting to the atmosphere. Pressure transducers are installed at the inlet and outlet line of the reactor in order to determine the pressure drop across the reactor. The operation pressure is controlled by means of a pressure relief valve, which is situated in the outlet line. The complete process control including industrial safety standards is realized in a programmable control system (Siemens S7) ensuring non-stop operation.

Analysis of gas composition at inlet and outlet is fully automated. The analysis unit comprises an infrared analyzer (Emerson NGA2000) for the measurement of *n*-butane, CO and CO_2, and a standard gas chromatograph (Agilent 6820N) using a capillary column (Restek RTX 1701, 30 m) for the measurement of *n*-butane, MA as well as acrylic, and acetic acid. A proper control system permits either manual measurements or the programming of fully automated measurement cycles ensuring the possibility of acquiring concentration data in 24/7 mode.

4.3 Dynamic experiments

A series of experiments were carried out applying the two ring shaped catalyst samples *C5* and *C6* (section 2.3). The catalyst bed length was about 3.5 m in every case. In the following, four pilot tests are considered. *PT1* and *PT2* were performed with catalyst *C5*, and *PT3* and *PT4* with catalyst *C6* respectively. Tab. 9 presents the applied experimental conditions, which are also typical for industrial practice. At these conditions, the particle Reynolds numbers were always higher than 500, and the Bodenstein numbers were around 2000 because of which channeling and dispersion effects can be excluded. Prior to catalyst performance trials, a blind test during which the reactor was filled with inert material only, did not show any conversion of reaction educts by the reactor device.

Tab. 9: Experimental conditions

Salt bath temperature (SBT)	°C	380 – 410
Relative inlet pressure	bar	1.45 – 1.65
Gas hourly space velocity (GHSV)	h^{-1}	2190 – 2610
Butane fraction	vol%	1.5 – 2
Water fraction	vol%	0 – 4
TMP fraction	ppmv	0 – 7

A series of test runs was conducted to investigate the effect of TMP and water on the performance of the VPO catalyst. Each test run took several weeks. The experimental plan comprised the following stages:

- Start-up (S/U) and equilibration phase during which only *n*-butane, water, and air were fed to the reactor until reaching steady state operation for different reference conditions
- Variation of operating conditions without addition of TMP (during some test runs only)
- Addition of TMP
- Variation of operating conditions including TMP and water feed concentrations

During these experiments, the initial S/U conditions were periodically reset for reference and to determine irreversible catalyst deterioration. Each operating condition was held for different time intervals during which temperature and concentration measurements were carried out

periodically. The following section 4.4 presents excerpts of the extensive, performed experiments, which representatively resume the most important observations.

4.4 Experimental results

4.4.1 Start-up behavior and equilibration without TMP addition

Operating conditions and performance data for the following examples are given in Tab. 10. During initial operation, hot spot temperature (HST) and *n*-butane conversion (*X*) declined with time, while the selectivity to MA increased. This is shown in Fig. 28 for test *PT1*. The main observed side products were CO and CO_2, which showed formation rates decreasing with time on stream (TOS). Acrylic and acetic acid were detected too, but with selectivities never exceeding 1.5 vol% each. A pronounced temperature hot spot developed at the entrance of the catalyst bed (Fig. 29). After a time period of about 40 h, a first steady operational state appeared for which conversion and hot spot temperature were about 9 % and 15°C lower than directly after start-up. The selectivity to MA increased by about 6.5 % while the formation of CO and CO_2 decreased about 6.2 and 2.6 %, respectively. It is worth noting that the velocity of the initial deactivation was found to be function of operating conditions. During the initial operation of *PT2* without TMP, the maximum catalyst temperature was constantly around 430°C as the SBT was kept at 395°C and the *n*-butane inlet concentration at only 1.5 vol%. The first operational steady state was not reached before after 120 h. In contrast, during *PT1* and *PT3*, SBT and *n*-butane concentration were 400°C and 1.7 vol% respectively.

Tab. 10: Operating conditions (C_4H_{10}, H_2O, TMP: Inlet concentrations of *n*-butane, water and TMP) and performance data (*X*: *n*-butane conversion, *S*(MA): Selectivity to MA) for presented experiments during start up equilibration

Oper-ating point	Test	TOS	GHSV	SBT	C_4H_{10}	H_2O	TMP	*X*	*S*(MA)
		h	h^{-1}	°C	vol%	vol%	ppmv	%	%
1-1	*PT3*	1	2180	400	1.7	2	0	93.3	63.9
1-2	*PT3*	69	2180	400	1.7	2	0	84.7	70.4
2-1	*PT1*	25	2610	400	1.8	2	0	79.3	72.1
2-2	*PT1*	120	2610	400	1.8	2	0	72.6	74.0
2-3	*PT1*	191	2610	400	1.8	2	0	73.0	73.5

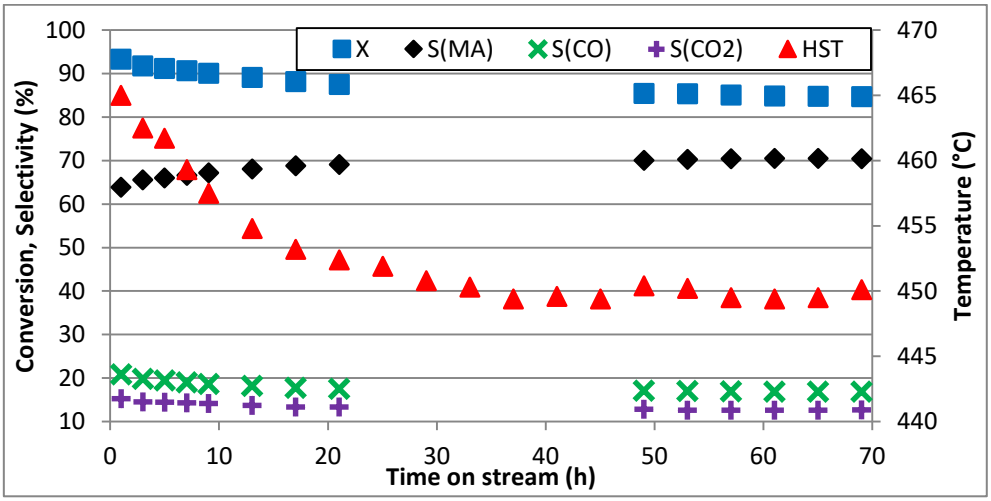

Fig. 28: Conversion (*X*), selectivity to MA, CO and CO_2 (*S(MA)*, *S(CO)*, *S(CO_2)*) and hot spot temperature (HST) during the equilibration of *PT3* according to operating points 1-1 to 1-2 in Tab. 10.

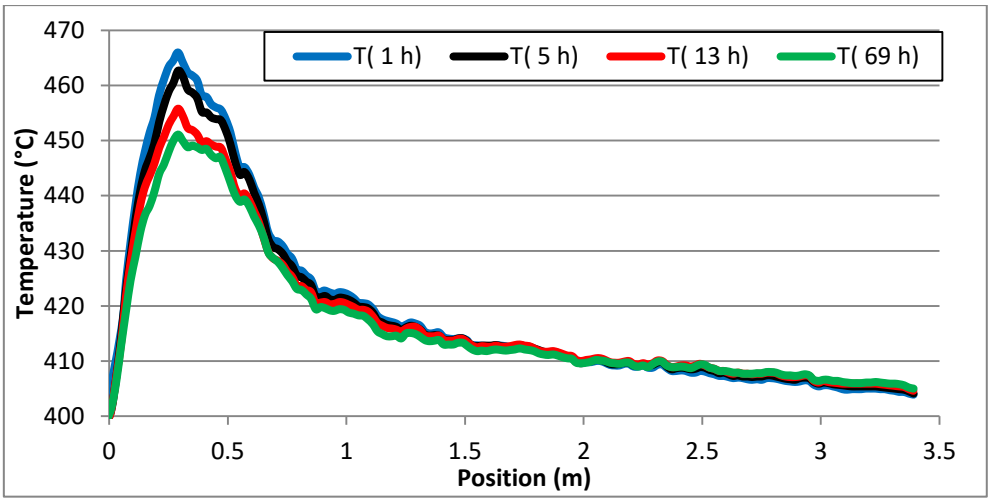

Fig. 29: Temperature profiles for different times on stream during the S/U equilibration of *PT3* according to operating points 1-1 to 1-2 in Tab. 10.

The stability of the first steady operational state too was found to be a function of time and operating conditions. When the reactor was operated for long time periods without TMP addition, the hot spot temperature started to rise again, as illustrated in Fig. 30 for *PT1*, while form and position of the temperature hot spot remained unchanged. At the same time, a very slight gain in conversion and loss in selectivity was observed. Accordingly, the respective temperature profiles reveal that it was only the hot spot temperature which increased again, but not the area below the temperature profile (Fig. 31) which is indicative of *n*-butane conversion and selectivity ratios. The rate of this change in catalyst performance again was

observed to increase with rising hot spot temperature. When the maximum temperature was kept below 430°C, a catalyst reactivation after the initial deactivation period could not be detected during almost 300 h of operation without TMP. On the other hand, when the maximum temperature was in the range of 440°C and it started to increase again after only 60 to 100 h (Fig. 30). This indicated an important temperature effect on catalyst activation in absence of P-dosing.

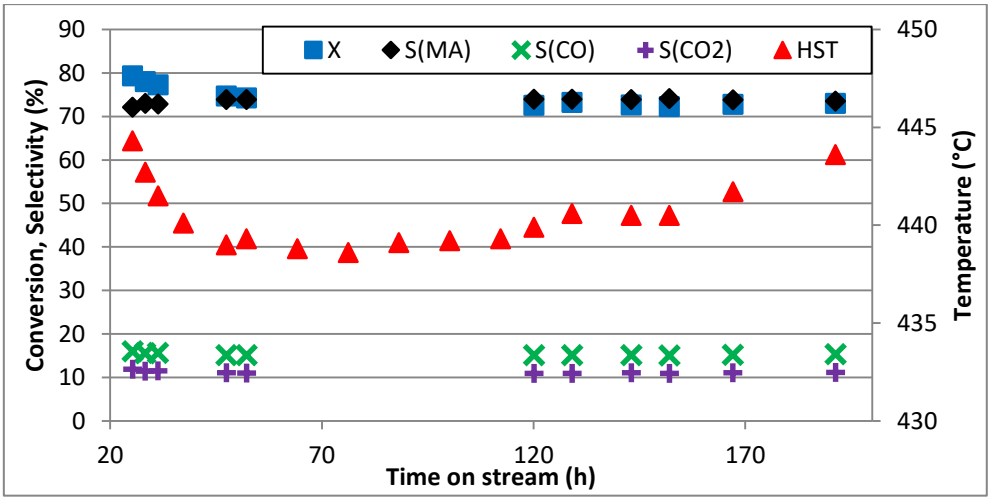

Fig. 30: Conversion (*X*), selectivity to MA, CO and CO_2 (*S(MA)*, *S(CO)*, *S(CO_2)*) and hot spot temperature (HST) during the initial operation without TMP according to operating points 2-1 to 2-3 in Tab. 10.

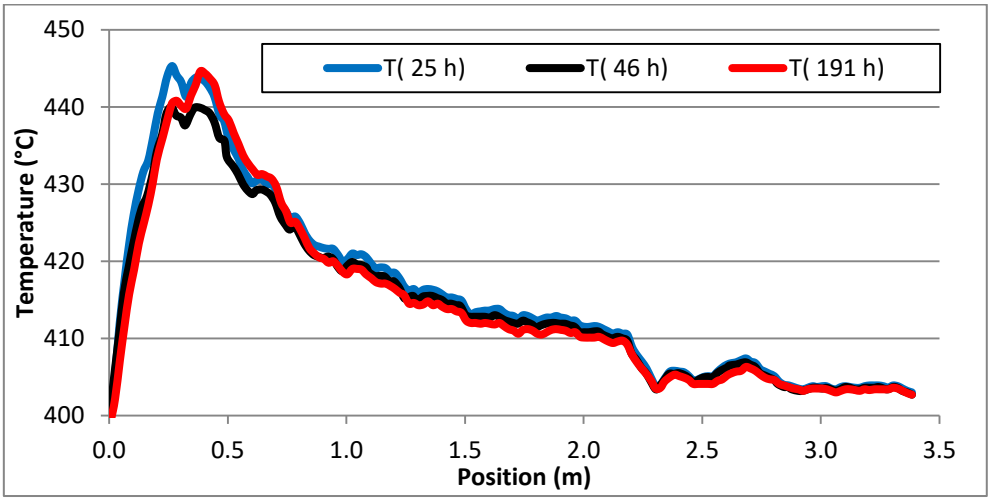

Fig. 31: Temperature profiles at the beginning of *PT1* (*blue*), during the first steady state (*black*) and after reactivation (*red*) according to performance in Fig. 30.

4.4.2 Influence of trimethyl phosphate

Operating conditions and performance data for the following examples are given in Tab. 11. Fig. 32 shows the progression of the temperature profiles when continuously adding about 5 ppm TMP to the reactor feed under equilibrating conditions after 191 h TOS. The hot spot started to decline slowly, becoming flatter and broader with TOS. 24 h after starting TMP addition, the temperature maximum was reduced by about 27°C, the conversion declined about 10.7 %, while the selectivity increased by about 3.3 %. Although around 20 h after starting the TMP addition, a new steady state was approached, a very slowly proceeding temperature reduction was still observed even after 60 h. The magnitude of these changes was found to depend strongly on the TMP amount. Less TMP in the feed caused lower absolute temperature reductions, as illustrated for PT3 in Fig. 33, for which only about 1.5 ppm TMP were added at 75 h TOS. During the following 25 h, the hot spot temperature dropped only by about 10°C and thereafter remained almost constant even 66 h after starting P addition. Respectively, the changes in conversion (-2.9 %) and selectivity (+1.1 %) were minor too. Despite the differences, both pilot tests show that the added phosphorus reduces significantly the activity of the catalyst in the inlet section, where initially the hot spot was situated.

Tab. 11: Operating conditions (C_4H_{10}, H_2O, TMP: Inlet concentrations of *n*-Butane, water and TMP) and performance data (*X*: *n*-Butane conversion, *S*(MA): Selectivity to MA) for presented TMP experiments

Oper-ating point	Test	TOS	GHSV	SBT	C_4H_{10}	H_2O	TMP	*X*	*S*(MA)
		h	h^{-1}	°C	vol%	vol%	ppmv	%	%
2-3	*PT1*	191	2610	400	1.8	2	0	73.0	73.5
2-4	*PT1*	215	2610	400	1.8	2	5	62.3	76.8
2-5	*PT1*	317	2610	400	1.8	2	5	60.3	76.9
2-6	*PT1*	359	2610	400	1.8	2	0	72.8	73.2
3-1	*PT3*	75	2180	400	1.7	2	0	84.7	70.4
3-2	*PT3*	140	2180	400	1.7	2	1.5	81.8	71.5

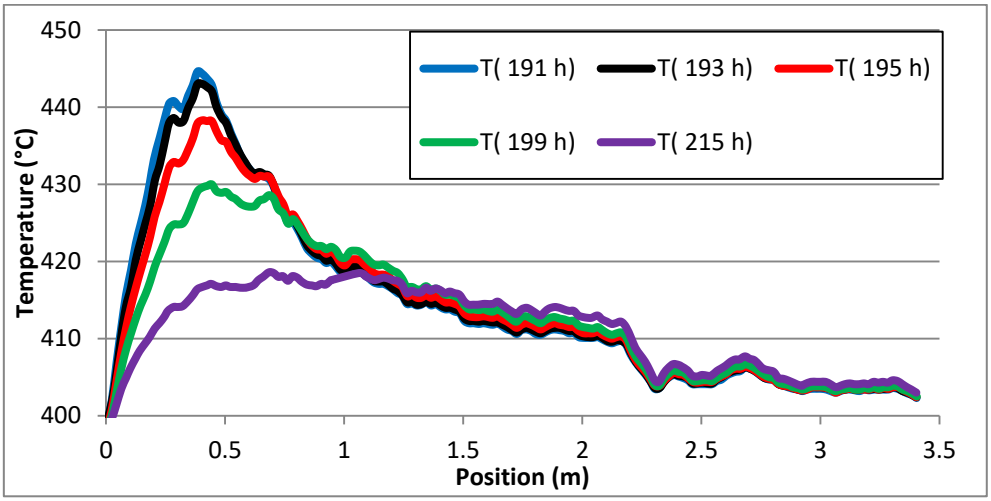

Fig. 32: Progression of the temperature profile after adding ca. 5 ppm TMP at 191 h TOS according to operating points 2-3 to 2-4 in Tab. 11.

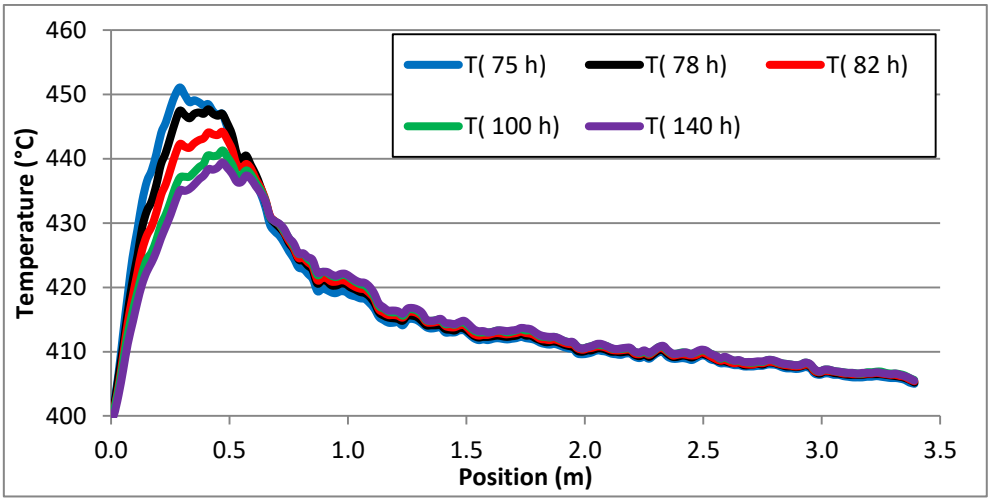

Fig. 33: Progression of the temperature profiles of *PT3* after adding ca. 1.5 ppm TMP after 75 h TOS according to operating points 3-1 to 3-2 in Tab. 11.

Another important aspect regarding the dynamics of this deactivation is illustrated in Fig. 34, which presents the progression of the hot spot temperatures after adding TMP in *PT1* and *PT3*. In case of *PT1*, the initial gradient of the temperature drop is lower and shows an inflection point before steady state is reached, while, in *PT3*, the gradient is highest at the beginning of the TMP addition. This, remembering the situation before TMP addition, may be explained by the fact that this is the equilibration phase as presented in section 4.4.2. As indicated in Fig. 28 and Fig. 30, the hot spot temperature in *PT1* finally increased again while this was not the case in *PT3*. Hence, the slower kinetics of the hot spot reduction is the result of an activating and a simultaneous deactivating effect. This dependence of the dynamics on the actual previous

history of the catalyst could be further confirmed in many different situations throughout all experiments.

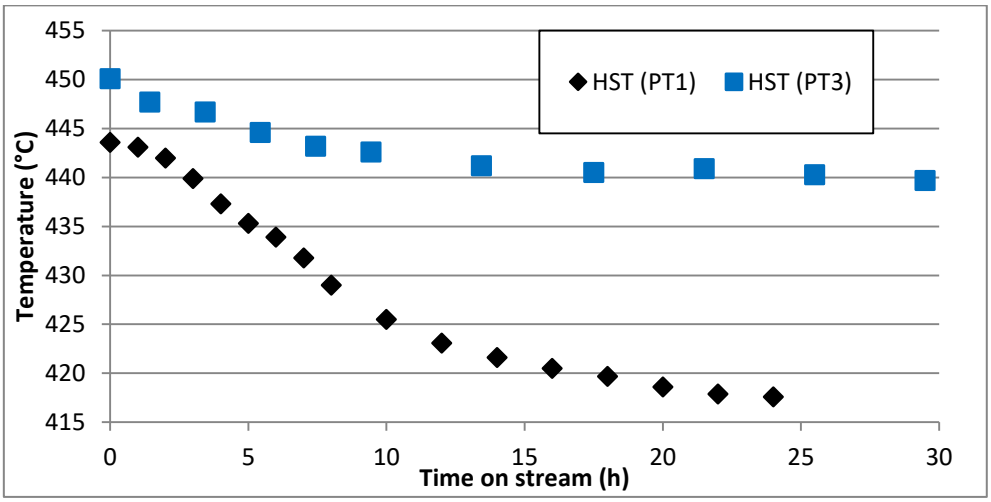

Fig. 34: Progression of the hot spot temperatures of *PT1* and *PT3* subsequent to TMP addition after having reached steady state operation.

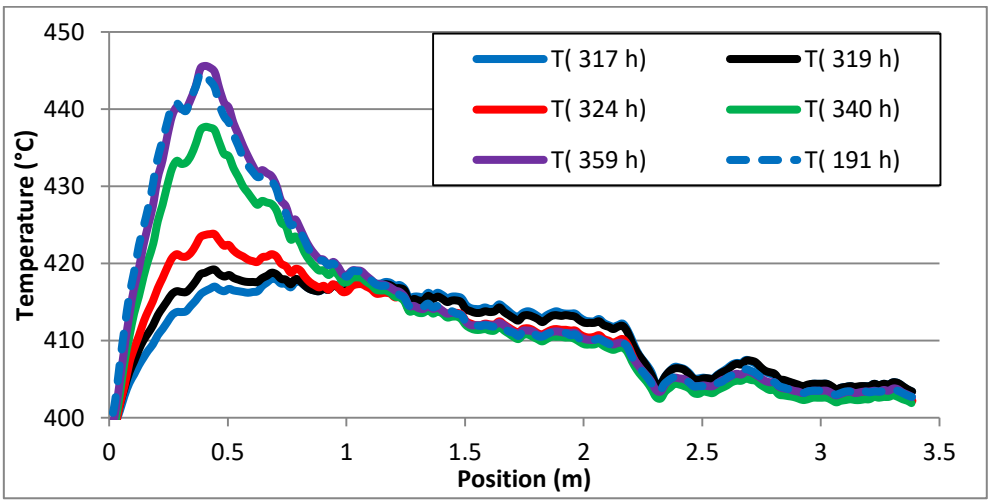

Fig. 35: Progression of the temperature profiles after stopping the TMP feed at 317 h TOS under equilibration conditions according to operating points 2-3, 2-5 and 2-6 in Tab. 11.

The reversibility of this effect is exemplarily demonstrated for *PT1* in Fig. 35. In this experiment, the TMP feed of about 5 ppm was completely stopped after 317 h TOS, while the remaining conditions were the same as during equilibration. The temperature of the hot spot started to rise and the originally observed hot spot developed again. MA selectivity and *n*-butane

conversion too approached their original values. About 42 h after stopping TMP addition, the temperature profile measured at the end of equilibration was almost reproduced, and all previously introduced phosphorus seemed to be removed again from the catalyst surface. The hot spot temperature finally was even 1 K higher indicating that the local activation within the hot spot zone continued, which was observed too after long-term equilibration without TMP.

4.4.3 Influence of water

Operating conditions and performance data for the following examples are given in Tab. 12. An important claim in the patent literature relates to the additional need of water in the reactor feed for the purpose of an optimal distribution of the phosphorus over the catalyst bed [10,12]. The addition of water alone was reported to intrinsically inhibit the reaction, but also to have multiple effects on the catalytic selectivity [28,41,45]. In order to investigate these aspects, the concentrations of TMP and water were independently varied and the dynamic response of the catalyst was observed during several hours until days.

When the water concentration was raised during the first operational steady state phase without addition of TMP, the hot spot temperatures were found to instantaneously decrease and to subsequently remain constant even 10 h after the step change. This effect was completely reversible (Fig. 36).

On the other hand, the situation changed when TMP was simultaneously fed, as exemplarily demonstrated by the following experiment. The temperature profile in Fig. 37 indicated by a blue line (T(198 h)) presents a stable operating state at which the catalyst had been exposed to TMP for several hours. The simultaneous constant feed of 3 vol% water was then stopped after 198 h operating hours. Because the reaction was less inhibited after stopping the water feed, the temperature first increased, which was visible during about one hour after the step change. But then the hot spot started to decline and to move towards the center of the catalyst bed. The temperature profile indicated by a dashed blue line, named T(314 h), illustrates this case. The temperature profile became very flat and the hot spot originally seen completely disappeared. According to the changing temperature profiles, the conversion first increased about 4 % and then decreased about more than 10 %. The selectivity changed inversely proportional about 2 % and 3 % respectively.

Tab. 12: Operating conditions (C_4H_{10}, H_2O, TMP: Inlet concentrations of *n*-Butane, water and TMP) and performance data (*X*: *n*-Butane conversion, *S*(MA): Selectivity to MA) for presented water experiments

Oper-ating point	Test	TOS	GHSV	SBT	C_4H_{10}	H_2O	TMP	*X*	*S*(MA)
		h	h^{-1}	°C	vol%	vol%	ppmv	%	%
4-1	*PT4*	96	2470	400	1.7	2	0	82.8	68.8
4-2	*PT4*	98	2470	400	1.7	4	0	79.6	70.4
4-3	*PT4*	116	2470	400	1.7	4	0	79.1	70.8
5-1	*PT3*	198	2190	400	1.7	3	3	80.4	72.5
5-2	*PT3*	199	2190	400	1.7	0	3	84.5	70.8
5-3	*PT3*	314	2190	400	1.7	0	5	66.2	75.9
6-1	*PT1*	624	2610	410	1.8	2	5	66.9	74.6
6-2	*PT1*	625	2610	410	1.8	4	5	63.8	75.8
6-3	*PT1*	647	2610	410	1.8	4	5	69.1	74.6

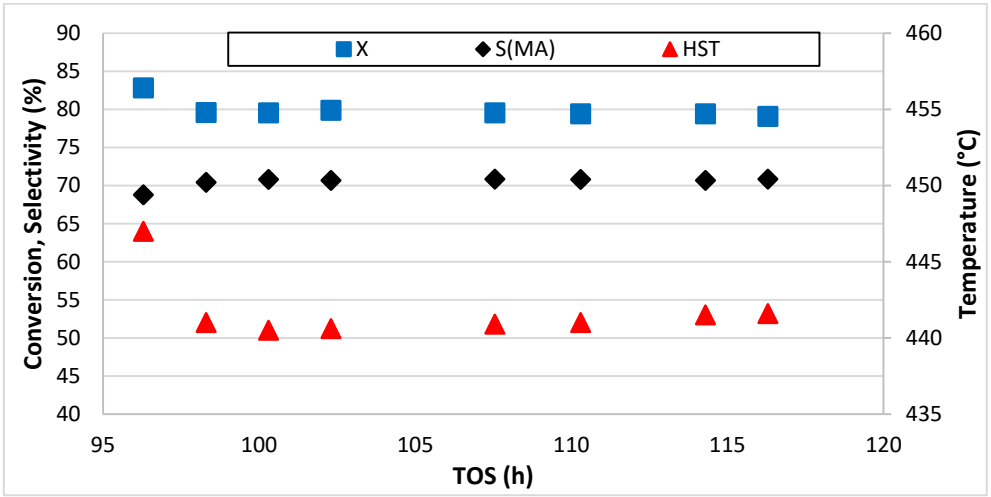

Fig. 36: Conversion, selectivity and hot spot temperature after increasing water feed according to operating points 4-1 to 4-3 in Tab. 12.

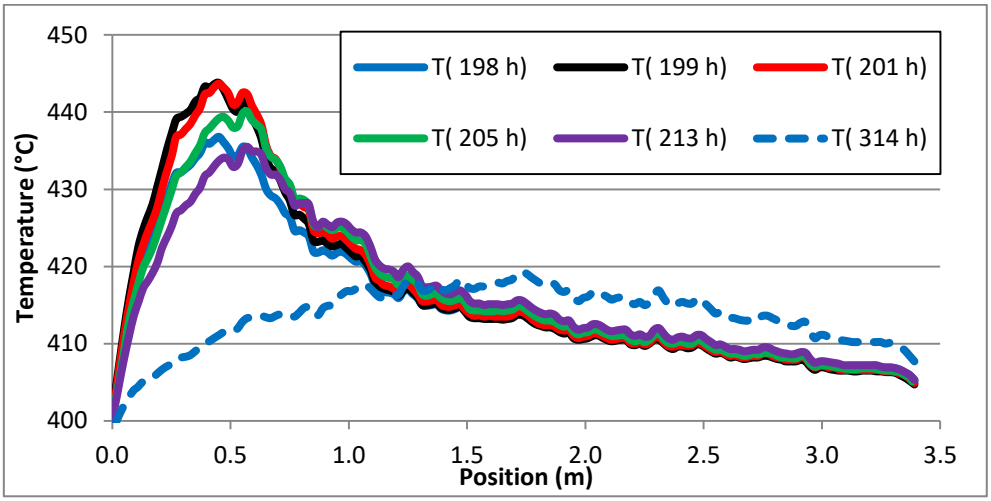

Fig. 37: Progression of the temperature profiles after interrupting the water feed from the initial 3 vol% at constant TMP concentration at 198 h TOS according to operating points 3-1 to 3-3 in Tab. 12.

Again, it was found that these changes were fully reversible. Fig. 38 shows an experiment during which the catalyst was first damped by continuously adding TMP but no water (T(624 h)). When the water feed was started, the initially flat temperature profile first decreases slightly, but then a hot spot starts to form very slowly in the inlet part of the catalyst bed.

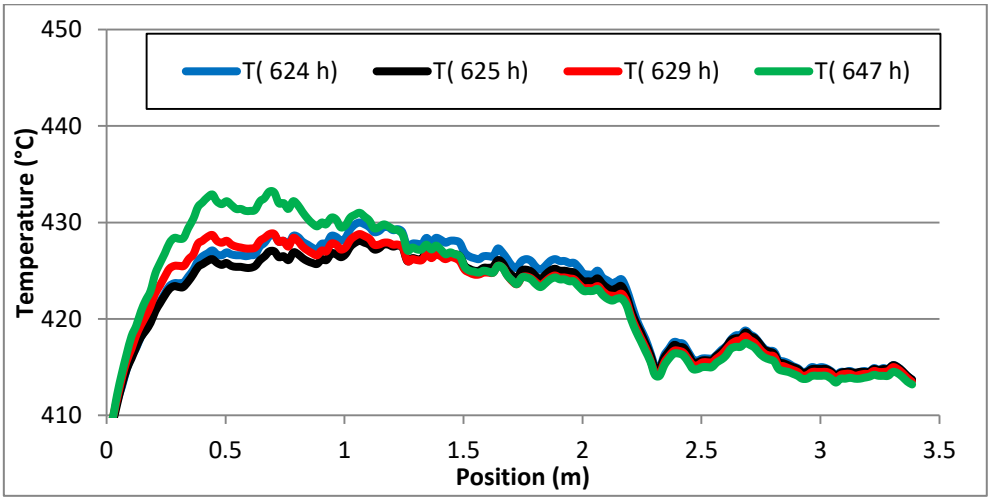

Fig. 38: Progression of the temperature profiles after increasing water feed at constant TMP addition at 624 h TOS according to operating points 4-1 to 4-3 in Tab. 12.

4.5 Discussion

The elaborated pilot reactor experiments illustrate some important aspects concerning the dynamic behavior of VPO catalysts in industrial scale fixed bed reactors for the production of maleic anhydride. Each experiment took several hundred hours during which the feed concentrations of water and TMP as phosphorus supply were varied under different operating conditions. The progressions of the hot spot temperatures after these variations during the entire experiment *PT3* is exemplarily shown in Fig. 39. In general, the assertions of the patent literature could be confirmed. Additionally, versatile interactions between water, TMP and the catalyst surface could be investigated separately. The importance for the industrial process is evidenced regarding the broad range of MA-yields, which were observed in the presented experiments (Fig. 40). Although *n*-butane concentration, inlet pressure, space velocity, and salt bath temperature were always kept at typical industrial values, Fig. 40 demonstrates that only slight variations of the concentrations of water and TMP in the feed may shift the MA yield significantly from its optimum.

The observations, which were made during the experiments, may be summarized as follows:

a) Initial start-up and equilibration: *n*-Butane conversion and hot spot temperature decline, while MA selectivity increases during the initial catalyst conditioning. Subsequently, catalyst reactivation appears in the bed region of higher temperatures and the hot spot temperature increases again. With time on stream, the catalyst activity hence passes through a wide minimum. The observed time periods of the formation and stability of this first steady state of lower catalyst activity became shorter with increasing bed temperatures.
b) Phosphorus promoter effect: The addition of TMP has a damping effect on a time scale of hours during which the conversion declines and MA selectivity increases. Simultaneously, the hot spot decreases and moves towards the center of the catalyst bed, becoming broader with time. The phosphorus induced changes in catalyst performance are noticeable even several days after switching operating conditions.
c) Steam moderator effect: The addition of water exerts very important impacts on the catalyst performance. Its intrinsic inhibition effect is seen on the time scale of minutes. Hence, higher water feed concentrations reduce the reaction rates, and thus hot spot temperature and conversion drop whereas the MA selectivity rises. However, when TMP is fed simultaneously with water, a rise of the water feed provokes an increase of the activity in the inlet part of the catalyst bed. This effect occurs on a time scale corresponding to that of the pure TMP impact and confirms the observations in the patent literature that water is able to distribute the phosphorous along the catalyst bed [12]. All effects related to the addition of TMP and water are reversible and the temperature profiles always present the highest sensitivity to the phosphorus dynamics.

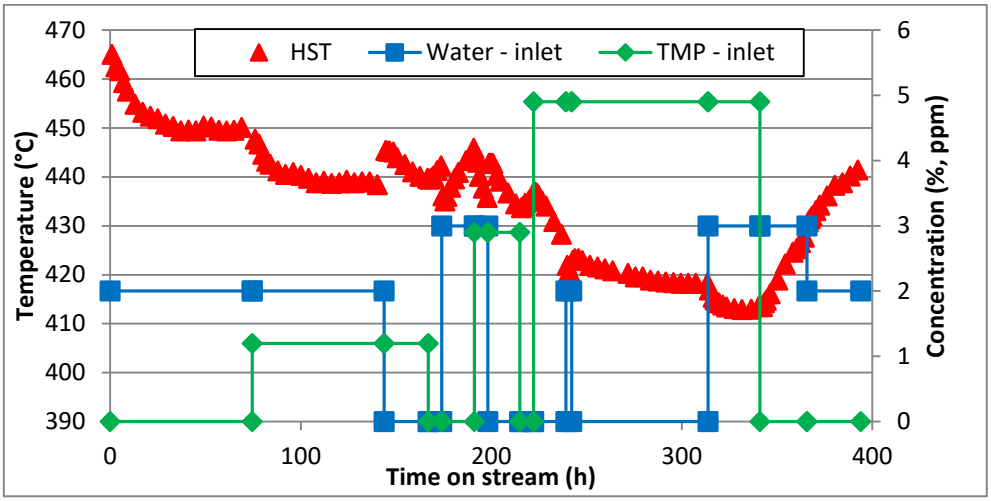

Fig. 39: Progression of the hot spot temperatures and inlet concentrations of TMP and water during *PT3*.

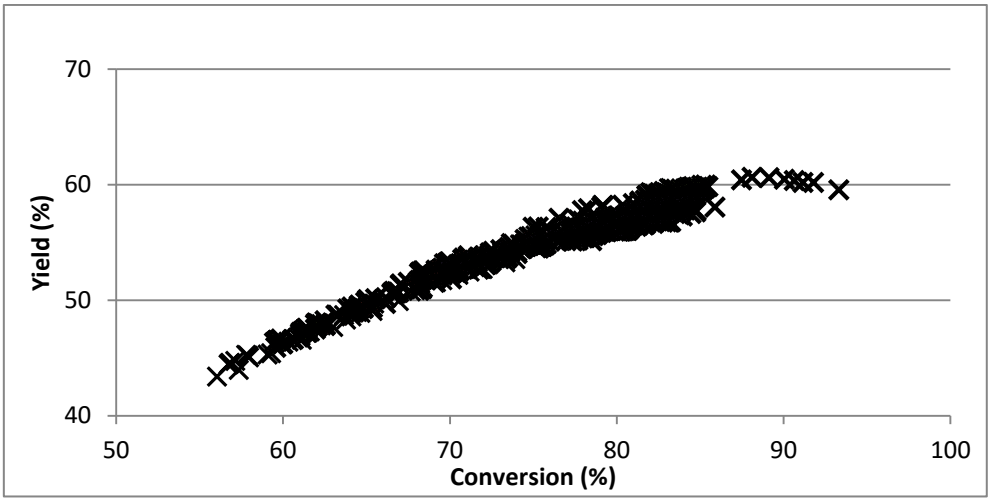

Fig. 40: Yield-conversion plot including all concentration measurements of all pilot tests.

In the literature, the changing catalytic performance of a freshly activated catalyst during the initial operation is mostly referred to as “conditioning” or “equilibration” [6–8,51]. A number of studies on this subject are reviewed in [6–8]. Coupled to the activation of the hemihydrate precursor, the conditioning stage is considered to be critical for the final performance of the catalyst. It is reported that the hemihydrate is transformed into V^{4+} and small amounts of V^{5+} phases during the activation step, while during the conditioning stage V^{5+} phases are reduced to V^{4+}, obtaining highly crystallized VPP with high BET surface areas [6–8,51,72]. Thereby, temperature and water, both, may essentially affect the structure and composition of the active catalyst surface [7,24,39–41,70]. However, these two coupled processes, i.e. activation and equilibration, were often not regarded or sufficiently controlled, yielding discrepancies between

different reported efforts on this topic [8]. The activation of the hemihydrate may be performed *ex-situ* or *in-situ*. *Ex-situ* activation implies a treatment in a non-reacting atmosphere, which is carried out prior to the conditioning in an *n*-butane containing atmosphere. On the other hand, *in-situ* activation combines both steps simultaneously. Hence, a lack of a common and systematic methodology is probably the major reason for discrepancies in the literature [8]. These differences relate to the conditioning time for which several hours up to 1000 h were reported, to the role of V^{5+}-phases, the crystallinity of VPP, as well as the generation of surface defects [6,8,51]. There are also contradicting views about the role of water. Patience *et al.* [73] found a deleterious effect, as the addition of water produced highly oxidized catalysts with low MA yields. In contrast, different authors reported higher MA selectivities and higher BET surface areas in the presence of water [7].

Recently, the initial loss of activity has been investigated by Wilkinson *et al.* [8] who observed the performance development of an *ex-situ* activated catalyst during the first 100 h of operation in a micro-reactor. As during the experiments described in the present paper, the authors observed a sharp decline in catalyst activity, during which the overall MA selectivity increased. In contrast, the deactivation rate of this initial process appeared to be independent of reactor temperature and took only a few hours. The reasons for this discrepancy may lie in the different reaction conditions applied by Wilkinson et al. [8], where the maximum temperature was below 410°C and water was not fed. Moreover, the catalyst synthesis and activation procedure applied in [8], which was found to have a significant effect on the catalyst performance [73], may differ in detail from that of the catalyst applied in the present work. Wilkinson *et al.* [8] additionally reported temporal variations of the CO_x formation rates along the catalyst bed during the initial operation. In the present work, such variations were not observed.

The activity and selectivity, initially changing during S/U until the first steady state was reached, were not in the focus of this study. An extraction and analysis of the catalyst after the equilibration period was not carried out. Hence, no conclusion about the underlying deactivating mechanism can be provided.

The presented experiments show how the hot spot temperatures start to rise again after the catalyst had reached the first steady state. Similar observations were reported by Buchanan and Sundaresan [32]. During studies of kinetics and redox properties of two VPO catalysts with P/V 1.0 and P/V 1.1 an irreversible loss of selectivity was observed during prolonged runs at 450°C with the P/V 1.0 sample. This is also in accordance with the presented experiments, during which the reactivation appeared much faster at temperatures above 440°C. Furthermore, it should be recalled that during the kinetic experiments in the bench scale reactor a reactivation was observed after prolonged runs at temperatures above 440°C.

In the patent literature [9,11], this observation is mostly described as a deactivation process or as a loss in selectivity and yield, although it basically refers to the same behavior. It is generally assumed that a loss of phosphorus is the cause of this behavior [3,12,32]. The analysis of some of the above mentioned samples that showed a reactivation after the prolonged runs at high temperatures in the laboratory reactor did indeed show reduced P/V ratios. The fact that

phosphorus can be released from the VPO surface to the gas phase has been proved in [40,65,68]. Cavani *et al.* [40] showed how *n*-butane conversion increased and MA selectivity declined after *in situ* removing phosphorus from the catalyst by treatment with water and ethanol. However, this was only observed at low temperature (380°C), while interestingly the phosphorus removal at high temperature (440°C) had no effect on the catalytic performance. The authors related this effect to the formation of different active surfaces as a function of reaction conditions. Accordingly, the composition of the active surface, which forms at high temperatures, is not affected by the phosphorus content.

The presented experiments in our study in contrast showed a significant acceleration of the changes in activity during long-term operations without phosphorus addition at high temperatures. Unfortunately, *in situ* characterization tools are not available at the pilot reactor being necessary to prove this loss of phosphorus leading to the shift in performance. Referring again to the works of Cavani *et al.* [39,40] according to which the active catalyst surface should be different along the catalyst bed as a function of temperature and fluid composition, also different reversible and irreversible activation and deactivation mechanisms may be responsible for the observed behavior.

Different relations between selectivity and the phosphorus content of the catalyst have also been deduced from DFT modeling of the active VPO surface [22,74]. Thompson *et al.* [74] suggested that vanadium is responsible for adsorption and activation of *n*-butane, while surface P-O oxygens may aid in electrostatic docking of *n*-butane at the surface and provide a source of selective oxygen species for the further transformation of activated *n*-butane to MA. Because of their nucleophilic character, the P-O oxygens are supposed to be more active in C-H than in C-C cleavage. Cheng and Goddard [22] concluded from their calculations that the O(1)=P of the metastable X1-$VOPO_4$ phase is able to carry out the *n*-butane activation so as its complete conversion to MA. Hence, a loss of phosphorus would mean reduced contents of selective P-O oxygens at the surface.

Independent of the previous discussion, the consequences for industrial operation become clearer with the examples described in the patents. For instance, Edwards *et al.* [11] reported that the coolant temperature decreased with operating time together with a reduced MA yield. In the light of the current study, this observation can be explained by the rising hot spot temperature during a long-term operation without phosphorus addition with simultaneous increasing conversion and decreasing selectivity. Depending on catalyst and operating conditions, the yield may hence proceed through a maximum, to later decrease again. Moreover, a declining MA selectivity with rising hot spot temperature implies a higher formation rate of carbon oxides, which in turn releases more heat, increasing the risk of reactor runaway. As specified in [11], the industrial reactor operator would thus have to reduce the coolant temperature, resulting in reduced MA yields. The addition of phosphorus on the other hand, permits reactor operation at higher coolant temperatures without any significant negative impact on selectivity.

An important result of the presented experiments however, is the necessity of an adequate phosphorus dosage, as already the addition of very small amounts of phosphorus significantly reduces the catalyst activity. The influence of the phosphorus content on the catalytic performance has been subject of investigations during several decades as resumed in [6,7,18]. It is generally agreed that well performing VPO catalysts exhibit a slightly higher P/V ratio than the stoichiometric ratio of one for VPP. On the other hand, excess phosphorus is assumed to prevent the bulk oxidation of VPP [6,7,52,53]. As various authors have related different V^{5+} species to the active catalyst surface [39,40,59,60], this may well explain the observations of the presented experiments. The addition of TMP to the reactor feed leads to higher phosphorus concentrations on the catalyst surface, which thus diminishes catalyst activity. The observed reversibility of this effect suggests that the introduced excess phosphorus is located on the surface, where its concentration is determined by the adsorption equilibrium with the gas phase. Although diffusion of phosphorus into the catalyst bulk and related effects on the intrinsic activity are expected to be present [39,68], such processes might occur on a much slower time scale and were thus not significant during the presented experiments of this work.

On the other hand, various authors who carried out *in situ* analyses of working VPO catalysts observed an enrichment of phosphorus in the surface region under reacting conditions, although without any external addition of phosphorus [24,40,41,65,70]. An important subject of the debate in this context is the theory that a highly dynamic surface forms on the pyrophosphate phase under reaction conditions, which is composed of various VPO phases [39,40,64] as a function of operating conditions.

Supporting the observations of the presented experiments, water, which is always present as a reaction product, is supposed to play a central role in the surface dynamics [39–41,64,65]. This may explain the variety of observed water induced effects on catalyst performance reported in the literature [24,28,45,70], so as the large number of different reported active sites/phases and their function in the conversion of *n*-butane towards selective and unselective reaction products [6,7,18]. An attempt to resume the complex situation is presented in Fig. 41 and described in the following section.

Crystalline vanadium pyrophosphate, which is always observed in active and selective catalysts, is considered to be the core of the active phase [6,18,40] and can be oxidized into a variety of orthophosphates, which partially may interconvert. So far, the structures of α_I-, α_{II}-, β-, γ-, δ-, ε-, ω-$VOPO_4$ and the X1-phase have been described in the literature [61,75–78]. Relations to the catalyst performance were reported for α-, β-, δ- and X1-$VOPO_4$ (⑥, ⑦, ⑤, ④ in Fig. 41) [22,39,40,59,61,67]. Frey *et al.* [59] suggest the adsorption of *n*-butane on δ-$VOPO_4$-like surface species (⑤ in Fig. 41), while Cheng and Goddard [22] showed by means of DFT modeling that the O(1)=P of the metastable X1-$VOPO_4$ phase (④ in Fig. 41) is able to activate the *n*-butane molecule, initializing the VPO chemistry. α-$VOPO_4$ was also supposed to contribute to the active surface [60], and it was reported to be very active but unselective [39,40]. Low catalyst performance was reported for β-$VOPO_4$ [61,67,78]. Nevertheless, α-, β-, δ- and X1-$VOPO_4$ were all observed on the catalyst surface under working conditions and might therefore contribute to

the formation of the different active surface sites. On the other hand, excess phosphorus prevents the oxidation of VPP to these V^{5+}-species [6,40,52,67].

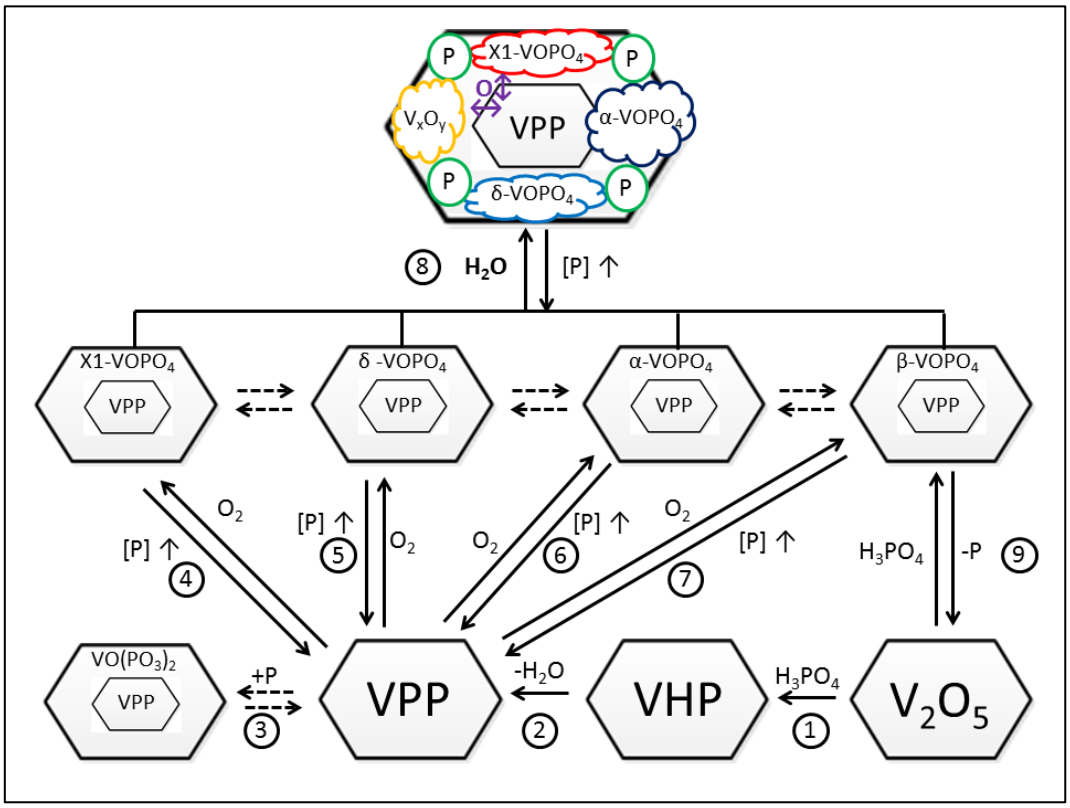

Fig. 41: Proposed scheme of the VPO chemistry derived according to the literature ([P]↑ and [P]↓ mean higher and lower phosphorus concentrations).

Although Cheng and Goddard [22] demonstrated low activation barriers for the complete olefinic route mechanism, this model may be questionable, as under standard reaction conditions, no gas phase intermediates were reported in the literature. It is therefore more likely that once the *n*-butane molecule is activated, the complete conversion to the final products occurs on the surface through strongly adsorbed intermediates. The nature of active oxygen is supposed to be lattice oxygen [22,48,79] which has to be provided locally to these intermediates. Its local concentration is thus function of the hydrocarbon conversion, the introduction of gas phase oxygen and the diffusion of oxygen between surface and bulk of the catalyst. Hence, the introduction of three oxygen atoms during the selective conversion of *n*-butane to MA requires a certain flexibility of lattice oxygen in the catalyst. According to Willinger *et al*. [78] and the model of Guliants *et al*. [22], the diffusion of oxygen between catalyst bulk and surface is facilitated in layered structures as contrasted to more stable, three-dimensional configurations. Also Bluhm *et al.* [64] emphasize the importance of a two-dimensional surface with increased flexibility of the reaction centers in their electronic structure. This hypothesis is

further supported by the findings of Guliants *et al.* [80] that better performances are achieved with VPP with well-ordered stacking of the (200) planes. Additionally, Okuhara and Misono [81] reported higher selectivity for plate-like VPP particles.

With respect to the different orthophosphates, such layered structures were reported for the X1-phase [22,61], and also for α-$VOPO_4$. The most stable orthophosphate is β-$VOPO_4$ (⑦ in Fig. 41) which has a three-dimensional structure [75] and shows low catalytic performance [61,67,78]. According to Willinger *et al.* [78], the conversion of α- to β-$VOPO_4$ is irreversible and its lower activity may be related to its higher stability. δ-$VOPO_4$ was related to a moderately active, but very selective catalyst [39,40]. Koyano *et al.* [61] supposed similar structures of X1- and δ-$VOPO_4$, but Girgsdies *et al.* [77] found by means of powder X-ray diffraction that the latter has a different, more three-dimensional structure. However, its strongly elongated V-O distances are supposed to facilitate its hydration to $VOPO_4 \cdot 2\ H_2O$, which itself has a structure similar to the layered α-$VOPO_4$ phase. This is in accordance with the concept of Bluhm *et al.* [64], in which water drives the system into a two-dimensional state.

Hence, such hydrolyzing step is also included in the proposed scheme of this work (⑧ in Fig. 41), leading to a highly dynamic surface. On this surface, all reported species, which were suggested to be active in the reaction mechanism, may be present in a two-dimensional surface state on top of crystalline VPP. While only one of these species might activate the *n*-butane molecule, the introduction of oxygen may be catalyzed by different species, which would lead to selectivity variations depending on the relative surface abundances of these species. The dynamic character of the surface is induced by water, which is always present under reaction conditions, and ensures the high dynamics of oxygen between surface species and catalyst bulk.

According to the higher mobility of oxygen, a layered surface structure might also facilitate the diffusion of phosphorus between bulk and surface, and finally the enrichment of the surface with phosphorus, as it was observed by Richter *et al.* [65] and Bluhm *et al.* [64]. Separated phosphate groups, which form after hydration, as postulated by [24,64,65], may affect the stability of the various phases present and thus, the composition of the surface. This scheme does also explain the relation between phosphorus content, activity and selectivity, according to the works of Cavani *et al.* [39,40], and finally, the enormous impact of the addition of only small amounts of TMP to the industrial reactor. On the other hand, too high phosphorus contents prevent the oxidation of the VPP bulk (④, ⑤, ⑥, ⑦ in Fig. 41) [6,40,52,60] and inhibit the formation of the active surface. If additionally water is not added to the system, the excess phosphorus cannot diffuse easily into the bulk of the catalyst. Under such conditions even vanadyl metaphosphate, $VO(PO_3)_2$ may be formed (③ in Fig. 41) on the surface, which was reported to have low activity [80] and low selectivity [82]. However, performance losses after extensive phosphorus addition, as observed by Cavani *et al.* [40], could also be related to the formation of polyphosphoric acids. Such were found by Castellino *et al.* [83] who exposed vanadium based SCR catalysts to flue gases containing phosphoric acid.

The phosphorus loss of the catalyst was often related to the formation of inactive V_2O_5 [24,64,68]. Xue and Schrader [24] even observed the direct reaction of orthophosphates to V_2O_5

(⑨ in Fig. 41; not necessarily β-$VOPO_4$). On the other hand, V_2O_5 and phosphates can react back to $VOPO_4$ phases [52,64], and the presence of reducing conditions may even facilitate the formation of the hemihydrate precursor (① in Fig. 41) and its dehydration to fresh VPP (② in Fig. 41) according to the synthesis of the industrial catalyst [6].

The proposed scheme may be a reasonable attempt to combine the contradictory literature on the nature of the active sites on VPO catalysts. The important role of water is emphasized as it induces the dynamic two-dimensional state of the catalyst surface, which facilitates the diffusion of oxygen and phosphorus between bulk and surface. In this scheme, the VPP bulk acts only as a precursor for active species and support on which various phases form during operation and which may have different functions in the reaction mechanism.

In the light of the experimental observations in this study, the diverse water effects may be resumed as follows. On a short term the adsorption of water on the catalyst surface inhibits the intrinsic reaction by site blocking effects in accordance with literature reports [41,45]. On the long term, the presence of water assures the working ability of the VPO surface by inducing the dynamic two-dimensional state. The interactions of steam with phosphorus seem to be various. A competitive adsorption of water and phosphorus, as well as the effect that the water induced surface dynamics may facilitate the phosphorus absorbing capacity of the catalyst, are both reasonable attempts to explain the experimental observations of this work. In this way, the addition of water to a catalyst, which is already saturated by phosphorus, reduces its surface concentration while the catalytic activity increases again. This corresponds to the statements in the patent literature in which water is assumed to play an important role for an adequate distribution of the phosphorus in the catalyst bed [10,11].

It is worth noting that the concept of a dynamic active catalyst surface, which forms only under reaction conditions, is not new in the literature. Mestl *et al.* [84] discovered similar transformations during the catalytic function of heteropoly acid catalysts for partial oxidations. These authors found that the Keggin anion structure of $H_4PVMo_{11}O_{40}$ disintegrates under reaction conditions, forming a variety of surface phases, among others also molybdenyl and vanadyl orthophosphates. Schlögl [46] constituted different requirements of the active sites for the dehydrogenation of propane and the selective oxidation to acrylic acid which occur both on the M1-phase $MoVNbTeO_x$ in a consecutive reaction network. The similarity of the chemistry to the VPO case is given as the first step in *n*-butane oxidation too is supposed to be the abstraction of hydrogen [6,18]. The author also suggests a strictly two-dimensional nature of the V_xO_y species on the M1 surface, which are active in the selective oxidation path.

The discussion about the composition of the VPP surface under reaction conditions and its influence on selectivity leads to another important subject, which is the number, and nature of active sites being involved in the *n*-butane conversion and their functions in the different reaction paths. While Bluhm *et al.* [64] did not study this aspect, there is a considerable number of works [6,7,28,39–41] which suggest that more than only one active site are present on the catalyst surface, and that they show different activities for the different reaction paths. This was previously discussed in section 2. Based on the present study, it is rather difficult to confirm or

rule out the presence of various active sites. The experimental observations are strongly influenced by the polytropic character of the applied industrial-scale pilot reactor, so as by diffusion effects in the catalyst particles.

5 Dynamic reactor modeling

A kinetic model was derived which describes the steady state reaction kinetics of the conversion of *n*-butane over equilibrated VPO catalysts (section 3). Despite the appearance of several non-ideal aspects related to the bench scale experiments, a kinetic model was obtained which satisfactorily describes the applied full body catalyst shapes. During the short term bench scale experiments no phosphorus was fed to the reactor and only minor changes in the catalyst activity were detected. However, the experiments which were carried out in the pilot reactor (section 1) revealed that the addition of only trace amounts of phosphorus to the reactor feed induces significant changes in catalyst performance as a function of time and operating conditions. In order to be able to describe an industrial fixed bed reactor, for which the commercial operation implies the addition of phosphorus to the reactor, it is necessary to include the phosphorus dynamics in the final reactor model. Hence, the next steps are:

- Development of a mathematical model for the pilot reactor
- Development of a mathematical model which describes the phosphorus dynamics
- Integration of the dynamic phosphorus model into the reactor model
- Parameter estimation through simulation of the previously performed pilot reactor experiments

The pilot reactor experiments further revealed that the phosphorus induced activity dynamics occur on a time scale of hours to days while on the other hand, the conversion of educts on the active sites of course occurs much faster. The different time scales of these processes offer the opportunity of strictly separating their mathematical descriptions. This means that only the time derivative of the rate determining modification of the active surface must be considered, while all other processes may be assumed to reach steady state. Thus, the final expressions for the reaction rates take the following form:

$$r_{i,j}(t) = r_{i,j}^{0} \cdot a_k(t) \qquad i = n\text{-Bu, MA}; \quad j = \text{MA, } CO_x; \quad k = 1\ldots n \qquad (5\text{-}1)$$

In this equation $a_k(t)$ is an activity factor which describes the changing catalyst activity induced by the phosphorus dynamics and $r_{i,j}^{0}$ is the intrinsic steady state reaction rate for reaction of *i* to *j* at a reference activity a_k^0. The index *k* accounts for the possible existence of various active sites. In the course of the present work, this reference steady state activity is thus, simply correlated to the constant activity which the catalyst exhibited during the kinetic experiments in the bench reactor. The advantage of this strategy is that the previously determined intrinsic kinetic

parameters can be fixed and only those parameters, which determine the dynamic changes of activity, must be determined by simulation of the pilot reactor experiments.

5.1 Reactor model

As discussed in section 2.5.3, the mass transport within the industrial catalyst bodies, has a significant influence on the apparent reaction rates. Therefore, a heterogeneous reactor model was applied for the simulation of the bench reactor which permits a separate description of solid and fluid phase and which accounts for intra-particle diffusion. As the experiments in the pilot reactor were carried out with the catalyst shapes *C5* and *C6*, which were also used for the kinetic experiments, the model for the pilot reactor is heterogeneous, too.

In contrast to the smaller bench reactor, the catalyst charges in the pilot reactor are not diluted and significant hot spots of up to 60 K were detected during the experiments. The fact that this temperature gradient is present along a radius of only about 15 mm (tube plus wall) underlines the significance of the radial heat transport. The resulting radial temperature profiles in the catalyst bed will cause pronounced differences in the reaction rates along the tube axis. In order to take into account such heat effects, the model for the pilot reactor has to be two-dimensional. This means that the material and energy balances are defined on a ring shaped volume element of the reactor tube and the integration succeeds in axial and radial directions.

The final balance equations for ring shaped catalyst pellets are shown below. For the radial heat transport, the α_w-model according to Nilles [56] was applied with some modifications as discussed below. Because the Bodenstein numbers were around 1500 during the experiments, the influence of axial dispersion was neglected [16].

- **Overall mass balance gas phase:**

$$\frac{\partial}{\partial z}\left(\rho_{fl} \cdot u_z\right) + \frac{1}{r}\frac{\partial}{\partial r}\left(r \cdot \rho_{fl} \cdot u_r\right) = 0 \tag{5-2}$$

- **Momentum balance:**

$$-\frac{\partial p}{\partial z} = C^{lam} \cdot \frac{(1-\varepsilon_B)^2}{{\varepsilon_B}^3} \cdot \frac{\eta_{fl} \cdot u_z}{d_p^2} + C^{turb} \cdot \frac{(1-\varepsilon_B)}{{\varepsilon_B}^3} \cdot \frac{\rho_{fl} \cdot {u_z}^2}{d_p} \tag{5-3}$$

- **Material balance fluid:**

$$-\varepsilon_B \cdot c_{fl}^f \cdot \frac{\partial x_i^f}{\partial t} = \frac{\partial \dot{N}_{i,z}^f}{\partial z} + \frac{1}{r}\frac{\partial}{\partial r}\left(r \cdot \dot{N}_{i,r}^f\right) - a_P \cdot \dot{N}_i^{Sf} \tag{5-4}$$

Radial material flux:

$$\dot{N}_{i,r}^{f} = -\varepsilon_B \cdot c_{fl}^{f} \cdot \mathcal{D}_{i,r}^{f} \cdot \frac{\partial x_i^f}{\partial r} + u_r \cdot c_{fl}^{f} \cdot x_i^f \tag{5-5}$$

Material transfer fluid-solid:

$$\dot{N}_i^{sf} = \beta_i \cdot c_{fl}^{f} \cdot \left[f^{osf} \cdot \left(x_i^{osf} - x_i^f \right) + \left(1 - f^{osf} \right) \cdot \left(x_i^{isf} - x_i^f \right) \right] \tag{5-6}$$

- **Material balance solid:**

$$\varepsilon_p \cdot c_{fl}^{s} \cdot \frac{\partial x_i^s}{\partial t} = -\frac{1}{r_p} \frac{\partial}{\partial r_p} \left(r_p \cdot \dot{N}_i^s \right) + \sum_j \nu_{i,j} \cdot r_j^0 \cdot a_k(t) \cdot \rho_P \tag{5-7}$$

Material flux by diffusion:

$$\dot{N}_i^s = -c_{fl}^{s} \cdot \mathcal{D}_i^{s,eff} \cdot \frac{\partial x_i^s}{\partial r_p} \tag{5-8}$$

- **Material balance solid surface (boundary conditions solid):**

$r_p = R_{P,outer}$:

$$\frac{\varepsilon_p}{S_v} \cdot c_{fl}^{osf} \cdot \frac{\partial x_i^{osf}}{\partial t} = c_{fl}^{s} \cdot \mathcal{D}_i^{s,eff} \cdot \frac{\partial x_i^{osf}}{\partial r_p} + \beta_i \cdot c_{fl}^{f} \cdot \left(x_i^{osf} - x_i^f \right) \tag{5-9}$$

$r_p = R_{P,inner}$:

$$\frac{\varepsilon_p}{S_v} \cdot c_{fl}^{isf} \cdot \frac{\partial x_i^{isf}}{\partial t} = c_{fl}^{s} \cdot \mathcal{D}_i^{s,eff} \cdot \frac{\partial x_i^{isf}}{\partial r_p} - \beta_i \cdot c_{fl}^{f} \cdot \left(x_i^{isf} - x_i^f \right) \tag{5-10}$$

- **Energy balance fluid:**

$$\frac{\partial H^f}{\partial t} = \frac{\partial \dot{H}_z^f}{\partial z} + \frac{1}{r} \frac{\partial}{\partial r} \left(r \cdot \dot{H}_r^f \right) + \frac{1}{r} \frac{\partial}{\partial r} \left(r \cdot \dot{Q}_r^f \right) - a_P \cdot \left(\dot{H}^{sf} + \dot{Q}^{sf} \right) \tag{5-11}$$

Radial heat flux in the fluid phase:

$$\dot{Q}_r^f = -\lambda_r^f \frac{\partial T^f}{\partial r} \tag{5-12}$$

Heat flux fluid-solid:

$$\dot{Q}^{sf} = \alpha_P \cdot \left(T^{sf} - T^f\right) \tag{5-13}$$

$$T^{sf} = T^{osf} = T^{isf} \tag{5-14}$$

- **Energy balance catalyst pellet:**

$$-\rho_P \cdot c_{p,P} \cdot \frac{\partial T^s}{\partial t} = \frac{1}{r_p}\frac{\partial}{\partial r_p}\left[r_p \cdot \left(\dot{Q}^s + \dot{H}^s\right)\right] + \sum_i \sum_j \nu_{i,j} \cdot r_j^0 \cdot a_k(t) \cdot \rho_P \cdot \Delta_F H_i^* \tag{5-15}$$

Heat flux in the solid phase:

$$\dot{Q}^s = -\lambda^s \cdot \frac{\partial T^s}{\partial r_p} \tag{5-16}$$

- **Energy balance solid surface (boundary conditions solid):**

$$a_P \cdot \dot{Q}^s - a_P \cdot \dot{Q}^{sf} - \frac{1}{r}\frac{\partial}{\partial r}\left(r \cdot \dot{Q}_r^{ss}\right) = \frac{\rho_P \cdot c_{p,P}}{S_v} \cdot \frac{\partial T^{sf}}{\partial t} \tag{5-17}$$

Radial heat flux between solid particles:

$$\dot{Q}_r^{ss} = -\lambda_r^{ss} \cdot \frac{\partial T^{sf}}{\partial r} \tag{5-18}$$

- **Energy balance reactor wall:**

$$\rho_W \cdot c_{p,W} \cdot \frac{\partial T^w}{\partial t} = -\frac{1}{r_w}\frac{\partial}{\partial r_w}\left(r_w \cdot \dot{Q}_r^w\right) - \frac{\partial \dot{Q}_z^w}{\partial z} \tag{5-19}$$

Heat fluxes in axial and radial direction:

$$\dot{Q}_j^w = -\lambda^w \cdot \frac{\partial T^w}{\partial j} \qquad \text{for } j = z, r \tag{5-20}$$

- **Boundary conditions reactor tube:**

Reactor inlet ($z = 0$):

$$\dot{N}_i^f(r)|_{z=0} = \dot{N}_{i0}^f;\ T^f(r)|_{z=0} = T^s(r)|_{z=0} = T^w(r_w)|_{z=0} = T^{SB} \tag{5-21}$$

$$\dot{N}_{i,r}^f(r)|_{z=0} = u_r(r)|_{z=0} = 0 \tag{5-22}$$

Reactor center ($r = R_i$):

$$\dot{N}_{i,r}^{f}(z)|_{r=R_i} = u_r(z)|_{r=R_i} = 0 \tag{5-23}$$

$$\frac{\partial \dot{N}_i^f(z)}{\partial r}|_{r=R_i} = \frac{\partial T^f(z)}{\partial r}|_{r=R_i} = \frac{\partial T^{sf}(z)}{\partial r}|_{r=R_i} = \frac{\partial u_z(z)}{\partial r}|_{r=R_i} = 0 \tag{5-24}$$

Inner reactor wall ($r = r_w = R$)

$$\dot{N}_{i,r}^{f}(z)|_{r=R} = u_r(z)|_{r=R} = 0 \tag{5-25}$$

$$\dot{Q}_r^f(z)|_{r=R} = \dot{Q}_r^w|_{r_w=R} = \alpha_W \cdot \left(T^f(z)|_{r=R} - T^w(z)|_{r_w=R}\right) \tag{5-26}$$

Outer reactor wall ($r_w = R_w$)

$$\dot{Q}_r^w|_{r_w=R_w} = \alpha^{SB} \cdot \left(T^w(z)|_{r_w=R_w} - T^{SB}\right) \tag{5-27}$$

Diffusion coefficients, as well as fluid-solid heat, and mass transfer coefficients were calculated according to the same correlations, which were applied in the bench reactor model (section 3.1). The most widely applied correlation for the pressure drop is that derived by Ergun [85], whereas the constants in equation (5-3) are C^{lam} = 150 and C^{turb} = 1.75 (see also equation (3-3) of the bench scale reactor model in chapter 3.1). However, the Ergun expression was originally developed for powders and spherical particles in tubes with high d_T/d_P-ratios. For different cases, a variety of correction terms have been proposed. Eisfeld and Schnitzlein [86] compared 24 published pressure drop correlations by evaluation of more than 2300 experimental data points. The best agreement between experiment and prediction was achieved with the correction term of Reichelt, which includes an influence on the d_T/d_P-ratio (5-28)-(5-31). The constants Ω_1, ω_1 and ω_2 were determined for different particle shapes. In case of the bench reactor (section 3.1) such correction was not necessary because of the dilution of the catalyst shapes with smaller inert particles.

$$C^{lam} = \Omega_1 \cdot A_w^2 \tag{5-28}$$

$$C^{turb} = \frac{A_w}{B_w} \tag{5-29}$$

$$A_w = \left(1 + \frac{2}{3 \cdot \frac{d_T}{d_P} \cdot (1 - \varepsilon_B)}\right) \tag{5-30}$$

$$B_w = \left[\omega_1 \left(\frac{d_P}{d_T}\right)^2 + \omega_2\right]^2 \tag{5-31}$$

The description of the heat transfer in the catalyst bed in case of two-dimensional, heterogeneous reactor models is another, more complex issue. As both, solid and fluid phase, contribute to the radial heat transport, the heat balance of each phase (equations (5-11) and (5-17)) requires separate radial heat transfer parameters. However, common literature models as those of Froment [55] and Zehner, Bauer and Schlünder [56] were developed and validated only for pseudo-homogeneous cases, which do not differentiate between solid and fluid phase. Instead, they make use of an overall effective heat conductivity, which is expressed by the general equation (5-32). The static term, $\lambda_{r,0}$, combines radiative and conductive transport mechanisms of both phases in the absence of fluid flow, while the dynamic term, $\lambda_{r,1}$, accounts for the convective contribution of the fluid flow.

$$\lambda_r^{eff} = \lambda_{r,0} + \lambda_{r,1} \tag{5-32}$$

A further distinction, which is made in two-dimensional models, is the description of the radial flow pattern and the temperature distribution at the wall. The α_w-model assumes plug flow and a characteristic temperature jump at the wall is described by a wall heat transfer coefficient (α_w) and a third kind boundary condition [56]. Alternatively, the $\lambda_r(r)$-model accounts for a radial flow distribution, which is caused by the radial profile of the bed porosity. At the wall, a first kind boundary condition states equality of fluid and wall temperature.

There is a longstanding debate about which of these models is more adequate. Proponents of the $\lambda_r(r)$-model point out the importance of the radial distribution of flow velocity and bed porosity, especially in case of low tube-to-particle diameter ratios [87,88]. These profiles are typically characterized by a significant slope of both parameters in the vicinity of the wall [56,89]. Porosity profiles must be determined experimentally or may be estimated by literature correlations which exist for a broad range of tube-to-particle diameter ratios and different spherical and cylindrical particle shapes [56,88,89]. The same accounts for the effective viscosity parameter, which is necessary for the description of the flow pattern by means of the extended Brinkmann equation. With the plug flow assumption, the α_w-model works without such parameters, but it implies an additional heat transfer coefficient at the wall (α_w). Proponents of this model insist on the experimental evidence of an existing temperature jump at the wall, which is also detectable in packed tubes without fluid flow [90].

In the presented experiments in the pilot reactor, the very low tube-to-particle diameter ratio ($D/d < 3$) caused significant wall effects (Fig. 42) and even minor filling voids. The filling was additionally influenced by the presence of the thermocouple well in the tube center, which may be the reason why several tested literature models failed in predicting reasonable porosity and velocity profiles in the present case. Therefore, the choice finally fell upon the α_w-model with the correlations according to Nilles (5-33)-(5-34) [56]. The range of validity with respect to the tube-to-particle diameter ratio is specified to 1.2 to 51. Although Bauer and Adler [90]

developed different correlations for spherical and ring shaped particles, the values for the bed porosity in the presented experiments are below the specified range of validity.

Fig. 42: Filling trial with catalyst C1 in a Plexiglas tube (21 mm inner diameter).

$$Nu^w = \left(1.3 + \frac{5}{d_T/d_P}\right) \cdot \frac{\lambda_{r,0}}{\lambda f} + 0.19 \cdot Re_0^{0.75} \cdot Pr^{1/3} \quad (5\text{-}33)$$

$$Nu^w = \frac{\alpha_w \cdot d_P}{\lambda f} \quad (5\text{-}34)$$

Another issue relates to the choice of the calculation method for the radial heat conductivity values for fluid and solid phase. Comparing to the application of two-dimensional, pseudo-homogeneous reactor models the number of works, in which heterogeneous models were used, is rather small. Hofmann [91] stated that in general the heat transfer between two adjacent particles is negligible. Accordingly, in most one-dimensional, heterogeneous models the heat exchange with the wall is conducted by the fluid phase while the solid interacts with the fluid only [16,55]. This method was also applied for the bench reactor model in the present work (section 3.1). Wijngaarden and Westerterp [92] followed the same principle for a two-dimensional, heterogeneous model which was used to describe a variety of dynamic experiments in a system without chemical reaction during which radial temperature profiles were measured. According to the authors, the estimated values of the heat transfer coefficients were in good agreement with the literature.

Papageorgiou and Froment [88] used a two-dimensional, heterogeneous model for the simulation of the highly exothermic synthesis of phthalic anhydride in a fixed bed reactor. For the modeling of the radial heat transport by means of the $\lambda_r(r)$-model, the authors assigned the respective static contributions of the effective radial heat conductivity to each phase, while the dynamic contribution was assigned to the fluid only. Testing different literature correlations for the static terms, the authors found a high sensitivity of the simulation results to the radial

conductivity parameters. Elsewhere [55], Froment points out that the simulated temperature profiles are too high if the whole conductivity term is assigned to the fluid phase only.

Marx [93] recently applied a two-dimensional, heterogeneous model for the description of an industrial scale pilot reactor in which the selective oxidation of *o*-xylene to phthalic anhydride was investigated. The reactor configuration was similar to that of the present work. The author applied the α_w-model and assigned the entire radial heat transfer to the solid phase. The radial heat conductivity and heat transfer coefficient at the wall were calculated according to the correlations of Zehner, Bauer, Schlünder and Nilles [56,94]. During kinetic parameter estimation however, the radial heat conductivity had to be multiplied by a factor of 1.8 in order to reproduce the measured axial temperature profiles.

Another issue related to this discussion is the fact that the literature models for the description of the radial heat transfer in fixed beds were derived or validated from data obtained from experiments without chemical reaction. In the presence of strongly exothermal reactions however, heat and mass transfer are coupled. Hofmann [91] reported significant differences in the heat transfer parameters when they were fitted together with kinetic parameters. Wijngaarden and Westerterp [95] explained such deviations by the presence of more pronounced temperature gradients between solid and fluid in experiments with chemical reaction. However, these gradients are not taken into account in pseudo-homogeneous models, which are generally the base for the common heat transfer calculation methods. Hence, an optimization of the literature values according to Marx [93] may be justified. On the other hand, Daszkowski and Eigenberger [96] found for the α_w-model that reaction and heat transfer can only be modeled with independently determined parameters if the radial variation of the axial mass flow velocity is properly considered.

With respect to the assignment of the radial heat conductivity of the catalyst bed with fluid flow, own simulations revealed that, if the complete radial heat transfer is assigned to the solid phase, the simulated temperature of the fluid becomes higher than that of the solid. This happens just after reaching the maximum hot spot temperature. In case of strongly exothermal reactions as is the *n*-butane oxidation however, this does not appear reasonable. On the other hand, assigning the heat transfer to the fluid phase only can lead to excessive temperature gradients between fluid and solid [55].

Hence, in the present work, a strategy according to that of Papageorgiou and Froment [88] was applied, but with the α_w-model. Static contributions of the solid and the fluid phase to the radial bed conductivity were calculated according to the correlations of Zehner, Bauer, Schlünder [94] for a packed bed without fluid flow. This was done by splitting the equation for the overall radial conductivity of the packed bed without fluid flow, $\lambda_{r,0}$, which is related to a pseudo-homogeneous reactor model, in two respective terms (5-35). The fluid contribution (5-36) increases with increasing gas volume ($\left(1-\sqrt{1-\varepsilon_B}\right)\cdot\varepsilon_B$) and the solid contribution (5-37) increases with increasing solid volume ($\sqrt{1-\varepsilon_B}$). It is important to note this is an approximation since according to the unit cell model of Zehner, Bauer and Schlünder the latter term refers to

the heat flux from one spherical particle to another through a circular area that is partially composed of solid and fluid. This approximation has not been tested experimentally. The mean bed void fraction (ε_B) was obtained experimentally from the average filling density and the particle density.

$$\frac{\lambda_{r,0}}{\lambda_{fl}} = \frac{\lambda_{r,0}^{f}}{\lambda_{fl}} + \frac{\lambda_{r,0}^{ss}}{\lambda_{fl}} \tag{5-35}$$

$$\frac{\lambda_{r,0}^{f}}{\lambda_{fl}} = \left(1 - \sqrt{1-\varepsilon_B}\right) \cdot \varepsilon_B \cdot \left[(\varepsilon_B - 1 + \kappa_G^{-1})^{-1} + \kappa_{rad}\right] \tag{5-36}$$

$$\frac{\lambda_{r,0}^{ss}}{\lambda_{fl}} = \sqrt{1-\varepsilon_B} \cdot \left[\varphi \cdot \kappa_p + (1-\varphi) \cdot \kappa_c\right] \tag{5-37}$$

The obtained value for the static contribution of the solid, $\lambda_{r,0}^{ss}$, can be directly used in equation (5-18), while the dynamic contribution was added according to equation (5-38) for the total contribution of the fluid, λ_r^f in equation (5-12). The influence of the tube-to-particle diameter ratio is included in the parameter K_r (see annex A.3).

$$\frac{\lambda_r^f}{\lambda_{fl}} = \frac{\lambda_{r,0}^{f}}{\lambda_{fl}} + \frac{Pe_0}{K_r} \tag{5-38}$$

5.2 Activity model

Revising the scientific literature, only one theoretical study has been found, which attempts to describe the phosphorus dynamics of VPO catalysts for the selective oxidation of *n*-butane. Diedenhoven *et al.* [97] proposed a linear relation between reaction rates and phosphorous coverage on the catalyst surface which was determined by the adsorption kinetics. Their model was able to describe dynamic, phosphorus induced changes of the hot spot temperature while, however, form and location of the hotspot were not affected. An influence of water on the dynamics was not included. Hence, such simple approach is not sufficient for the description of the experiments of the present work, during which significant shifts of the temperature profile as well as significant interactions between water and phosphorus were observed.

The phenomena of shifting temperature profiles in industrial scale fixed bed reactors was more thoroughly investigated for a similar partial oxidation reaction which is the production of phthalic anhydride from *o*-xylene over V_2O_5/TiO_2 catalysts [93,98–100]. Among these works, Cheng *et al.* [99] presented a dynamic approach which included deactivation by coke formation on the catalyst surface as a function of the *o*-xylene concentration, so as the reactivation by gas

phase oxygen. The authors could well describe a series of dynamic experiments during which the hot spot moved inside the catalyst bed and the temperature profile showed an inflection point in the inlet section.

Based on the experimental observations of the present work and the conclusions in section 4.5, the following requirements for the dynamic activity model may be stated:

a) Active surface sites dynamically appearing and disappearing on the catalyst surface as function of reaction conditions.
b) The formation of active sites being hindered by excess phosphorus (= damping P effect)
c) The presence of water leading to catalyst activation through an enhancing effect on the P dynamics (this effect must not be mixed up with the intrinsic effect of water on the n-butane oxidation).
d) The surface concentration of phosphorus being determined by its adsorption equilibrium, which is altered by the presence of water.
e) The phosphorus induced processes being rate determining for the surface dynamics.

Points a) and b) are direct conclusions of the discussions in section 4.5. The formation of active sites (S_k^{VPO}) from non-active sites on the VPO surface (S_{k0}^{VPO}) can thus be expressed in form of a chemical reaction (5-i). In the light of the discussions in chapter 4.5, the water induced formation of an active site would thereby correspond to the water promoted stabilization of a two-dimensional state of the active surface, which is necessary in order to ensure the provision of bulk oxygen for the reaction. Accordingly, the S_k^{VPO}-formation reaction requires adsorbed water ($S_{H_2O}^{ads}$), whereas the presence of excess surface phosphorus (S_P^{ads}) favors the reverse path, i.e. the destruction of S_k^{VPO}. Both surface species, water and P, are not consumed in this reaction, and their presence is supposed to only affect the presence of different surrounding VPO surface species. The index *k* implies that more than only one active site might be involved as it was also worked out in chapters 3.4 and 4.5.

$$S_{k0}^{VPO} \underset{S_P^{ads}}{\overset{S_{H_2O}^{ads}}{\rightleftharpoons}} S_k^{VPO} \qquad (5\text{-i})$$

The adsorption of phosphorus on the catalyst surface is considered to be essential due to the following reflections. It is reasonable that a phosphorus induced shift of the temperature hot spot towards the center of the catalyst bed is consequence of high catalyst deactivation in the inlet zone. Therefore, the deactivating component phosphorus should present a concentration profile on the catalyst surface varying along the catalyst bed. The formation of such concentration profile is driven by the kinetics of adsorption and desorption of phosphorus on the catalyst surface. The influence of water on the phosphorus distribution can be expressed by

means of a competitive adsorption of phosphorus and water on free surface sites (S_0^{ads}) according to reaction (5-ii) and (5-iii).

$$P^* + S_0^{ads} \rightleftharpoons S_P^{ads} \quad \text{(5-ii)}$$

$$H_2O + S_0^{ads} \rightleftharpoons S_{H_2O}^{ads} \quad \text{(5-iii)}$$

The stability of trimethyl phosphate under reaction conditions is questionable. Phosphoric acid forms polyacids and phosphorus oxides at elevated temperatures [83,101]. Hence, the exact nature of the phosphorus species, which interact between gas phase and catalyst surface, is not known. For the model of the present work, a hypothetical species P* is therefore considered, which contains one phosphorus atom, similar to TMP.

It is worth noting that this model is a very simplified resume of the previously derived VPO scheme (Fig. 41 in section 4.5) since the surface species are not consumed during reaction (5-i). This means that no bulk diffusion of phosphorus is included and therefore, the model does not account for any storage of adsorbed phosphorus in the catalyst or for the removal of phosphorus from the catalyst bulk. All processes, which affect the activity, are occurring fully reversibly on the catalyst surface. For the time being, this model is thus only valid if no significant irreversible deactivation was observed.

A more general justification for the model assumptions may be as follows. Relating the reactivation after startup equilibration exclusively to a loss of phosphorus, it can be assumed for the experiments during which a significant reactivation did not appear, that the catalyst was still saturated with phosphorus. In other words, the phosphorus diffusion from the catalyst bulk to the surface was still not significant. The timely introduction of phosphorus to the reactor feed after equilibration further inhibits the formation of more pronounced concentration gradients in the catalyst bulk which would lead to a phosphorus loss and thus, to a change of the intrinsic catalyst activity.

Additionally, it must be taken into account that the pilot test runs in the present work took only up to two months each. As compared to typical commercial catalyst lifetimes of around six years, the interval of the presented experiments is still related to start of run conditions. Since the diffusion of phosphorus in the catalyst bulk is supposed to be again much slower than the adsorption dynamics, related long term effects like the formation of $VO(PO_3)_2$ or V_2O_5 (Fig. 41 in section 4.5), and probably occurs to a significant extent only on a longer time scale. Hence, such effects should not play any role during the experiments of the present work. Therefore, care should be taken when extending the proposed model to longer operation times.

In order to find mathematical expressions for the rates of reactions (5-i)-(5-iii) some additional assumptions are required. As pointed out in section 4.5, the active sites are supposed to be rather large structures, presumably being composed of various molecular surface species, as 8

hydrogens have to be removed and 3 oxygens need to be incorporated. Assuming that the actual adsorption sites for phosphorus and water are much smaller than the catalytically active sites, they can be balanced separately, so that S_0^{ads} and S_{k0}^{VPO} are not identical. A similar assumption is made with respect to the different active sites. Expressing the concentrations of active sites and adsorbed species by means of activity factor a_k and surface coverage, θ_i ($\theta_{Ph} + \theta_{H_2O} + \theta_0 = 1$), and assuming that the adsorption of water is much faster than that of phosphorus, the following model equations can be formulated.

$$\frac{\partial \theta_{Ph}}{\partial t} = k_{Ph}^{ads} \cdot p_{Ph} \cdot \frac{(1-\theta_{Ph})}{\left(1+K_{H_2O}^{ads} \cdot p_{H_2O}\right)} - k_{Ph}^{des} \cdot \theta_{Ph} \tag{5-39}$$

$$\frac{\partial a_k}{\partial t} = k_k^{act} \cdot \theta_{H_2O}^{\xi_{1,k}} \cdot (1-a_k)^{\xi_{2,k}} - k_k^{deact} \cdot \theta_{Ph}^{\xi_{3,k}} \cdot a_k^{\xi_{4,k}} \qquad k = 1, 2, \ldots N \tag{5-40}$$

A further simplification of the model implies the assumption that the adsorption of phosphorus is the rate limiting step of both reactions. In this case, the time derivative of the activity factor may be set to zero, leading to the following steady state expression (5-41).

$$a_k = \frac{K_k^{act} \cdot \theta_{H_2O}^{\xi_{1,k}}}{K_k^{act} \cdot \theta_{H_2O}^{\xi_{1,k}} + \theta_{Ph}^{\xi_{3,k}}} \qquad k = 1, 2, \ldots N \tag{5-41}$$

Note that both, the dynamic and the steady state approach combined with the dynamic expression for the surface coverage, as well as with the intrinsic kinetics (equations (3-36)-(3-37) in section 3.2) are able to describe the observed influence of water. High water concentrations in the gas phase favor the adsorption on the catalyst surface, which enhances the activating reaction (first term in equation (5-40)). On the other hand, it also inhibits the adsorption of phosphorus (first term in equation (5-39)), reducing its surface coverage which finally decelerates the deactivating reaction (second term in equation (5-40)).

The finding of initial conditions for equations (5-39) and (5-40) is strongly related to the definition of the reference activity, a_k^0. As the intrinsic kinetic parameters were determined after the equilibration periods during the bench reactor experiments, a_k^0 should be unity after the respective equilibration periods during the pilot reactor experiments. Therefore, only those pilot tests are considered during which no significant change of the intrinsic activity was observed after the equilibration period. Hence, the initial condition for the feed-related, additional phosphorus surface coverage is zero (5-42). Again, it is important to note that this initial phosphorus coverage relates to the surface phosphorus, which is in excess as compared to the fresh, virgin catalyst. The catalytically active surface species of the fresh vanadyl pyrophosphate catalyst of course do contain phosphorus, which however does not contribute to the exchange between catalyst and gas phase in the presented model. Hence, setting the time derivative of

the activity to zero, the initial catalyst activity is constant and unity during the steady state experiments, during which phosphorus was not yet added. As the observed initial deactivation during the equilibration period is excluded from the modeling, it is thus appropriate to start the simulations from the moment in which the first observed steady state was reached. The initial conditions for equations (5-39) and (5-40) are thus equations (5-42) and (5-43). The initial activity resulting from these equations is unity.

$$\theta_{Ph}(t=0) = 0 \tag{5-42}$$

$$\frac{\partial a_k(t=0)}{\partial t} = 0 \tag{5-43}$$

Another assumption had to be made with respect to the distribution of phosphorus within the catalyst pellet. Not knowing the exact nature of the acting phosphorus species, uncertainty prevails as to the transport mechanism in the catalyst. Diffusion through gas phase, solid surface and/or solid bulk is conceivable. Reminding the theory of a highly dynamic surface on which various VPO phases are in equilibrium (section 4.5), especially the surface and bulk diffusion would be enhanced by phase transformations. The influence of pore diffusion on activity and selectivity of the catalyst is visible, reaching an effectiveness factor for the butane conversion of about 50% in the hot spot region. Since the effects of phosphorus addition or withdrawal occur on a time scale of minutes to hours, it is not expected that pore diffusion with time constants of the order of seconds can influence these rather slow effects. For simplification is thus assumed that the concentration of the hypothetical phosphorus species in the catalyst equals the bulk concentration in the gas phase. Mathematically, this corresponds to the assumption that the efficiency factor for the phosphorus adsorption is always one for all catalysts and all process conditions. This assumption entails the advantage that no diffusion coefficient is required for the phosphorus species, which would be another subject to uncertainty. Accordingly, our model is rather likely not sufficient for describing the phosphorus dynamics in cases of strong diffusional limitations.

As the phosphorus concentration takes very small values in the range of ppm, the model stability was enhanced by logarithmizing the phosphorus balance leading to equation (5-44). The factor 1/0.4343 surges from the logarithmic base transformation (e→10).

$$-\frac{\varepsilon_{bed}\cdot c_{fl}^{f}}{0.4343}\cdot\frac{\partial log x_{Ph*}^{f}}{\partial t} = \frac{\dot{N}_z}{0.4343}\frac{\partial log x_P^f}{\partial z} - \frac{1}{0.4343}\frac{\varepsilon_{bed}\cdot c_{fl}\cdot D_{P,r}^{f}}{r}\frac{\partial}{\partial r}\left(r\frac{\partial log x_{Ph}^{f}}{\partial r}\right) - \frac{\sum_j \nu_{P,j}\cdot r_{P,j}\cdot\rho_P\cdot(1-\varepsilon_{bed})}{10^{log x_{Ph}^{f}}} \tag{5-44}$$

5.3 Parameter estimations

In the first step, the initial steady state experiments, during which phosphorus was still not added, were used for optimizing the derived reactor model in order to be able to correctly reproduce the measured concentrations and temperature profiles. This implies the optimization of the calculated heat transfer and pressure drop parameters, as well as of the kinetic model. At continuation, the optimized reactor model is used for simulating the dynamic experiments and for estimating the parameters of the above described activity model. Before presenting the parameter estimation results, the following paragraphs explain the applied methods of model and data preparation.

The concentrations of *n*-Butane, CO and CO_2 that were measured by means of an IR analyzer were directly used for the simulations, analogously to the procedure applied during the kinetic parameter estimation with the laboratory reactor experiments (section 3.3). For the preparation of the temperature measurements, the measurement positions in the catalyst bed had to be assigned to the axial grid points in gPROMS. For the two-dimensional heterogeneous pilot reactor model 58 grid points in axial direction and 4 in radial direction were used, as well as 6 grid points within the catalyst pellets. The number of axial points, which compose one measured temperature profile, however, was around 170. Hence, only those 58 axial measurement points were selected, the position of which corresponded to the position of the axial model grid points. The deviation between these positions was constantly below 5 mm, which should produce only minor errors. As the most significant changes in the temperature profiles occurred in the first part of the reactor, more data points along the first two meters of the catalyst bed were used. The final assignment of the temperature measurements is illustrated in Fig. 43 for one pronounced hot spot and one rather flat temperature profile. The lines represent the entire measurement and the markers are the respective temperature points used for parameter estimation in gPROMS.

The filling trial (Fig. 42) illustrates that the axial well, which contains the thermocouple, has contact with catalyst particles and reacting gas. Hence, the question arises if a measured temperature value corresponds to the solid or the fluid phase. An additional error is produced by the heat conduction within the thermocouple well. According to the jagged form of the temperature profiles (Fig. 43), the attribution of the measured values to either gas or solid phase is probably randomly distributed. For the simulations, the measured temperatures were hence assigned to the average of fluid and solid temperatures. The variance was thereby set to 5 K. It is worth noting that this is still a rather optimistic value, taking into account that according to the applied solid-fluid heat transfer model, the calculated temperature gradients are up to 10 K, and the thermocouple itself has an error of ± 2 K.

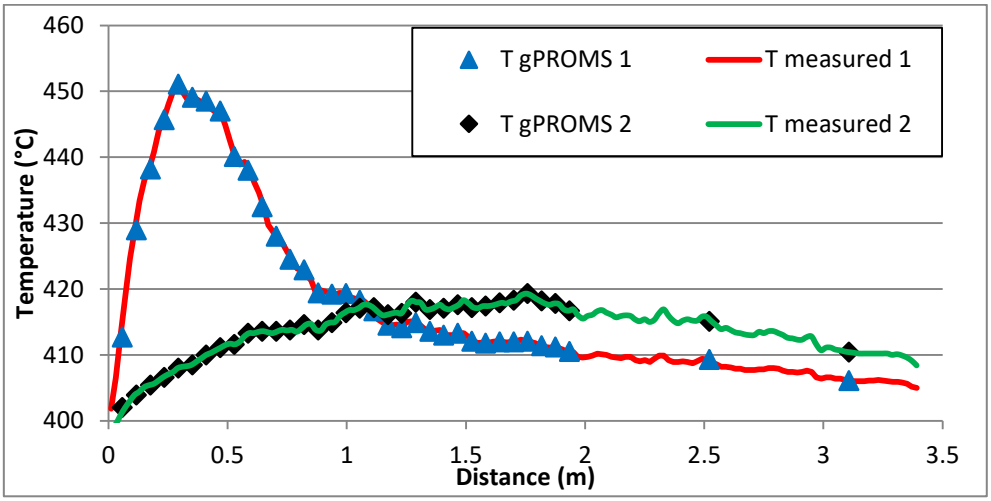

Fig. 43: Two measured temperature profiles and the corresponding data points which were used in gPROMS.

The experiments in the pilot reactor revealed that the changes in catalyst performance, which were induced by the phosphorus dynamics, became apparent on a time scale of hours. Hence, it is reasonable to establish hours as time unit for the integration of the balance equations. As the chemical reaction rates on the other hand have a much smaller time constant, the time derivatives of the fluid and solid concentrations of all compounds with exception of phosphorus were neglected. In case of the heat balances, only the time derivative of the solid temperature was included because of the much higher specific heat capacity of the solid as compared to the gas.

In order to reproduce the pressure drop over the catalyst bed, which was measured during the experiments, the constants Ω_1, ω_1 and ω_2 of the Eisfeld model (5-28) - (5-31) were adjusted to the measurements. Because of the assumptions which were made for the radial heat transfer model, the contribution of the fluid flow to the total radial heat conductivity, which was found to make around 90 % of the total value, was multiplied with the constant factor $C^{\lambda_{rf}}$. Similarly, the bed-wall heat transfer coefficient α_w was multiplied with the constant factor C^{α_w}. These factors were permitted to vary between 0.8 and 1.2 corresponding to 20 % deviation of the literature models. In general, the tuning of pressure drop and heat transfer parameters is justified, especially because of the presence of the axial thermocouple well, which has a significant impact of the catalyst bed packing (Fig. 42), as well as on the effective tube-to-particle diameter ratio. Since all applied correlations include a dependency on the aspect ratio, a deviation from the literature values is expected.

The intrinsic kinetic parameters were formerly determined in the bench scale reactor (section 4.4.3), in which the catalyst was diluted with inert material, and the operating conditions were different from those applied in the pilot reactor. Especially the diluted catalyst bed despite of which considerable heat effects were still observed, may have interfered on the bench reactor

simulations. Therefore, the intrinsic kinetic parameters (Tab. 6 in section 3.3) too, were permitted to vary within 10 % of their original values.

With the optimized kinetic and reactor model, the parameters of the dynamic phosphorus model can finally be estimated by simulation of the dynamic experiments. The respective parameters to be estimated in each case are resumed in Tab. 13. The exact number of parameters for the activity model depends on the number of site activities, which are necessary to describe the system, so as on the discrimination between dynamic (5-34) and steady state activity model (5-36). Again, only pilot tests *PT1*, *PT2* and *PT3* were used for parameter estimation.

Tab. 13: Estimated parameters by simulation of steady state and dynamic experiments

Steady state experiments		Dynamic experiments	
Radial heat transfer:	$C^{\lambda_{rf}}$, C^{α_w},	Phosphorus adsorption:	k_{Ph}^{ads}, k_{Ph}^{des}, $E^{A,ads}$, $E^{A,des}$
Pressure drop:	Ω_1, ω_1, ω_2,	Water adsorption:	$K_{H_2O}^{ads}$, $\Delta_{ads}H_{H_2O}$
Intrinsic kinetic:	$k_{i,j}^{ref}$, $E_{i,j}^{A}$, K_i^{ref}	Activity:	k_k^{act}, k_k^{deact}, $E_k^{A,act}$, $E_k^{A,deact}$ $\xi_{1,k}$, $\xi_{2,k}$, $\xi_{3,k}$, $\xi_{4,k}$

5.4 Results

5.4.1 Intrinsic kinetic and model parameters

Tab. 14 shows the results of the reactor and kinetic parameter tuning. The simulation of the initial steady experiments revealed that not all adjustable parameters were significant. In terms of the heat transfer model, the measured temperature profiles could be matched best by increasing only the α_w-coefficient by 22 %. In contrast, the proposed radial heat transfer model for the two-dimensional heterogeneous reactor model with the radial heat conductivity parameters according to Zehner, Bauer, Schlünder [56,94] is applicable without any further modifications.

Regarding the pressure drop, it was not possible to describe both tested catalyst shapes with only one set of constants according to the Eisfeld model (5-3), (5-28) - (5-31). Eisfeld and Schnitzlein [86] found Ω_1 = 155, ω_1 = 1.42 and ω_2 = 0.83 for different particle shapes. While in

the present simulations, the original values of Ω_1 and ω_1 could be applied, ω_2 had to be modified individually for each shape within ±15 %. However, taking back in mind the high degree of non-ideality of the catalyst packing in the pilot reactor caused by the low tube-to-particle diameter ratio and the presence of the thermocouple well in the tube center, these minor changes of heat transfer and pressure drop parameters are assumed to be acceptable for the considered range of operating conditions.

Tab. 14: Optimized pressure drop and intrinsic kinetic parameters

Parameter	**Unit**	**Optimum estimate**	**Difference to original value***
$C^{\lambda_{rf}}$	-	1	-
C^{α_w}	-	1.22	+ 22 %
Ω_1	-	155	-
ω_1	-	1.42	-
ω_2 (*C5* / *C6*)	-	0.72 / 0.84	- 13 % / + 2 %
$k_{Bu,MA}^{ref}$	10^{-3} mol/s/kg/bar$^{1.5}$	738.97	+ 8 %
$k_{Bu,CO}^{ref}$	10^{-3} mol/s/kg/bar$^{1.5}$	110.10	- 7 %
k_{Bu,CO_2}^{ref}	10^{-3} mol/s/kg/bar$^{1.5}$	71.83	+ 2 %
$k_{MA,CO}^{ref}$	10^{-3} mol/s/kg/bar$^{1.5}$	34.25	- 7 %
k_{MA,CO_2}^{ref}	10^{-3} mol/s/kg/bar$^{1.5}$	30.96	+ 2 %
$E_{Bu,MA}^{A}$	kJ/mol	86.56	-
$E_{Bu,CO}^{A}$	kJ/mol	105.27	-
E_{Bu,CO_2}^{A}	kJ/mol	108.17	-
$E_{MA,CO}^{A}$	kJ/mol	105.47	-
E_{MA,CO_2}^{A}	kJ/mol	119.67	-
$K_{H_2O}^{ref}$	bar^{-1}	80.94	- 8 %
$K_{Bu,1}^{ref}$	bar^{-1}	403.95	+ 1 %
$K_{Bu,2}^{ref}$	bar^{-1}	446.20	+ 4 %

* Original values determined in the modeling of the bench scale tests

With respect to the kinetic parameters, the activation energies could be kept constant, while the kinetic and inhibition constants varied slightly. The reference state again corresponds to the reference temperature of 420°C. The highest corrections correspond to the reference kinetic constant of the selective reaction (k_1^{ref}, + 8 %) and to the reference inhibition constant of water ($K_{H_2O}^{ref}$, - 8 %). The kinetic constants for the CO formation reactions decreased by 7 %, while those for the CO_2 formation increased by only 2 %. Also the *n*-butane inhibition constants increased only slightly by 1 and 4 %. These minor deviations are again acceptable taking back in mind the above discussed differences between the two applied reactors.

The parity plots in Fig. 44 show that this model reproduces well the measured outlet concentrations of *n*-butane, CO and CO_2, since the majority of the points are within 10 % deviation (solid lines). In order to further underline the quality of the reactor model, the following Fig. 45 - Fig. 47 compare the measured and simulated temperature profiles for the steady state reference conditions for the three considered pilot tests. In each case the measured temperature profiles are most widely located between the simulated profiles of fluid and solid temperature.

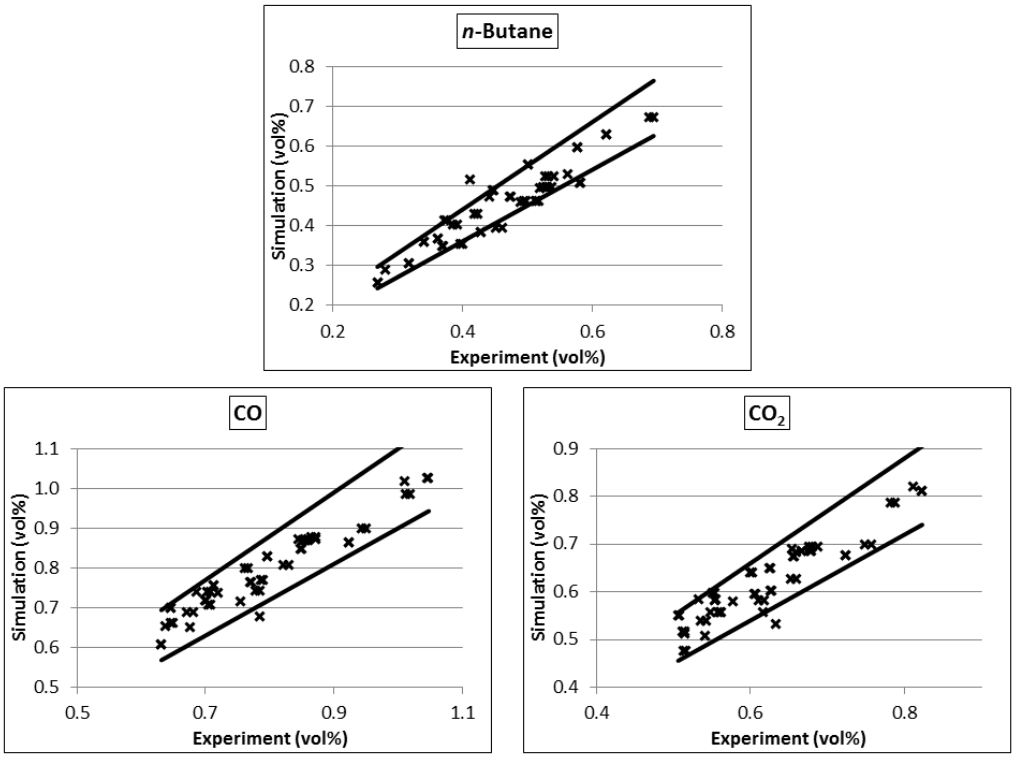

Fig. 44: Parity plots of measured outlet concentrations for the initial steady state experiments (solid lines present 10 % deviation).

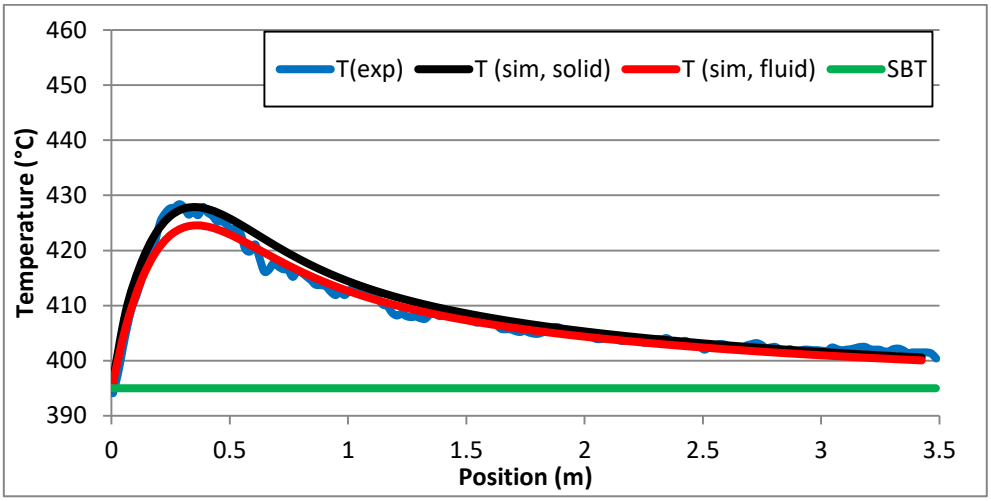

Fig. 45: Measured temperature profile and simulated fluid and solid temperature profiles for *PT1*.

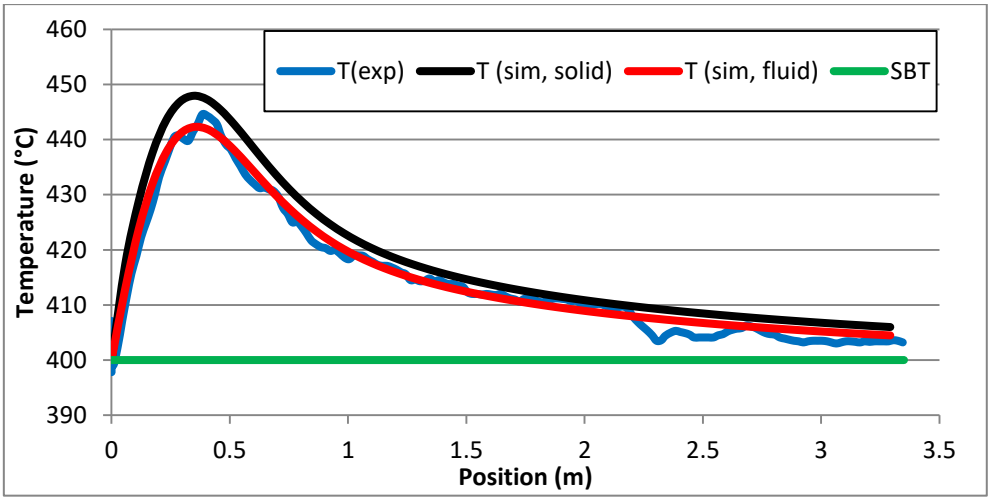

Fig. 46: Measured temperature profile and simulated fluid and solid temperature profiles for *PT2*.

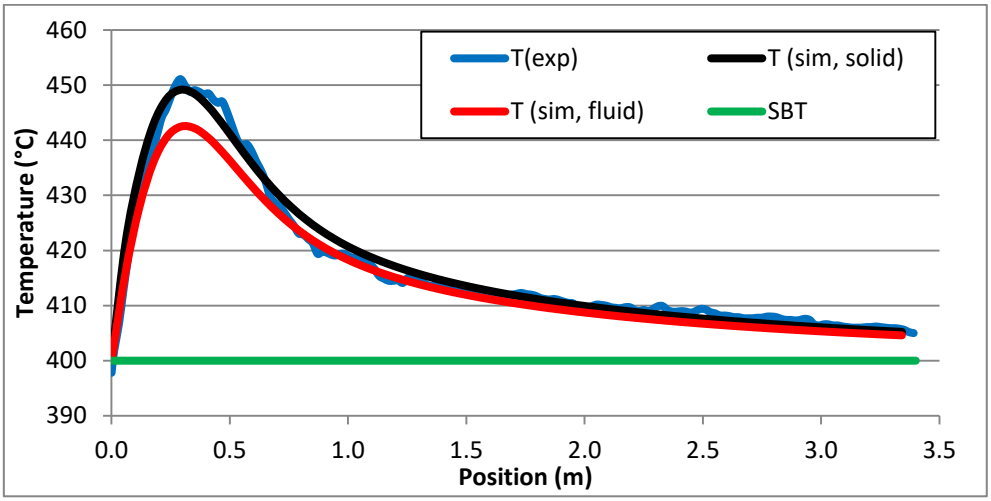

Fig. 47: Measured temperature profile and simulated fluid and solid temperature profiles for *PT3*.

5.4.2 Activity model parameters

With the optimized intrinsic kinetic parameters and reactor model, the activity model parameters (Tab. 13) were estimated by simulation of the phosphorus dosing experiments.

Tab. 15 shows the optimized parameters for the best fit for the dynamic and the steady state activity models, whereas the reference constants again refer to the reference temperature of 420°C. Good results were obtained applying both, the steady state and the dynamic activity model, although the latter achieved a lower sum of the weighted residuals (3rd term in equation (3-40). On the other hand, a number of parameter correlations appeared with respect to the temperature dependence of the rate constants in case of both models (Tab. 16 and Tab. 17). In addition, the water and phosphorus adsorption constants appeared correlated. Further parameter estimations revealed that all correlations disappeared when the activation energies of the adsorption and activation rates were set to zero. However, in this case the value of the objective function increased significantly by 20 to 30 % because of which the appearing correlations were accepted.

Tab. 15: Activity parameter estimation results

			Dynamic activity model		**Steady state activity model**	
	Parameter	**Unit**	**Optimal Estimate**	**95 % Confidence interval**	**Optimal Estimate**	**95 % Confidence interval**
	Weighted residual term (relative)	-	1.00		1.11	
1	$k_{Ph}^{ads,ref}$	mol/kg/h/bar	5464.4	349.5	4195.2	110.5
2	$k_{Ph}^{des,ref}$	10^{-3} mol/kg/h	73.5	0.2	60.3	0.1
3	$E^{A,ads}$	kJ/mol	93.5	0.5	105.0	0.5
4	$E^{A,des}$	kJ/mol	116.9	0.2	64.4	0.5
5	K_{ads,H_2O}^{ref}	bar^{-1}	863.5	58	827.7	33.8
6	$\Delta_{ads}H_{H_2O}$	kJ/mol	-45.6	11.0	-45.0	11.0
7	k_{act}^{ref} (K_{act}^{ref})	h^{-1} (-)	0.5	0.0	2.8	0.1
8	k_{deact}^{ref}	h^{-1}	36.1	1.0	-	-
9	$E^{A,act}$ (ΔE^{act})	kJ/mol	39.8	9.2	-51.0	8.7
10	$E^{A,deact}$	kJ/mol	121.8	8.7	-	-

Tab. 16: Correlation matrix for the dynamic activity model

	1	**2**	**3**	**4**	**5**	**6**	**7**	**8**	**9**	**10**
1	1.00									
2	0.92	1.00								
3	0.58	0.83	1.00							
4	-0.87	-0.67	-0.22	1.00						
5	0.99	0.33	0.62	-0.86	1.00					
6	0.64	0.31	-0.78	0.93	-0.96	1.00				
7	-0.27	-0.63	-0.93	-0.08	-0.33	0.77	1.00			
8	-0.84	-0.98	-0.92	0.52	-0.86	-0.49	0.75	1.00		
9	0.79	0.97	0.93	-0.50	0.83	0.96	-0.80	-0.99	1.00	
10	0.80	0.97	0.93	-0.51	0.84	0.95	-0.79	-0.99	1.00	1.00

Tab. 17: Correlation matrix for the steady state activity model

	1	2	3	4	5	6	7	9
1	1.00							
2	-0.67	1.00						
3	-0.60	0.75	1.00					
4	-0.33	-0.62	0.35	1.00				
5	0.99	0.32	-0.56	-0.86	1.00			
6	0.53	0.41	0.69	0.93	0.94	1.00		
7	0.63	-0.56	0.49	-0.08	-0.71	0.66	1.00	
9	0.89	0.96	-0.92	0.53	0.88	0.91	-0.79	1.00

The simulations further revealed that the measured temperature profiles and outlet concentrations can be described sufficiently well when applying only one activity parameter for all reactions. Introducing a second one for the CO formation reactions according to the remarks in section 3.2, the respective activity constants differed only minimally and provoked more parameter correlations, hence this was ruled out. As the parallel estimation of the exponents, ξ_n, together with the remaining parameters reduced the statistical quality of the results and also significantly increased the simulation time, they were optimized separately. The best fits were obtained using a first order dependency of the catalyst activity on the phosphorus coverage (ξ_3) and an exponent for the dependency on surface water (ξ_1) of 0.33. In case of the dynamic activity model the best fit was further obtained with $\xi_2 = \xi_4 = 1$.

The resulting adsorption constants are in the same range for both models. Also the activity parameters are similar as the steady state reference activity constant fits well the quotient between activation and deactivation constants (K_{act}^{ref} = 2.77, $k_{act}^{ref}/k_{deact}^{ref}$= 2.68) and the steady

state activation energy is in the same range as the difference between the activation energies for the activating and deactivating reactions.

The following figures show the parity plots for the outlet concentrations (Fig. 48), as well as the comparison between measured and simulated temperatures at the initial hot spot position over the time (Fig. 49 - Fig. 51), applying the dynamic activity model. Although the distribution of the outlet concentrations (Fig. 48) is broader than in case of the steady state simulations (Fig. 44) and some more points are located outside the 10 % deviation (solid lines), the results are still very good taking into account, the many assumptions, the large number of measurements, and the long experimental times which are continuously integrated by the model. The latter aspect is further underlined by regarding Fig. 49 - Fig. 51. The measured temperatures at the initial hot spot position in the catalyst bed are reproduced very well by the model over time intervals up to 360 h.

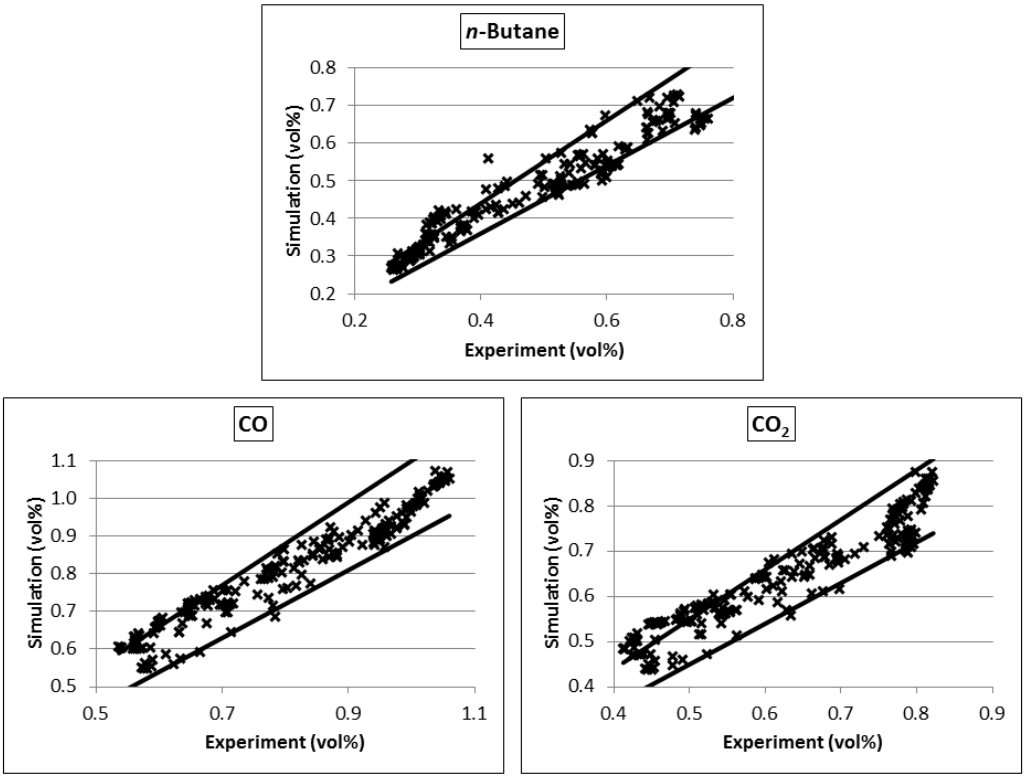

Fig. 48: Parity plots of measured outlet concentrations for all dynamic experiments (solid lines present 10 % deviation) applying the dynamic activity model.

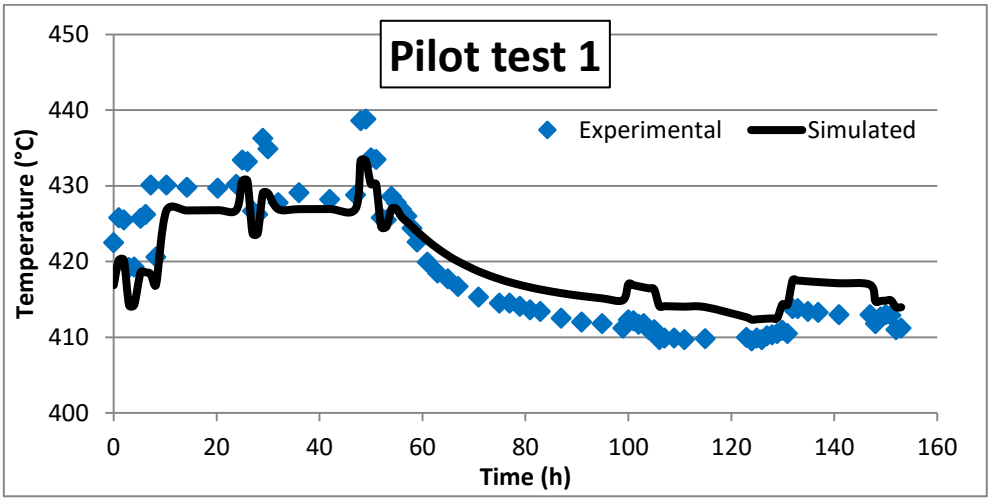

Fig. 49: Measured temperature and with the dynamic activity model simulated catalyst temperatures at the axial catalyst bed position at which the hot spot was initially located in experiment *PT1*.

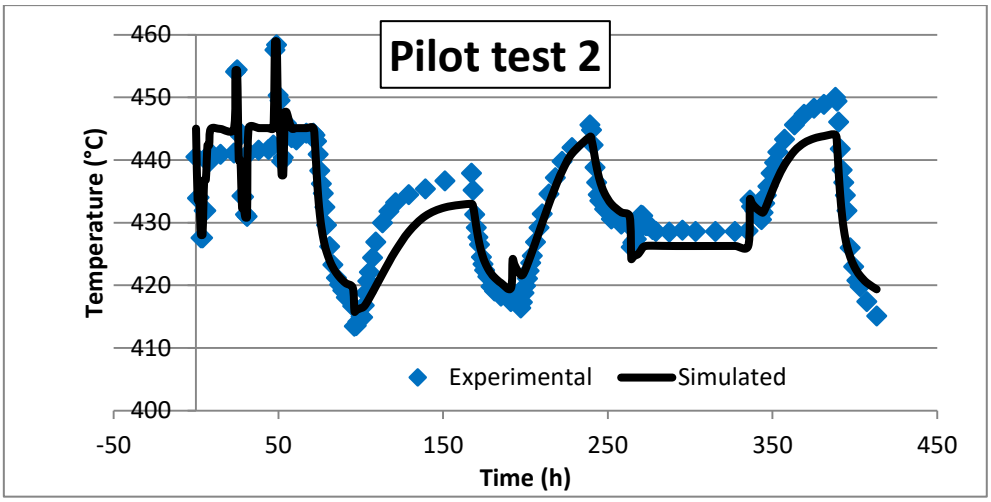

Fig. 50: Measured temperature and with the dynamic activity model simulated catalyst temperatures at the axial catalyst bed position at which initially the hot spot was located in experiment *PT2*.

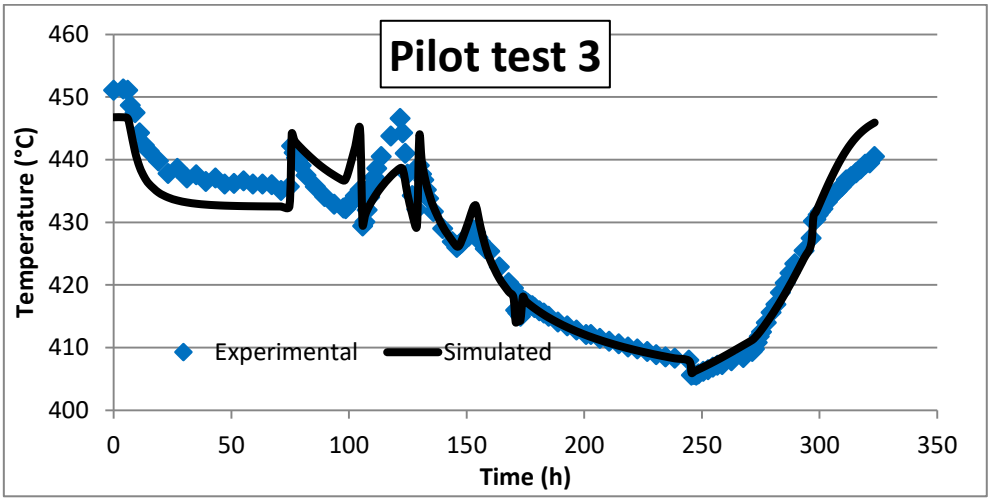

Fig. 51: Measured temperature and with the dynamic activity model simulated catalyst temperatures at the axial catalyst bed position at which initially the hot spot was located in experiment *PT3*.

With respect to the observed interaction between phosphorus, water, and catalyst activity, Fig. 52 - Fig. 57 present the simulated temperature profiles corresponding to the examples of phosphorus addition (Fig. 32) and interruption of the water feed at constant TMP feed (Fig. 37), which were presented in section 4.4.2 and 4.4.3. The model is able to reproduce the measured profiles very well in both, height and form. Minor deviations in the temperature profiles are supposed to especially arise from the long continuous simulation time intervals and the therefore very probable error progressions.

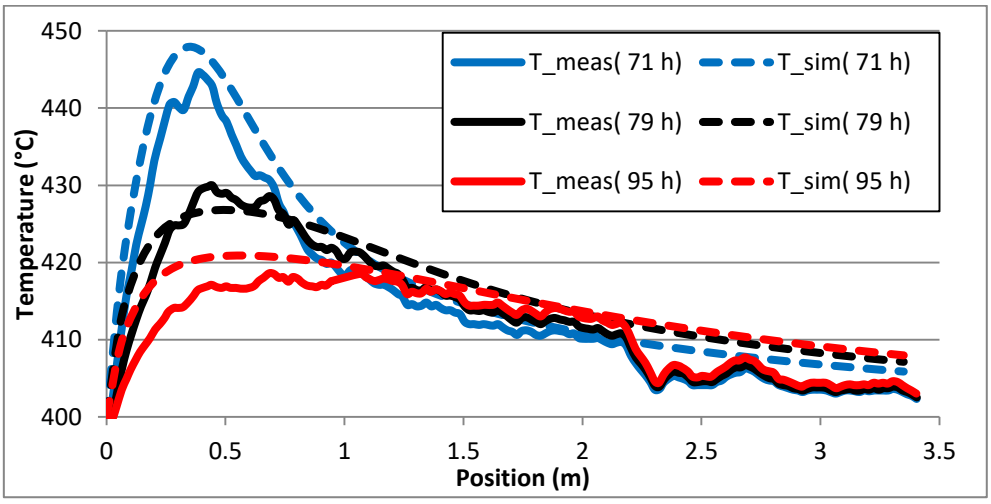

Fig. 52: Measured and with the dynamic activity model simulated catalyst temperature profiles after adding ca. 5 ppmv TMP after 71 operating hours.

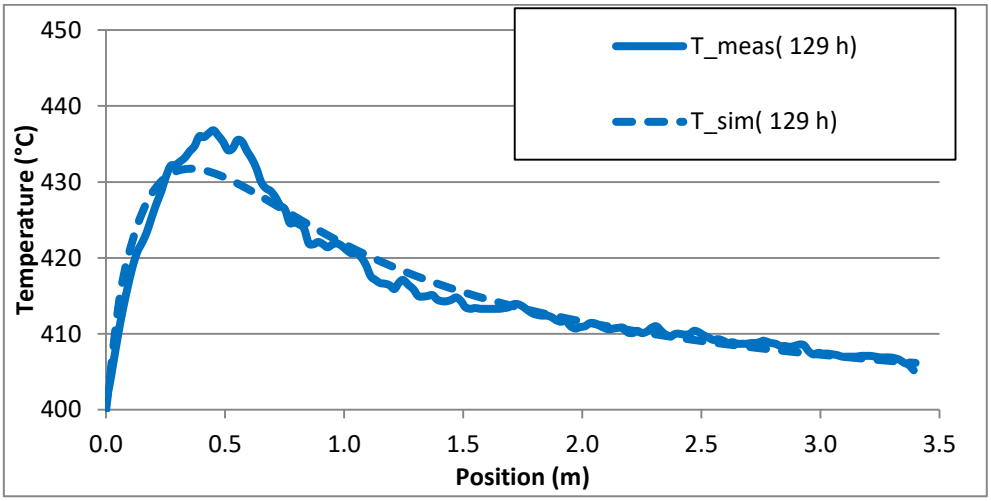

Fig. 53: Measured and with the dynamic activity model simulated catalyst temperature profiles before stopping the water feed after 129 h.

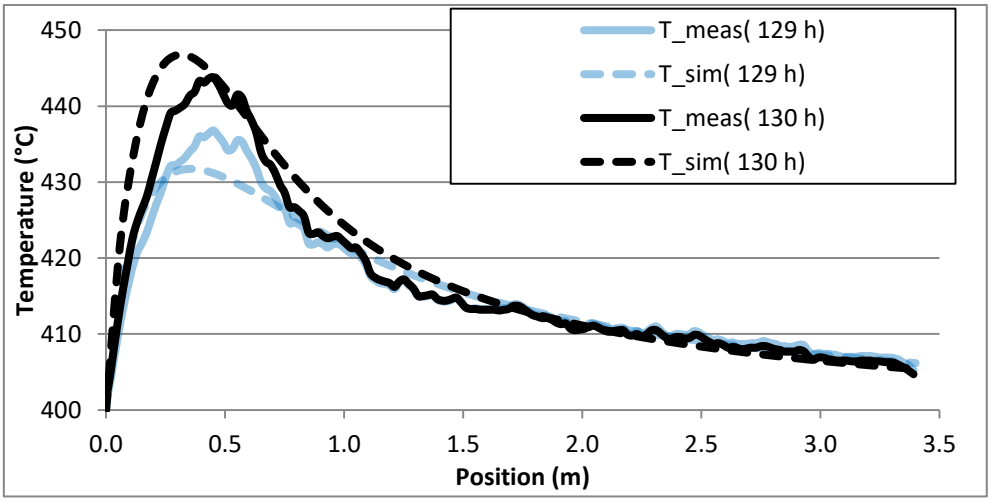

Fig. 54: Measured and with the dynamic activity model simulated catalyst temperature profiles 1 h after stopping the water feed after 129 h TOS.

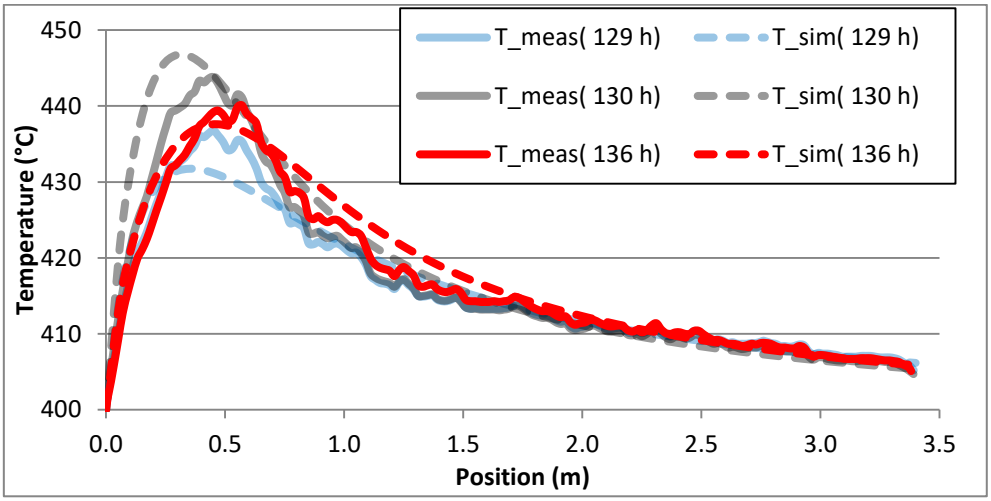

Fig. 55: Measured and with the dynamic activity model simulated catalyst temperature profiles 7 h after stopping the water feed after 129 h TOS.

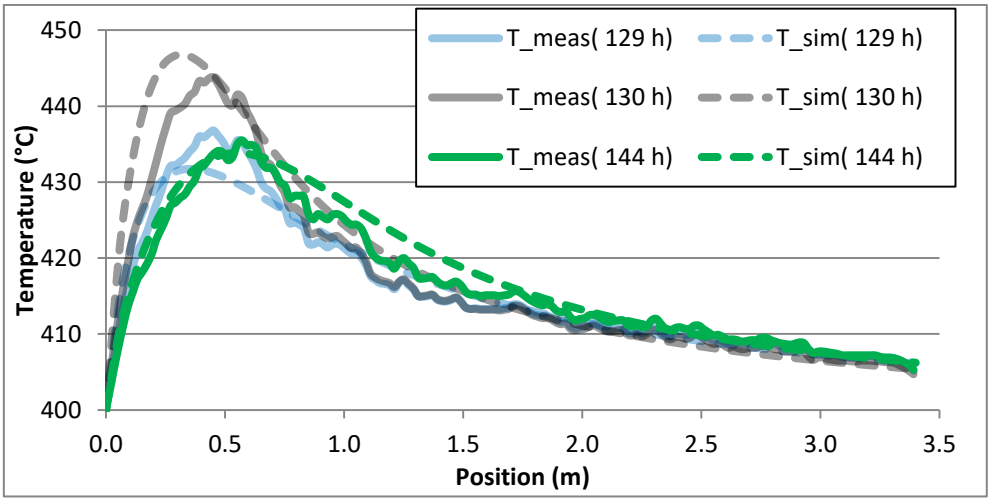

Fig. 56: Measured and with the dynamic activity model simulated catalyst temperature profiles 15 h after stopping the water feed after 129 h TOS.

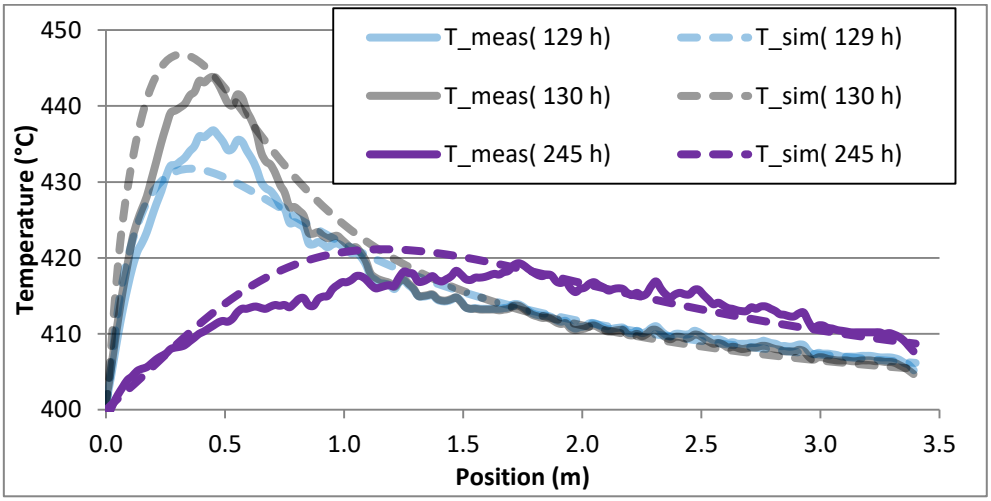

Fig. 57: Measured and with the dynamic activity model simulated catalyst temperature profiles 126 h after stopping the water feed after 129 h TOS (TMP feed was increased from ca. 3 to 5 ppmv after 153 h).

5.5 Discussion

The derived two-dimensional heterogeneous reactor model with the modified radial heat transfer model is able to describe the industrial scale fixed bed pilot reactor very well in terms of both, concentration and temperature profiles. The intrinsic kinetic parameters which were previously determined in the smaller bench scale reactor could be used after small variations of only up to 8 % of the initial values. These deviations are acceptable taking into account the above discussed differences between the two reactor setups and operating conditions.

The correction of the pressure drop und heat transfer parameters is considered to be acceptable, especially because of the presence of the axially centered thermocouple well which causes bigger inhomogeneities in the catalyst packing, such as additional wall effects at the tube center and filling voids (Fig. 42). This is one important difference as compared to commercial reactors which do not contain axial thermocouples and in which the catalyst packing should thus be more homogeneous. Therefore, the estimated model corrections are only valid for the applied pilot reactor and the model is hence not directly transferable to commercial reactors.

Another consequence of the inhomogeneous catalyst packing is that an exact radially and axially resolved void fraction profile as required by the $\lambda_r(r)$-model is not accessible for the applied reactor system and would most probably also require unprovable assumptions and corrections for this model. In this light, the choice of the α_W-model, which implies the use of mean bed property parameters, is understandable. This emphasizes the still existing lack of appropriate heat transfer models for two-dimensional heterogeneous reactor models. In the light of their

importance for the simulation of processes with large radial temperature gradients, the development of more complex models should be the focus of future research.

The resulting radial heat transfer resistances are illustrated in Fig. 58, which shows a simulated radial temperature profile at the hot spot position. According to the simulations, the main heat transfer resistance at the simulated steady state equilibrating conditions is located at the inner wall, where the step change in temperature (ΔT = 27 K) which is caused by the model assumptions of the α_W-model, is much higher than the gradient within the catalyst bed (ΔT = 14 K). Similar findings were made among others by Wen and Ding [102]. The temperature difference between solid and fluid is constantly below 10 K, which is also in a typical range [91,103]. Regarding the contributions to the total radial bed conductivity (5-45), the model predicts that the fluid flow (Pe_0/K_r) constitutes up to 90 % at the applied experimental conditions. The remainder equally distributes on the static contributions of solid ($\lambda_{r,0}^{ss}/\lambda_f$) and fluid ($\lambda_{r,0}^{f}/\lambda_f$) phases. Hence, the optimization of the fluid flow contribution only is justified. Although the predominance of the fluid flow contribution may support the more common method of assigning the complete radial heat conductivity to the fluid phase, own simulations showed that the temperature difference between fluid and solid may exceed 10 K in that case. Therefore, the presented method is kept.

$$\frac{\lambda_r^{eff}}{\lambda_f} = \frac{\lambda_{r,0}^{ss}}{\lambda_f} + \frac{\lambda_{r,0}^{f}}{\lambda_f} + \frac{Pe_0}{K_r} \tag{5-45}$$

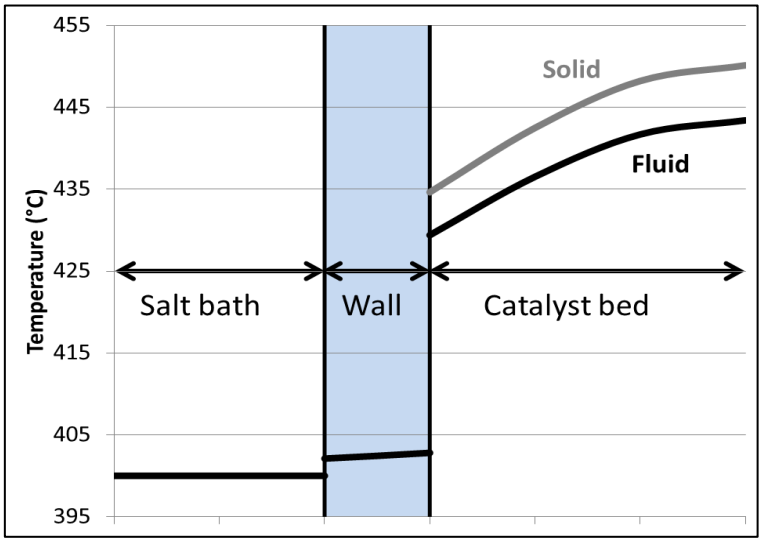

Fig. 58: Simulated radial catalyst temperature profile at the position of the temperature hot spot at equilibrating conditions.

Another important conclusion of the successful simulation of the steady state experiments by one set of kinetic parameters is that despite the different applied equilibrating conditions and times during the different tests, the active surface that formed on the catalyst did not differ significantly. In other words, the applied range of different start up procedures had no significant influence on the catalyst activity during the first operational steady state. This of course should not be extrapolated to a broader range of equilibration conditions, but requires more investigation in future works.

The presented activity model is able to describe the performed pilot reactor experiments very well over time intervals of up to two months, during which height and form of the temperature profiles changed significantly. Comparing to the simple approach of Diedenhoven *et al.* [97] it contains a lot of additional mechanistic information, which was necessary for a qualitative and quantitative description of the changing catalyst performance. Still, the model is a rather condensed resume of the complex scheme of which was previously developed in this work (Fig. 41 in section 4.5). It comprises two reversible reactions. A slow, reversible phosphorus adsorption is expressed by a Langmuir type adsorption kinetics and is influenced by water. The formation of active sites is proportional to the actual number of inactive sites and the surface concentration of water while the rate of decomposition of active sites increases with the surface concentration of phosphorus and is further proportional to the actual catalyst activity. Phosphorus diffusion in the catalyst pores, bulk or on the catalyst surface, or the bulk diffusion of oxygen are not included. According to section 4.5 the diffusion of oxygen, which is essential for the conversion of *n*-butane to MA on the catalyst surface, is enhanced by the presence of water and inhibited by excess phosphorus. In the model, these effects are surmised in the reactions of formation and decomposition of the active sites. These assumptions were successful and essential in the present work leading to the highest agreement between experiment and simulation.

The effect of water on the phosphorus distribution over the catalyst is supposed to be due to the enhanced diffusivity of phosphorus in the catalyst, although a direct effect on the adsorption-desorption process is also conceivable. In the presented model, this interaction is expressed only by the competing adsorption between phosphorus and water whereas the latter is assumed to be faster, resulting in permanent equilibrium. According to the simulations and with the applied conditions, the phosphorus coverage varies between 0 and 5 % in most parts of the bed (Fig. 59), but it reaches up to 50 % in the first 0.5 m of the bed when no water is fed (Fig. 60). The resulting activity profiles are inversely proportional to the profiles of the phosphorus coverage, as expected. Since the model does reproduce well the progress of the temperature profile after phosphorus induced dynamic changes (Fig. 52-Fig. 57), it may be concluded that also the resulting qualitative and quantitative progress of the activity profile is correct. On the other hand, due to the lack of experimental confirmation, it remains an open question if the predicted phosphorus profiles are correct, too.

The nature of adsorbed excess phosphorus and its migration through the catalyst bed have hardly been considered in the literature. The presented model includes only surface adsorption

equilibrium for a hypothetical phosphorus species, which contains one phosphorus atom according to TMP. The transport through the reactor thus occurs only through the gas phase. According to the discussions in section 4.5 however, also catalyst bulk and surface diffusion mechanisms could contribute to the axial distribution of phosphorus in the catalyst bed. Additionally, it was assumed that phosphorus adsorbs on the same surface sites as water, and that the surface phosphorus presents no concentration gradient in the catalyst pores. These assumptions were successful in the present work and it is important to note that the parameter estimation results were significantly worse when neglecting the water adsorption. However, there is no evidence about the exact sorption mechanisms since they hardly have been investigated so far. The absence or presence of such gradients have to be determined experimentally and may be influenced by the contribution of surface and bulk diffusion mechanisms. A better understanding of these processes is needed to further improve the model and should be considered in future investigations.

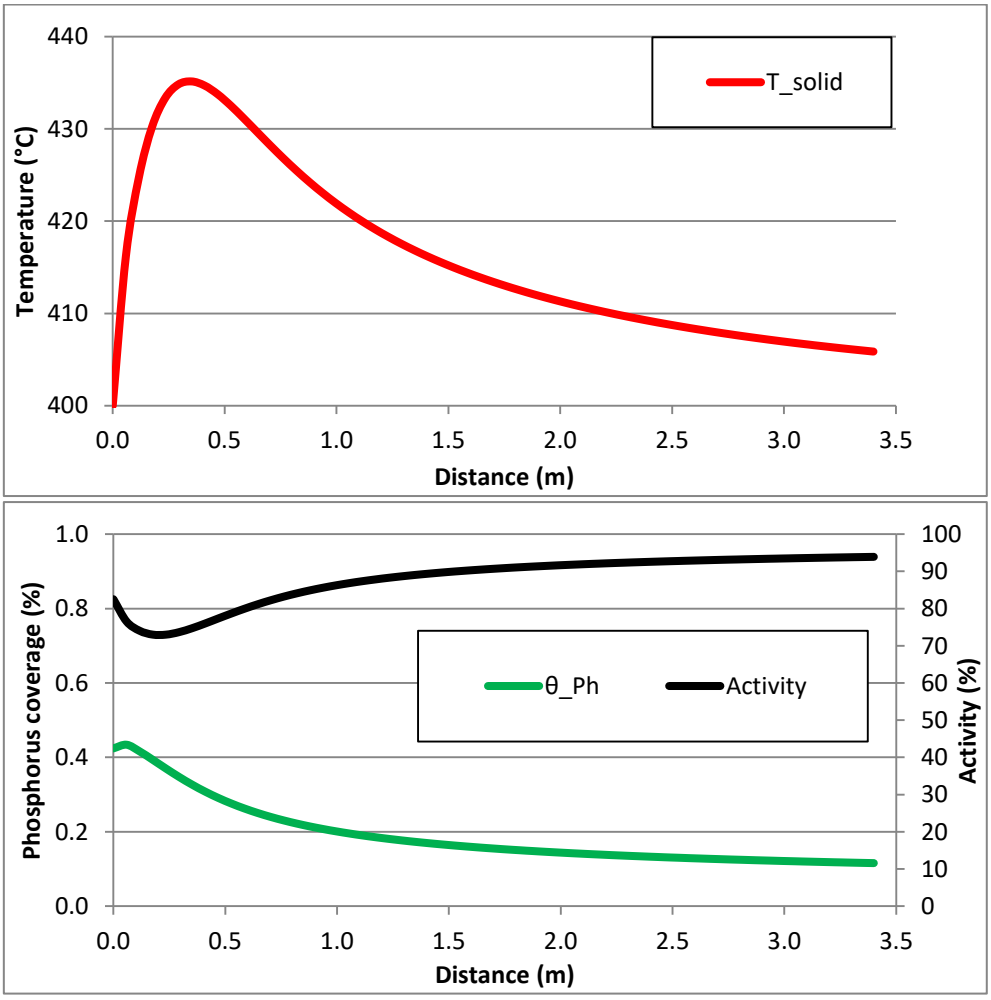

Fig. 59: Simulated profiles of catalyst temperature, phosphorus coverage (θ_{Ph}) and catalyst activity along the central axis for operation with 1 ppmv TMP and 2 vol% H_2O at stationary state.

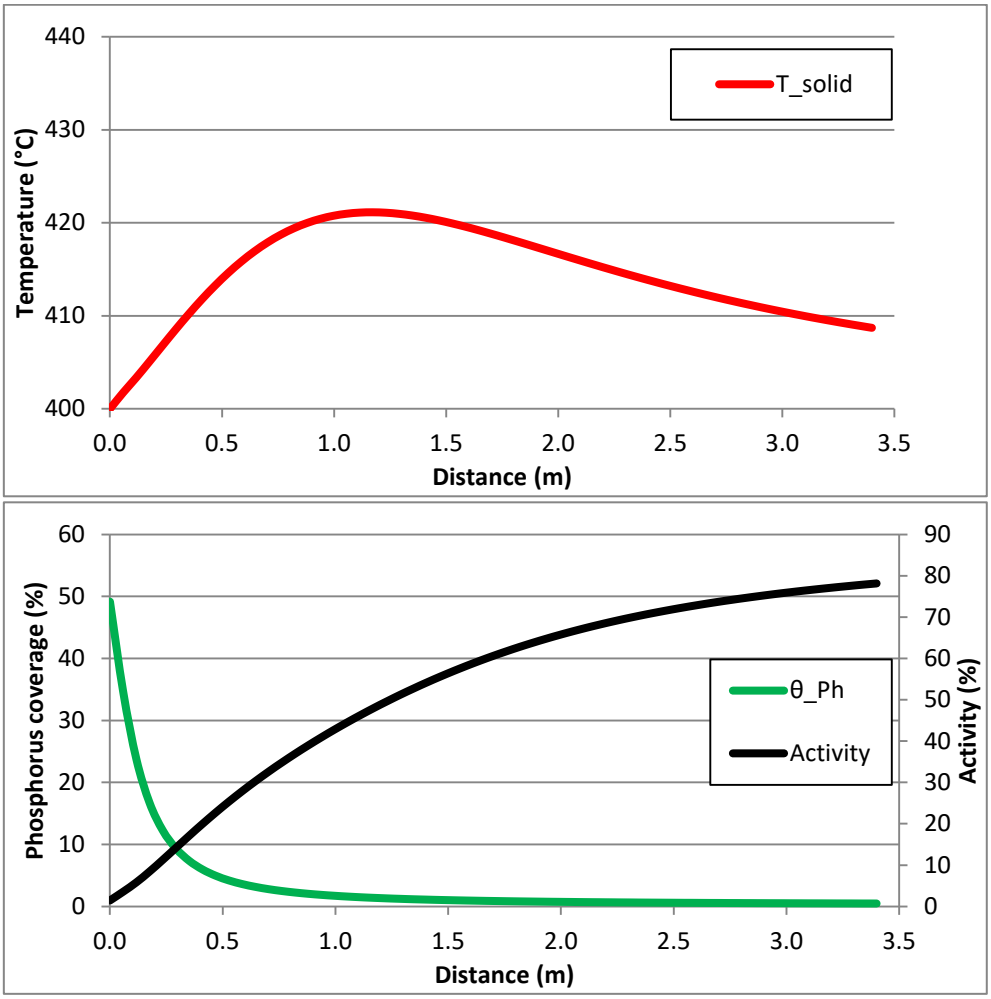

Fig. 60: Simulated profiles of catalyst temperature, phosphorus coverage (θ_{Ph}) and catalyst activity along the central axis for operation with 5 ppmv TMP and no water at stationary state.

It is important to note that the applied model for the phosphorus dynamics includes only fully reversible surface effects, which according to the simulation results are sufficient to describe the performed experiments very well over time intervals of up to two months. This result further indicates that during the considered period no significant changes in the intrinsic catalyst activity occurred like the formation of $VO(PO_3)_2$ or V_2O_5. On the other hand, when significantly longer operation times are considered, especially the bulk diffusion of phosphorus may have to be included into the description. The effects of related structural transformations of the catalyst bulk on the intrinsic catalytic activity, may also appear on much longer time scales which, however, was not investigated in this work. The same accounts for the appearance of extreme conditions as applied by Cavani *et al.* [39]. During experiments of *in situ* removal and reintegration of phosphorus, the authors observed an irreversible loss of selectivity, which cannot be described by the presented model of this work.

Nature and diffusion mechanisms of active oxygen species too are not considered in the model. The presented experiments could be well described without any influence or consumption of oxygen in the dynamic formation reactions of the active sites. If however orthophosphates are components of the active sites according to the proposed scheme in section 4.5 (Fig. 41), their formation should include an oxidizing step of the VPP precursor. The reason that such step was not necessary for the simulations may be that in the fixed bed process with air, oxygen is abundantly present. Another explanation is that the two-dimensional active surface first forms on the VPP precursor under the influence of water according to the proposed scheme of Bluhm *et al.* [64]. The reported active orthophosphate species [39,40,42,59,60] are then formed on these two-dimensional structures. In the presented model, this is included as oxygen is only consumed in the conversion of hydrocarbons whereas the intrinsic reaction rates depend on the partial pressure of oxygen. Together with the effects of water and phosphorus on the formation reaction of active sites, the literature reports according to which excess phosphorus prevents and water enhances the oxidation of the catalyst [6,39,40] are hence included in the model.

Another coincidence between the estimated model parameters and the findings of Cavani *et al.* [39,40] is that the activation energy of the formation reaction of the active sites is lower than that of the decomposition reaction. At certain surface concentrations of water and TMP, the concentration of active sites is thus higher at lower temperatures. Accordingly, the authors of [39,40] reported that the addition of water to a catalyst containing excess phosphorus permits the formation of active δ-$VOPO_4$ already at reduced temperatures.

The fact that only one activity factor was sufficient to describe all the experiments does not necessarily contradict the findings in section 3.3. The experiments in the bench reactor indicated that the formation of CO may be differently inhibited by the concentration of *n*-butane. It was thus concluded that in the corresponding reactions different active sites are involved as compared to the formations of MA and CO_2. The results in this section suggest that both sites are equally affected by the phosphorus concentration on the catalyst surface. In accordance with the statements in section 4.5 the following mechanism appears conceivable. The *n*-butane molecule is activated on one active site, and remains anchored on the catalyst surface during the complete conversion. Thereby, the dynamic phase equilibrium promotes the supply of oxygen, whereas the formations of MA and CO_2 may be facilitated by different phases present than the formation of CO. The fact that apparently all reaction paths are equally influenced by the presence of excess phosphorus suggests that phosphorus inhibits primarily the formation of the *n*-butane activating sites. However, this is in contrast to the findings of Cavani *et al.* [39,40] who found different selectivities as a function of phosphorus content and operating conditions. The cause of these differences may be that the synthesis of catalysts with lower P/V ratio as performed in [39,40] leads to a different bulk structure, which effects on the surface dynamics. This aspect again highlights the importance for future works to investigate the interactions between bulk and surface of VPO catalysts and to include this into more detailed models for the description of the activity dynamics.

6 Conclusion and outlook

The industrial manufacture of maleic anhydride (MA) by selective oxidation of *n*-butane over VPO catalysts is well known to be a dynamic process during which catalyst performance changes with time and operating conditions. There is a general agreement that a loss of phosphorus is responsible for this behavior. Therefore, a variety of technologies are claimed compensating this loss in order to ensure optimum operation of commercial reactors. This implies the addition of an organic phosphorus compound, such as trimethyl phosphate (TMP), to the reactor feed. Furthermore, the addition of water seems to play an important role for an adequate distribution of phosphorus in the catalyst bed. The aim of the presented work was the kinetic description of the dynamic behavior of industrial VPO catalysts for the manufacture of MA in a catalytic fixed bed pilot reactor. The necessary tools for this objective were the experimental investigation and modeling of the intrinsic reaction kinetics, as well as of the phosphorus dynamics.

Reaction network and kinetics of the selective oxidation of *n*-butane to MA were investigated in a bench scale reactor, in which different cylindrical and ring shaped particle geometries of a full body VPO catalyst were filled together with inert material. Actually, the reactor configuration was not ideal for investigating the detailed reaction network and kinetics, since it was not possible to dosage any reaction products and to establish isothermal conditions. However, the experiments revealed some important aspects about the formation of the by-products CO and CO_2, which so far hardly have been considered in detail in the literature.

The CO/CO_2 ratio was found to decrease with increasing conversion, but it also increased with reducing *n*-butane inlet concentration. The results suggest that at least CO is formed by a different reaction mechanism and/or on different kind of active sites. Common literature kinetic models, which in the past were used for reactor modeling, do not account for this behavior, because of which the performed experiments of this work were used for kinetic modeling. Different kinetic models were deduced for a network of five reactions, the selective conversion to MA, so as the over-oxidations of *n*-butane and MA towards CO and CO_2 respectively. The reaction rate equations are similar to existing literature models, with the difference that it is explicitly distinguished between the formation paths of CO and CO_2. Satisfactory results were obtained with an Eley-Rideal type Hougen-Watson model, where the rate equation for the CO formation contains a different constant for the *n*-butane inhibition than the other reactions. All reactions are further inhibited by water and proportional to the concentration of oxygen by the power of 0.5. The order with respect to the hydrocarbon is one.

During the kinetic modeling, all non-ideal aspects of the laboratory reactor were tried to be included in the applied reactor model. The same accounts for diffusion resistance in the catalyst pellets which were described by means of an effective Fickian diffusion model. The applied procedure finally permitted a good description of different catalyst shape geometries by one kinetic model. Therefore, the developed model should also be directly applicable to different commercially applied full body catalyst shapes. However, it is surely recommendable to investigate the reaction network and kinetics again in the light of the findings of the presented

work, applying a more suitable reactor system in which temperature and diffusion related interactions are minimized, and which additionally permit the dosage of reaction products to the reactor feed stream.

The fact that already during the kinetic experiments an unsteady catalyst behavior was observed implies a further influence on the modeling results. Catalytic performance and properties as BET surface area and P/V ratio were found to vary as a not definable function of operating conditions and time. In some cases in which the catalyst reactivated after prolonged runs at high temperature, chemical analysis of the used catalyst supported the common assumption of the literature that a loss of phosphorus is responsible for the unsteady behavior. However, the varying extent of dynamic effects during the experiments and the high variance of the analysis results reduce the validity of these findings. Therefore, nature and cause of such changes too should be investigated in more detail in a more ideal reactor system.

The dynamic behavior of a full body shaped VPO catalyst was investigated separately in an industrial scale fixed bed pilot reactor. In the light of its industrial importance, the addition of phosphorus and steam to the reactor feed was focused. If the reactor is operated without phosphorus addition during prolonged periods, an increase in activity and simultaneous loss in MA selectivity drive the operation in a less stable region with the risk of runaway. The underlying effects are probably the same as in case of the laboratory reactor experiments although this was not focused in this work. The addition of small amounts of phosphorus to the reactor effects a very slow, but reversible deactivation. In addition, these dynamic activity processes are strongly influenced by the presence of water. The addition of water was found to effect a fast intrinsic inhibition of the reactions, but on a longer time scale it provoked a reactivation of the catalyst when it formerly had been damped with TMP. Hence, an optimum dosage of both, water and phosphorus permits the control of the temperature profile and MA yield in the fixed bed reactor.

Comparing the presented experiments with the long standing, often contradictory, scientific literature about reaction mechanism and active VPO surface, it was further possible to find common aspects, which might be summarized in a scheme for the VPO chemistry. According to this model, the active surface is a two-dimensional structure composed of various surface species, which may have various functions in the different reaction steps. This surface is formed on the VPP precursor under reaction conditions under the influence of water, while its composition is further determined by the phosphorus concentration at the catalyst surface. The surface concentration is influenced by the adsorption equilibrium of gas phase phosphorus, as well as by the diffusion of phosphorus between catalyst bulk and surface. The diffusion again is facilitated by the water induced two-dimensional structure of the catalyst surface, which is also responsible for the easy access of oxygen atoms necessary for the *n*-butane oxidation. It must again be underlined that the proposed model is not based on detailed analysis studies. Instead it should be considered as a theoretical approach which was deduced by discussing the experimental observations in the light of the diverse scientific literature about the underlying reaction mechanism.

Forthcoming works should hence take into consideration the dynamic processes occurring on the VPO surface and focus more on the role of phosphorus and water in the reaction mechanism. Additionally, the formation mechanisms of the nonselective byproducts acrylic and acetic acid, as well as CO and CO_2 and their relation to the presence of different surface species requires more precise investigation. A suitable experimental set up may be a micro-reactor, which permits the implementation of *in situ* analysis technics and a dosage system for TMP and water. Flexibility in the setting of operating conditions should further permit the investigation of a broad range of conversion and gas compositions.

The experimental periods in this work were several weeks which comparing to catalyst lifetimes of several years are still related to start of run conditions. During this time, all observed effects were reversible. Since the diffusion of phosphorus in the catalyst bulk however is supposed to be much slower than the adsorption dynamics, related long term changes of the bulk phases probably occur to a significant extent only on a longer time scale. Hence, such effects should not play any role during the experiments of the present work. Therefore, care should be taken when extending the proposed reaction scheme to longer operation times. This too should be focused in forthcoming works and combined with advanced characterization methods.

The proposed VPO reaction scheme was used as a basis for a mathematical model for the description of the observed phosphorus dynamics. This dynamic activity model was then implemented in a two-dimensional heterogeneous reactor model for the applied pilot fixed bed reactor, which was finally used for parameter estimations. The radial heat transfer in the reactor was described by a slightly modified α_w-model according to which the static contribution to the effective radial bed conductivity was distributed over the gas and the solid phase respectively. The dynamic contribution and the wall heat transfer coefficient were assigned to the gas phase only. With this model and minor optimizations of the intrinsic kinetic parameters, pressure drop parameters and the wall heat transfer coefficient, the pilot reactor could be described very well in steady state. However, there is still a common lack of appropriate heat transfer models for two-dimensional heterogeneous reactor models. In the light of their importance for the simulation of processes with large radial temperature gradients these more complex models should be focused in the future. Another consequence of the unideal catalyst packing of the pilot reactor relates to the transferability of the developed model to commercial reactors. As commercial reactors do not include axial thermocouples the catalyst loading is much more homogeneous. The developed model of this work with its optimized heat transfer and activity parameters can therefore not be transferred directly to commercial reactors.

The dynamic activity model comprises two reversible reactions. A slow, reversible phosphorus adsorption is expressed by a Langmuir type adsorption kinetic expression. Water adsorption is assumed to be faster reaching equilibrium at any time. The formation of active sites is proportional to the actual number of inactive sites and the surface concentration of water. The latter is according to the formerly proposed mechanism according to which water drives the system in a two-dimensional state, which facilitates the mobility of the three oxygen atoms necessary for the conversion of *n*-butane to MA. The activation process is inhibited by the

presence of surface phosphorus. Accordingly, the rate of decomposition of active sites increases with the surface concentration of phosphorus and is further proportional to the actual catalyst activity.

The diverse influence of water is hence included in three ways. According to the fast reduction of hot spot temperature and conversion, which was observed after increasing the feed concentration of water, the intrinsic kinetic expressions contain a respective inhibition term. The slower activating effect of water when the catalyst has been damped with phosphorus is included by the competitive adsorption between water and phosphorus, as well as by the accelerating impact on the formation of active sites.

The overall kinetic model thus distinguishes explicitly between intrinsic kinetics and phosphorus induced activity dynamics. In the presented work, this was possible as all phosphorus related processes were induced by the addition of TMP to the reactor feed and appeared to be completely reversible. Since during the kinetic experiments in the bench reactor neither phosphorus nor water were fed, the model activity is constantly one during these experiments, neglecting the observed minor activity changes. Diffusion of phosphorus between bulk and surface where it can desorb to the gas phase according the reported loss of phosphorus is not included in the model. Hence, it cannot describe irreversible changes in catalyst performance after prolonged runs without phosphorus addition and at high temperatures. In this light, future studies with focus on irreversible dynamics during start up and prolonged runs without phosphorus addition, should also be evaluated kinetically. For this goal, the underlying VPO chemistry and phosphorus and oxygen transport processes must be identified too and included in the activity model.

Despite these constraints, the model describes very well the overall reactor performance in terms of conversion and selectivity at the reactor outlet and axial temperature profiles. However, concentration measurements at very low conversions could further improve the model since they are related to the most significant temperature variations, which were observed in the first third of the catalyst bed. In order to additionally reduce influences of the non-ideal characteristics of the applied pilot scale reactor, it may again be recommended to make recourse of a micro-scale reactor which permits the dosage of TMP and water.

Keeping in mind the above described limitations it can be summarized that the ambition of developing a model for the description of industrial scale fixed bed reactors for the manufacture of MA from *n*-butane including the performance determining phosphorus dynamics was successfully achieved in this study. A decisive measure therefore was the inclusion of more recent research works, which consider the working VPO surface as a dynamic complex. So far, kinetic models for reaction engineering calculations are commonly based on a simple site isolation concept according to which an active site is a constant quantitative property of a catalyst. The presented study however shows that in case of VPO catalysts the active surface under process condition is a highly dynamic construct because of which common literature kinetic models are not sufficient for a feasible description of the industrial reactor. The developed model of this work includes an extension of the site isolation concept, being the

active sites not completely defined constructs, which dynamically form and decompose as a function of time and operating conditions. The presented study further shows the importance of including industrially relevant aspects like the necessity of an adequate dosage of TMP and water into the fundamental research about the VPO chemistry. For future works, it is thus essential that different research approaches go hand in hand. This conclusion of course expands to other heterogeneous catalytic reactions.

A. Annex

A.1 Experimental methods

A.1.1 TMP dosage system

The TMP saturator consists of a double walled measuring cylinder containing an inner tube with liquid trimethyl phosphate and an outer tube with temperate water. TMP is carried to the reactor feed gas by a flow of pure nitrogen which bubbles through the liquid. The concentration is adjusted through the vapor pressure by controlling the temperature of the circulating water. Calculations to set up a certain TMP concentration are based on the Antoine equation with the constants as found in [71]:

$$\log(p_{TMP}) = A - \frac{B}{T+C} \qquad A = 4.96817, B = 2249.287, C = -12.294 \qquad \text{(A-1)}$$

The final TMP concentration in the reactor feed results in

$$x_{TMP,Feed} = \frac{p_{TMP}}{p_{Sat} - p_{TMP}} \cdot \frac{\dot{V}^N_{N_2,Sat}}{\dot{V}^N_{Feed}} \qquad \text{(A-2)}$$

A.1.2 Evaluation of concentration measurements

The quantitative analysis of the organic compounds was conducted by a standard gas chromatograph (Agilent 6820N) capillary column (Restek RTX1701, 30 m), a split injector and a flame ionization detector. The sampling gas passes through a sample loop connected to a 6-port-2-position valve. By switching the valve, the sample loop volume is carried to the split injector by a helium flow. In normal position, the outlet of the sample loop leads first to a series of wash bottles were in which all organic acids are absorbed in water. At continuation, the gas phase water is condensed in a Peltier cooler at 5°C before entering the infrared analyzer (Emerson NGA2000) which conducts the quantitative analysis of *n*-butane, CO and CO_2.

After injection of the sample gas into the capillary column, the timely separation of the organic gas components, *n*-butane, MA, acetic acid (AcA) and acrylic acid (AcrA), is optimized by conducting a series of temperature ramps. The integrator of the GC software (Chemstation software, Version A 10.4) calculates the peak area corresponding to the respective retention time (Fig. 61) at which each organic gas component is separately eluted. From the peak areas

the molar flows are calculated with the response factors relative to MA. These factors were frequently determined by measuring different calibration solutions.

$$RF_i = \frac{\dot{n}_i / A_i}{\dot{n}_{MA} / A_{MA}} \qquad \text{i = AcA, AcrA} \qquad \text{(A-3)}$$

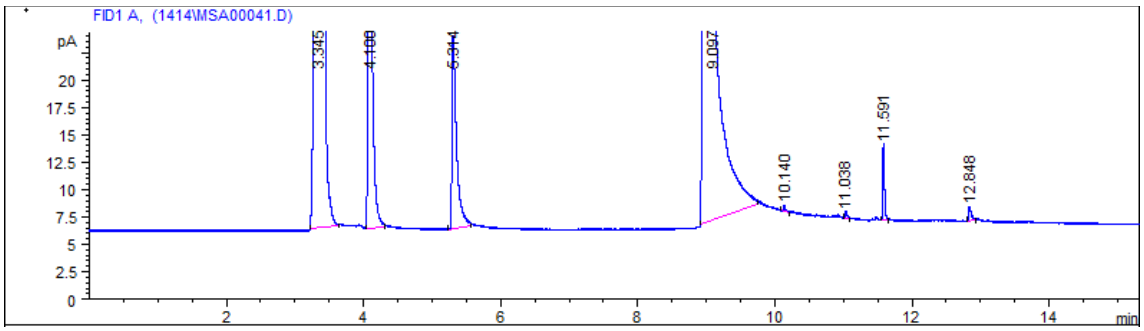

Fig. 61: Chromatogram of a measurement of the pilot reactor outlet gas.

As all acidic compounds are washed out from the sampling gas before entering the IR-spectrometer, the resulting material balances are:

$$\dot{n}_i = x_{i,IR} \cdot \left(\dot{n}_{Bu} + \dot{n}_{CO} + \dot{n}_{CO_2} + \dot{n}_{O_2} + \dot{n}_{N_2}\right) \qquad \text{i = Bu, CO, CO}_2 \qquad \text{(A-4)}$$

Adding the four elemental balances of carbon, hydrogen, oxygen and nitrogen leads to a system of linear equations, which permits the calculation of the molar fractions of the nine gas phase components.

$$4 \cdot \Delta\dot{n}_{Bu} + \Delta\dot{n}_{CO} + \Delta\dot{n}_{CO_2} + 4 \cdot \Delta\dot{n}_{MA} + 2 \cdot \Delta\dot{n}_{AcA} + 3 \cdot \Delta\dot{n}_{AcrA} = 0 \qquad \text{(A-5)}$$

$$10 \cdot \Delta\dot{n}_{Bu} + 2 \cdot \Delta\dot{n}_{H_2O} + 2 \cdot \Delta\dot{n}_{MA} + 4 \cdot \Delta\dot{n}_{AcA} + 4 \cdot \Delta\dot{n}_{AcrA} = 0 \qquad \text{(A-6)}$$

$$2 \cdot \Delta\dot{n}_{O_2} + \Delta\dot{n}_{CO} + 2 \cdot \Delta\dot{n}_{CO_2} + \Delta\dot{n}_{H_2O} + 3 \cdot \Delta\dot{n}_{MA} + 2 \cdot \Delta\dot{n}_{AcA} + 2 \cdot \Delta\dot{n}_{AcrA} = 0 \qquad \text{(A-7)}$$

$$\Delta\dot{n}_{N_2} = 0 \qquad \text{(A-8)}$$

A.2 Reactor models

A.2.1 Bench reactor model

The reactor model is one-dimensional and heterogeneous, accounting for intra particle diffusion as well as for axial dispersion. It is deduced for cylindrical and ring shaped catalyst pellets. In order to derive the balance equations, an infinitesimal volume element is considered (Fig. 62). The mass, molar, and heat fluxes that enter and leave this element are given in kg/m²/s, mol/m²/s and J/m²/s.

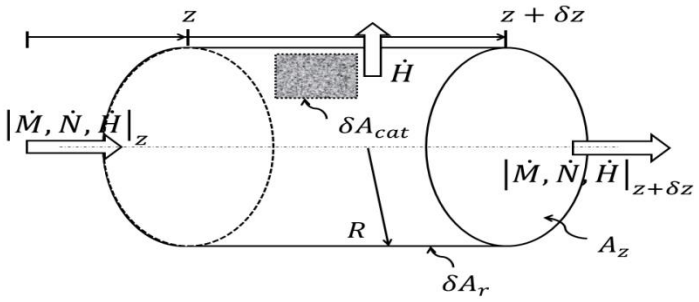

Fig. 62: Control volume for the one-dimensional heterogeneous reactor model.

- **Overall mass balance gas phase:**

$$\left(\dot{M} \cdot A_z\right)|_z - \left(\dot{M} \cdot A_z\right)|_{z+\delta z} = 0 \qquad \text{(A-9)}$$

The mass flux may be expressed by the product of fluid density and flow velocity. For its value at position $z + \delta z$, the first term of a Taylor series is used. As the axial section area A_z is constant, it can be reduced directly.

$$\dot{M}|_{z+\delta z} = \dot{M}|_z + \frac{\partial}{\partial z}\left(\dot{M}\right)dz \qquad \text{(A-10)}$$

Replacing $\dot{M}$ and transposing results in

$$\frac{\partial}{\partial z}\left(\rho_{fl} \cdot u_z\right) = 0 \qquad \text{(A-11)}$$

- **Material balance fluid:**

The molar fluxes that enter and leave the gas phase volume element are of convection ($\dot{N}_{i,z}^{f,conv}$) and dispersion ($\dot{N}_{i,z}^{f,disp}$). Additionally, a flux, $\dot{N}_i^{sf}$, enters the balance volume from the solid surface. For the steady state, the accumulation term is zero.

$$\left(\dot{N}_{i,z}^{f,conv} \cdot A_z\right)|_z - \left(\dot{N}_{i,z}^{f,conv} \cdot A_z\right)|_{z+\delta z} + \left(\dot{N}_{i,z}^{f,disp} \cdot A_z\right)|_z - \left(\dot{N}_{i,z}^{f,disp} \cdot A_z\right)|_{z+\delta z} + \dot{N}_i^{sf} \cdot \delta A_P = 0 \quad \text{(A-12)}$$

δA_P may be expressed as the product of the specific surface area of the catalyst in the reactor, a_P, and the differential volume. Applying again a Taylor series, the material balance simplifies to

$$\frac{\partial}{\partial z}\left(\dot{N}_{i,z}^{f,conv} + \dot{N}_{i,z}^{f,disp}\right) - a_p \cdot \dot{N}_i^{sf} = 0 \quad \text{(A-13)}$$

- **Material balance solid:**

The catalyst pellet is considered one-dimensionally in direction of the particle radius. Balancing the molar flows gives

$$\left(\dot{N}_i^s \cdot A_{r_p}\right)|_{r_p} - \left(\dot{N}_i^s \cdot A_{r_p}\right)|_{r_p+\delta r_p} + \sum_j \nu_{i,j} \cdot r_j \cdot \rho_P \cdot \delta V_P = 0 \quad \text{(A-14)}$$

The diffusion area, A_{r_p}, changes with the particle radius, r_p, and the Taylor series for a cylindrical particle shape ($\delta A_{r_p} = 2\pi h_P \delta r_p$, $\delta V_P = 2\pi h_P r_p \delta r_p$) results in

$$\left(\dot{N}_i^s \cdot A_{r_p}\right)|_{r_p+\delta r_p} = \left(\dot{N}_i^s \cdot A_{r_p}\right)|_{r_p} + \frac{\partial}{\partial r_p}\left(\dot{N}_i^s \cdot A_{r_p}\right) \cdot dr_p$$

$$= 2\pi h_P \cdot \left(r_p \cdot \dot{N}_i^s + r_p \cdot \frac{\partial \dot{N}_i^s}{\partial r_p} dr_p + \dot{N}_i^s \cdot dr_p\right) \quad \text{(A-15)}$$

Doing the same for spherical particles and replacing the general molar balance results in

$$-\frac{\partial \dot{N}_i^s}{\partial r_p} - \frac{\varphi_{geo}}{r_p} \cdot \dot{N}_i^s + \sum_j \nu_{i,j} \cdot r_j \cdot \rho_p = 0 \quad \text{(A-16)}$$

- **Energy balance gas-phase:**

The heat fluxes $\dot{H}^j$ (mol/m²/s) are defined as the sum of all molar fluxes that enter and leave the control volume multiplied with their partial enthalpy. Additionally, the heat exchange with the solid phase and with the reactor wall, as well as the axial heat conduction are taken into account. These heat fluxes are termed $\dot{Q}^j$.

$$\dot{H} = \sum_i \dot{N}_i \cdot h_i = \sum_i \dot{N}_i \cdot \left(\Delta_F H_i^* + \int c_{p,i} dT\right) \quad \text{(A-17)}$$

$$\left(\dot{H}^{f,conv} \cdot A_z\right)|_z - \left(\dot{H}^{f,conv} \cdot A_z\right)|_{z+\delta z} + \left(\dot{H}^{f,disp} \cdot A_z\right)|_z - \left(\dot{H}^{f,disp} \cdot A_z\right)|_{z+\delta z} + \left(\dot{Q}^{f,cond} \cdot A_z\right)|_z - \left(\dot{Q}^{f,cond} \cdot A_z\right)|_{z+\delta z} + \left(\dot{H}^{sf} + \dot{Q}^{sf}\right) \cdot \delta A_P - \dot{Q}^w \cdot \delta A_w = 0 \quad \text{(A-18)}$$

Applying a Taylor series and expressions for δA_P and δA_w, the material balance simplifies to

$$-\frac{\partial}{\partial z}\left(\dot{H}^{f,conv} + \dot{H}^{f,disp} + \dot{Q}^{f,cond}\right) + a_p \cdot \left(\dot{H}^{sf} + \dot{Q}^{sf}\right) - \frac{2}{R_T} \cdot \dot{Q}^w = 0 \quad \text{(A-19)}$$

- **Energy balance catalyst pellet:**

Balancing the heat flows gives

$$\left(\dot{H}^s \cdot A_{r_p}\right)|_{r_p} - \left(\dot{H}^s \cdot A_{r_p}\right)|_{r_p+\delta r_p} + \left(\dot{Q}^s \cdot A_{r_p}\right)|_{r_p} - \left(\dot{Q}^s \cdot A_{r_p}\right)|_{r_p+\delta r_p} = 0 \quad \text{(A-20)}$$

and further

$$\frac{1}{r_p}\frac{\partial}{\partial r_p}\left(r_p \cdot \dot{H}^s\right) + \frac{1}{r_p}\frac{\partial}{\partial r_p}\left(r_p \cdot \dot{Q}^s\right) = 0 \quad \text{(A-21)}$$

As $\dot{H}^S = \sum_i \dot{N}_i^S \cdot h_i$, the material balance can be introduced resulting in

$$\frac{1}{r_p}\frac{\partial}{\partial r_p}\left(r_p \cdot \dot{Q}^S\right) + \frac{1}{r_p}\frac{\partial}{\partial r_p}\left(r_p \cdot \sum_i \dot{N}_i^S \cdot \int c_{p,i} dT\right) + \sum_i \sum_j \nu_{i,j} \cdot r_j \cdot \rho_p \cdot \Delta_F H_i^* = 0 \qquad \text{(A-22)}$$

A.2.2 Pilot reactor model

The model for the pilot reactor is heterogeneous and two-dimensional accounting for radial heat and mass transport. As the flow rates are much higher than in the bench scale reactor, axial dispersion and heat conduction are neglected. The model is deduced for ring shaped pellets. Hence, a ring shaped control volume is considered (Fig. 63) in order to derive the balance equations.

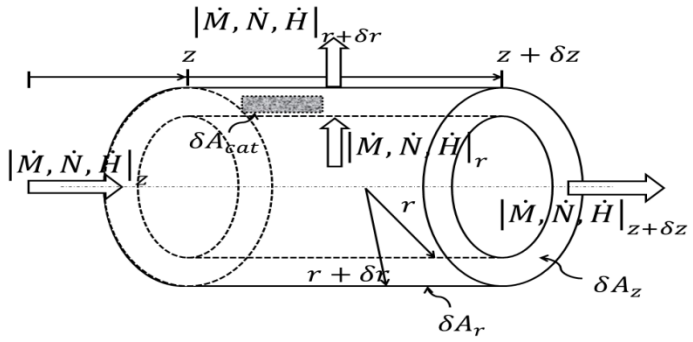

Fig. 63: Control volume for the two-dimensional reactor model.

- **Overall mass balance gas phase:**

Due to radial dispersion there is a radial mass flux passing the control volume.

$$\left(\dot{M}_z \cdot A_z\right)|_z - \left(\dot{M}_z \cdot A_z\right)|_{z+\delta z} + \left(\dot{M}_r \cdot A_r\right)|_r - \left(\dot{M}_r \cdot A_r\right)|_{r+\delta r} = 0 \qquad \text{(A-23)}$$

With the radial section area, A_r, with r being the reactor radius, the application of a Taylor series gives

$$\left(\dot{M}_r \cdot A_r\right)|_{r+\delta r} = \left(\dot{M}_r \cdot A_r\right)|_r + \frac{\partial}{\partial r}\left(\dot{M} \cdot 2\pi r \delta z\right) dr \qquad \text{(A-24)}$$

and the mass balance is finally

$$\frac{\partial}{\partial z}\left(\rho_{fl}\cdot u_z\right)+\frac{1}{r}\frac{\partial}{\partial r}\left(r\cdot\rho_{fl}\cdot u_r\right)=0 \tag{A-25}$$

- **Material balance fluid:**

Axial and radial molar fluxes enter and leave the gas phase volume element whereas the axial flux, $\dot{N}_{i,z}^{f}$, is convective and the radial flux, $\dot{N}_{r,i}^{f}$, includes the radial dispersion. An additional flux, $\dot{N}_{i}^{sf}$, describes the material exchange between solid surface and fluid. In this case, also the molar accumulation is considered.

$$\left(\dot{N}_{i,z}^{f}\cdot A_z\right)|_z-\left(\dot{N}_{i,z}^{f}\cdot A_z\right)|_{z+\delta z}+\left(\dot{N}_{i,r}^{f}\cdot A_r\right)|_r-\left(\dot{N}_{i,r}^{f}\cdot A_r\right)|_{r+\delta r}+\dot{N}_{i}^{sf}\cdot\delta A_P=\frac{\partial n_i^f}{\partial t} \tag{A-26}$$

Applying again the Taylor series the final model equation is

$$-\varepsilon_B\cdot c_{fl}^{f}\cdot\frac{\partial x_i^f}{\partial t}=\frac{\partial\dot{N}_{i,z}^{f}}{\partial z}+\frac{1}{r}\frac{\partial}{\partial r}\left(r\cdot\dot{N}_{i,r}^{f}\right)-a_P\cdot\dot{N}_{i}^{sf} \tag{A-27}$$

- **Material balance solid:**

As in the one-dimensional reactor model, the catalyst pellet is cylindrical and one-dimensional the mass balance is analogously written.

$$-\frac{1}{r_p}\frac{\partial}{\partial r_p}\left(r_p\cdot\dot{N}_{i}^{s}\right)+\sum_j\nu_{i,j}\cdot r_{het,j}\cdot\rho_{cat}=\varepsilon_{cat}\cdot c_{fluid}^{s}\cdot\frac{\partial x_i^s}{\partial t} \tag{A-28}$$

- **Energy balance fluid:**

In this case only radial heat conduction is taken into account. Because of the much lower heat capacity of the gas comparing to the solid, the time derivative of the gas temperature may be neglected. From the general balance

$$\left(\dot{H}_z^f \cdot A_z\right)|_z - \left(\dot{H}_z^f \cdot A_z\right)|_{z+\delta z} + \left(\dot{H}_r^f \cdot A_r\right)|_r - \left(\dot{H}_r^f \cdot A_r\right)|_{r+\delta r} + \left(\dot{Q}_r^f \cdot A_r\right)|_r$$
$$-\left(\dot{Q}_r^f \cdot A_r\right)|_{r+\delta r} + \left(\dot{H}^{sf} + \dot{Q}^{sf}\right) \cdot \delta A_P = \frac{\partial H^f}{\partial t} \quad \text{(A-29)}$$

results

$$\frac{\partial H^f}{\partial t} = \frac{\partial \dot{H}_z^f}{\partial z} + \frac{1}{r}\frac{\partial}{\partial r}\left(r \cdot \dot{H}_r^f\right) + \frac{1}{r}\frac{\partial}{\partial r}\left(r \cdot \dot{Q}_r^f\right) - a_P \cdot \left(\dot{H}^{sf} + \dot{Q}^{sf}\right) \quad \text{(A-30)}$$

- **Energy balance solid:**

Accounting for storage, the general balance is

$$\left(\dot{H}^s \cdot A_{r_p}\right)|_{r_p} - \left(\dot{H}^s \cdot A_{r_p}\right)|_{r_p+\delta r_p} + \left(\dot{Q}^s \cdot A_{r_p}\right)|_{r_p} - \left(\dot{Q}^s \cdot A_{r_p}\right)|_{r_p+\delta r_p}$$
$$= \delta m_P \cdot c_{p,P} \cdot \frac{\partial T^s}{\partial t} \quad \text{(A-31)}$$

and further

$$-\rho_P \cdot c_{p,P} \cdot \frac{\partial T^s}{\partial t} = \frac{1}{r_p}\frac{\partial}{\partial r_p}\left[r_p \cdot \left(\dot{Q}^s + \dot{H}^s\right)\right] + \sum_i \sum_j \nu_{i,j} \cdot r_j^0 \cdot a_k(t) \cdot \rho_P \cdot \Delta_F H_i^* \quad \text{(A-32)}$$

- **Energy and material balance of the solid surface (boundary conditions solid):**

The balances for the catalyst surface are deduced for rings and must imply the dynamic terms for concentration and temperature too. The general balances are

$$\dot{Q}^s \cdot \delta A_P - \dot{Q}^{sf} \cdot \delta A_P + \left(\dot{Q}_r^{ss} \cdot A_r\right)|_r - \left(\dot{Q}_r^{ss} \cdot A_r\right)|_{r+\delta r} = \delta m_P \cdot c_{p,P} \cdot \frac{\partial T^{sf}}{\partial t} \quad \text{(A-33)}$$

$$\dot{N}_i^s \cdot \delta A_P - \dot{N}_i^{sf} \cdot \delta A_P = \frac{\partial n_i^{surf}}{\partial t} = \varepsilon_P \cdot c_{fl}^{sf} \cdot \frac{\partial x_i^{surf}}{\partial t} \cdot \delta V_P \quad \text{(A-34)}$$

The radial heat transport in the reactor through the solid is determined by the effective radial conductivity of the bed, λ_r^{ss}. As the surface temperature is assumed to be uniform, only one boundary condition is needed for the heat balance.

$$a_P \cdot \dot{Q}^s + a_P \cdot \dot{Q}^{sf} - \frac{1}{r}\frac{\partial}{\partial r}\left(r \cdot \dot{Q}_r^{ss}\right) = \frac{\rho_P \cdot c_{p,P}}{S_v} \cdot \frac{\partial T^{sf}}{\partial t} \quad \text{(A-35)}$$

For the material balance, the inner and outer surface concentration have to be considered separately.

$r_p = R_{P,outer}$:

$$\frac{\varepsilon_p}{S_v} \cdot c_{fl}^{osf} \cdot \frac{\partial x_i^{osf}}{\partial t} = c_{fl}^{s} \cdot \mathcal{D}_i^{s,eff} \cdot \frac{\partial x_i^{osf}}{\partial r_p} + \beta_i \cdot c_{fl}^{f} \cdot \left(x_i^{osf} - x_i^{f}\right) \quad \text{(A-36)}$$

$r_p = R_{P,inner}$:

$$\frac{\varepsilon_p}{S_v} \cdot c_{fl}^{isf} \cdot \frac{\partial x_i^{isf}}{\partial t} = c_{fl}^{s} \cdot \mathcal{D}_i^{s,eff} \cdot \frac{\partial x_i^{isf}}{\partial r_p} - \beta_i \cdot c_{fl}^{f} \cdot \left(x_i^{isf} - x_i^{f}\right) \quad \text{(A-37)}$$

- **Energy balance reactor wall:**

The wall conducts the heat fluxes coming from fluid and solid to the coolant. Beside the radial heat transfer to the coolant, axial heat conduction is considered. Thus, the wall is modeled two-dimensionally. The general balance on a ring shaped control volume is

$$\dot{Q}_{r_w}^{w} A_{r_w}|_{rw} - \dot{Q}_r^{w} A_{r_w}|_{r_w+\delta r_w} + \dot{Q}_z^{w} A_{z_w}|_z - \dot{Q}_z^{w} A_z|_{z+\delta z} = \rho_W \cdot c_{p,W} \cdot \frac{\partial T^w}{\partial t} \cdot \delta V_W \quad \text{(A-38)}$$

and further

$$\rho_W \cdot c_{p,W} \cdot \frac{\partial T^w}{\partial t} = -\frac{1}{r_w}\frac{\partial}{\partial r_w}\left(r_w \cdot \dot{Q}_r^{w}\right) - \frac{\partial \dot{Q}_z^{w}}{\partial z} \quad \text{(A-39)}$$

A.3 Mass and heat transport coefficients

A.3.1 Mass and heat transfer through the solid-fluid-interface

The correlations of Gnielinski [57] are used for the calculation of the solid-fluid heat and material transfer coefficients. The shape factor f_a is 1.6 for full cylinders and 2.1 for ring shapes.

$$Sh = \frac{\beta \cdot d_{surf}}{\mathcal{D}} = f_a \left(2 + \sqrt{Sh_{lam}^2 + Sh_{turb}^2} \right) \quad \text{(A-40)}$$

$$Sh_{lam} = 0.664 \cdot \sqrt{Re_\varepsilon} \cdot \sqrt[3]{Sc} \quad \text{(A-41)}$$

$$Sh_{turb} = \frac{0.037 \cdot Re_\varepsilon^{0.8} \cdot Sc}{1 + 2.443 \cdot Re_\varepsilon^{-0.1} \cdot \left(Sc^{2/3} - 1 \right)} \quad \text{(A-42)}$$

$$Nu = \frac{\alpha_P \cdot d_{surf}}{\lambda_{fl}} = f_a \left(2 + \sqrt{Nu_{lam}^2 + Nu_{turb}^2} \right) \quad \text{(A-43)}$$

$$Nu_{lam} = 0.664 \cdot \sqrt{Re_\varepsilon} \cdot \sqrt[3]{Pr} \quad \text{(A-44)}$$

$$Nu_{turb} = \frac{0.037 \cdot Re_\varepsilon^{0.8} \cdot Pr}{1 + 2.443 \cdot Re_\varepsilon^{-0.1} \cdot \left(Pr^{2/3} - 1 \right)} \quad \text{(A-45)}$$

$$Re_\varepsilon = \frac{u_z \cdot \rho_{fl} \cdot d_{surf}}{\eta_{fl} \cdot \varepsilon_B} \quad \text{(A-46)}$$

$$Sc = \frac{\eta_{fl}}{\mathcal{D} \cdot \rho_{fl}} \quad \text{(A-47)}$$

$$Pr = \frac{\eta_{fl} \cdot c_{p,fl} \cdot}{\lambda_{fl}} \quad \text{(A-48)}$$

A.3.2 Axial and radial dispersion

The calculation of the axial and radial dispersion coefficient is based on the correlations found in [56,94].

$$Pe_n = \frac{u_z \cdot d_{vol}}{\mathcal{D}_n} = \left(\frac{\mathcal{D}_B / \mathcal{D}}{Pe_0} + \frac{1}{K_n} \right)^{-1} \qquad \text{n = ax, r} \quad \text{(A-49)}$$

$$\frac{\mathcal{D}_B}{\mathcal{D}} = 1 - \sqrt{1 - \varepsilon_B} \quad \text{(A-50)}$$

$$Pe_0 = \frac{u_z \cdot d_{vol}}{\mathcal{D}_{mix}} \quad \text{(A-51)}$$

$$K_{ax} = 2 \tag{A-52}$$

For Raschig rings with the dimensions $d_a \times d_i \times h,$, K_r is calculated as

$$K_r = K_{r,\infty} \cdot \left[2 - \left(1 - \frac{2}{d_T/d_P}\right)^2\right] \tag{A-53}$$

$$K_{r,\infty} = 8 \cdot \left[1.75 \cdot \Delta\Psi_1 + 3.46 \cdot (h - \Delta\Psi_1) \cdot \left(\frac{d_i}{d_a}\right)^{2/3}\right]^{-1} \tag{A-54}$$

$$\Delta\Psi_1 = \left[1 + \frac{1-\Psi_1}{\Psi_1} \cdot \left(\frac{d_i}{d_a}\right)^2\right]^{-1} \tag{A-55}$$

$$\Psi_1 = 0.39 + 0.02 \cdot \left[\frac{1}{d_a} - 0.85\right]^{4/3} \tag{A-56}$$

A.3.3 Radial heat transfer

The effective radial bed conductivity according to the model of Zehner-Bauer-Schlünder [56,94] includes the contributions of solid and fluid phase without flow, as well as the contribution of the fluid flow.

$$\frac{\lambda_r^{eff}}{\lambda_{fl}} = \frac{\lambda_{r,0}^{f}}{\lambda_{fl}} + \frac{\lambda_{r,0}^{ss}}{\lambda_{fl}} + \frac{Pe_0}{K_r} \tag{A-57}$$

$$\frac{\lambda_{r,0}^{f}}{\lambda_{fl}} = \left(1 - \sqrt{1-\varepsilon_B}\right) \cdot \varepsilon_B \cdot \left[(\varepsilon_B - 1 + \kappa_G^{-1})^{-1} + \kappa_{rad}\right] \tag{A-58}$$

$$\frac{\lambda_{r,0}^{ss}}{\lambda_{fl}} = \sqrt{1-\varepsilon_B} \cdot \left[\varphi \cdot \kappa_p + (1-\varphi) \cdot \kappa_c\right] \tag{A-59}$$

$$\kappa_c = \frac{2}{N}\left\{\frac{B\cdot(\kappa_p+\kappa_{rad}-1)}{N^2\cdot\kappa_p\cdot\kappa_G} ln \frac{\kappa_p+\kappa_{rad}}{B\cdot\left[\kappa_G+(1-\kappa_G)\cdot(\kappa_p+\kappa_{rad})\right]} + \frac{B+1}{2\cdot B}\left[\frac{\kappa_{rad}}{\kappa_G} - B\cdot\left(1+\frac{1-\kappa_G}{\kappa_G}\cdot\kappa_{rad}\right)\right] - \frac{B-1}{N\cdot\kappa_G}\right\} \tag{A-60}$$

$$N = \frac{1}{\kappa_G} \cdot \left(1 + \frac{\kappa_{rad} - B\cdot\kappa_G}{\kappa_p}\right) - B \cdot \left(\frac{1}{\kappa_G} - 1\right) \cdot \left(1 + \frac{\kappa_{rad}}{\kappa_p}\right) \tag{A-61}$$

$$B = C_f \cdot \left(\frac{1-\varepsilon_B}{\varepsilon_B}\right)^{10/9} \tag{A-62}$$

$$C_f = 2.5 \cdot \left[1 + \left(\frac{d_i}{d_a}\right)^2\right] \tag{A-63}$$

$$\kappa_{rad} = \frac{\lambda_{rad}}{\lambda_{fl}} = \frac{4 \cdot \sigma_{rad}}{{}^{2}/_{\varepsilon_{rad}} - 1} \cdot T^3 \cdot \frac{d_{vol}}{\lambda_{fl}} \tag{A-64}$$

$$\kappa_G = \frac{\lambda_G}{\lambda_{fl}} = \left(1 + \frac{l}{d_{vol}}\right)^{-1} \tag{A-65}$$

$$l = 2 \cdot \frac{2-\mu}{\mu} \cdot \sqrt{\frac{2 \cdot \pi \cdot R \cdot T}{M_i}} \cdot \frac{\lambda_{fl}}{p \cdot \left(2 \cdot c_{p,fl} - {}^{R}/_{M_i}\right)} \tag{A-66}$$

$$log\left(\frac{1}{\mu} - 1\right) = 0.6 - \frac{{}^{1000\mathrm{K}}/_{T} + 1}{2.8} \tag{A-67}$$

The bed-wall heat transfer coefficient, α_w, is calculated according to the correlation of Nilles and Martin [56].

$$Nu^w = \frac{\alpha_w \cdot d_P}{\lambda^f} = \left(1.3 + \frac{5}{d_T/d_P}\right) \cdot \frac{\lambda_{r,0}}{\lambda^f} + 0.19 \cdot Re_0^{0.75} \cdot Pr^{1/3} \tag{A-68}$$

A.3.4 Intra-particle diffusion

The intra-particle diffusion is described by an Fickian approach with an effective diffusion coefficient according to [15,55]:

$$\mathcal{D}_i^{eff} = \left(\frac{1}{\mathcal{D}_{i,mix}} + \frac{1}{\mathcal{D}_{K,i}}\right)^{-1} \cdot \frac{\varepsilon_p}{\tau} \tag{A-69}$$

$$\mathcal{D}_{i,mix} = \frac{1 - x_i}{\sum_{j \neq i} {}^{x_j}/_{\mathcal{D}_{i,j}}} \tag{A-70}$$

$$\mathcal{D}_{i,j} = \frac{0{,}0143 \cdot T^{1{,}75} \cdot \sqrt{{M_i}^{-1} + {M_j}^{-1}}}{p \cdot \sqrt{2} \cdot \left[{\Delta_{vi}}^{1/3} + {\Delta_{vj}}^{1/3}\right]^2} \tag{A-71}$$

$$\mathcal{D}_{K,i} = \frac{d_{Pore}}{3} \cdot \sqrt{\frac{8 \cdot R \cdot T}{\pi \cdot M_i}} \tag{A-72}$$

A.4 Kinetic models

This section describes the deduction of the intrinsic kinetic models.

- ***HW1*-model:**

The *HW1*-model implies the following assumptions:

- Gas-phase hydrocarbon reacts with chemisorbed oxygen
- The reoxidation of the active site is inhibited by adsorbed *n*-butane and water
- The activation of the hydrocarbon is rate determining
- No adsorptive interaction between MA, CO and CO2 with the catalyst surface

The reactions are

$$\mathrm{S_{red}} + 0.5\mathrm{O_2} \overset{K_{ox}}{\Longleftrightarrow} \mathrm{S_{ox}} \qquad \text{(A-i)}$$

$$\mathrm{S_{red}} + \mathrm{Bu} \overset{K_{Bu}}{\Longleftrightarrow} \mathrm{S_{Bu}} \qquad \text{(A-ii)}$$

$$\mathrm{S_{red}} + \mathrm{H_2O} \overset{K_{H_2O}}{\Longleftrightarrow} \mathrm{S_{H_2O}} \qquad \text{(A-iii)}$$

$$\mathrm{A}_i + \mathrm{S_{ox}} \overset{k^*_{i,j}}{\longrightarrow} \mathrm{A}_j \qquad i = \mathrm{Bu, MA}\ ;\ j = \mathrm{MA, CO, CO_2};\ i \neq j \qquad \text{(A-iv)}$$

Balancing the surface sites and applying the concept of the rate determining step gives

$$r_{i,j} = \frac{k^*_{i,j} \cdot K_{ox} \cdot p_i \cdot p_{O_2}^{0.5}}{1 + K_{Bu,1} \cdot p_{Bu} + K_{H_2O} \cdot p_{H_2O} + K_{ox} \cdot p_{O_2}^{0.5}} \qquad i = \mathrm{Bu, MA}\ ;\ j = \mathrm{MA, CO, CO_2};\ i \neq j \qquad \text{(A-73)}$$

Uihlein [] found that the surface coverage of oxygen is small as compared to the surface concentrations of *n*-butane and water ($K_{ox} \cdot p_{O_2}^{0.5} \ll K_{Bu} \cdot p_{Bu} + K_{Bu} \cdot p_{Bu}$), which leads to the final rate equations:

$$r_{i,j} = \frac{k_{i,j} \cdot p_i \cdot p_{O_2}^{0.5}}{1 + K_{Bu,1} \cdot p_{Bu} + K_{H_2O} \cdot p_{H_2O}} \qquad i = \mathrm{Bu, MA}\ ;\ j = \mathrm{MA, CO, CO_2};\ i \neq j \qquad \text{(A-74)}$$

- ***HW2-model:***

The *HW2*-model includes the same assumptions as the *HW1*-model with the only difference that the formation of CO from *n*-butane is performed by the reaction of adsorbed *n*-butane and oxygen:

$$A_i + S_{ox} \xrightarrow{k^*_{i,j}} A_j$$ *i* = Bu, MA; *j* = MA, CO_2; $i \neq j$ (A-v)

$$S_{Bu} + S_{ox} \xrightarrow{k^*_{Bu,CO}} CO$$ (A-vi)

$$MA + S_{ox} \xrightarrow{k^*_{MA,CO}} CO$$ (A-vii)

$$r_{i,j} = \frac{k_{i,j} \cdot p_i \cdot p_{O_2}^{0.5}}{1 + K_{Bu,1} \cdot p_{Bu} + K_{H_2O} \cdot p_{H_2O}}$$ *i* = Bu, MA; *j* = MA, CO_2; $i \neq j$ (A-75)

$$r_{Bu,CO} = \frac{k_{Bu,CO} \cdot p_{Bu} \cdot p_{O_2}^{0.5}}{\left(1 + K_{Bu,1} \cdot p_{Bu} + K_{H_2O} \cdot p_{H_2O}\right)^2}$$ (A-76)

$$r_{MA,CO} = \frac{k_{MA,CO} \cdot p_{MA} \cdot p_{O_2}^{0.5}}{1 + K_{Bu,1} \cdot p_{Bu} + K_{H_2O} \cdot p_{H_2O}}$$ (A-77)

- ***HW3*-model:**

The *HW3*-model is based on the same mechanistic steps as the *HW1*-model. The only difference is that the conversion of *n*-butane to CO occurs on a different active site as compared to the other reactions. The oxidation of both active sites is equally inhibited by water

$$S_{red,1} + 0.5O_2 \overset{K_{ox,1}}{\Longleftrightarrow} S_{ox,1}$$ (A-viii)

$$S_{red,2} + 0.5O_2 \overset{K_{ox,2}}{\Longleftrightarrow} S_{ox,2}$$ (A-ix)

$$S_{red,1} + Bu \overset{K_{Bu,1}}{\Longleftrightarrow} S_{Bu,1}$$ (A-x)

$$S_{red,2} + Bu \overset{K_{Bu,2}}{\Longleftrightarrow} S_{Bu,2}$$ (A-xi)

$$S_{red,k} + H_2O \overset{K_{H_2O}}{\Longleftrightarrow} S_{H_2O,k}$$ k = 1, 2 (A-xii)

$$A_i + S_{ox,1} \xrightarrow{k^*_{i,j}} A_j$$ i = Bu, MA ; j = MA, CO_2; $i \neq j$ (A-xiii)

$$Bu + S_{ox,2} \xrightarrow{k^*_{Bu,CO}} CO$$ (A-xiv)

$$MA + S_{ox,1} \xrightarrow{k^*_{MA,CO}} CO$$ (A-xv)

Balancing the two types of surface sites separately and applying again the concept of the rate determining step for the reaction gives:

$$r_{i,j} = \frac{k_{i,j} \cdot p_i \cdot p_{O_2}^{0.5}}{1 + K_{Bu,1} \cdot p_{Bu} + K_{H_2O} \cdot p_{H_2O}} \qquad i = \text{Bu, MA};\ \ j = \text{MA, CO}_2;\ \ i \neq j \qquad \text{(A-78)}$$

$$r_{i,j} = \frac{k_{i,j} \cdot p_i \cdot p_{O_2}^{0.5}}{1 + K_{Bu,2} \cdot p_{Bu} + K_{H_2O} \cdot p_{H_2O}} \qquad i = \text{Bu, MA};\ \ j = \text{CO} \qquad \text{(A-79)}$$

- ***RO*-model:**

The *RO*-model implies the following assumptions:

- The oxidation of a reduced site can lead to two different oxidized sites, one of which produces CO and the other MA and CO_2 by reaction with gas-phase hydrocarbon
- The reoxidation of the active site is inhibited by adsorbed water
- The concept of the quasi-steady state applies for the oxidized sites
- No adsorptive interaction between MA, CO and CO_2 with the catalyst surface

The reactions are

$$\mathrm{S_{red}} + 0.5\mathrm{O_2} \xrightarrow{k_{ox,1}} \mathrm{S_{ox,1}} \qquad \text{(A-xvi)}$$

$$\mathrm{S_{red}} + 0.5\mathrm{O_2} \xrightarrow{k_{ox,2}} \mathrm{S_{ox,2}} \qquad \text{(A-xvii)}$$

$$\mathrm{S_{red}} + \mathrm{H_2O} \overset{K_{H_2O}}{\Longleftrightarrow} \mathrm{S_{H_2O}} \qquad \text{(A-xviii)}$$

$$\mathrm{A}_i + \mathrm{S_{ox,1}} \xrightarrow{k^*_{i,j}} \mathrm{A}_j \qquad i = \text{Bu, MA};\ j = \text{MA, CO}_2;\ i \neq j \qquad \text{(A-xix)}$$

$$\mathrm{A}_i + \mathrm{S_{ox,2}} \xrightarrow{k^*_{i,j}} \mathrm{A}_j \qquad i = \text{Bu, MA};\ j = \text{CO} \qquad \text{(A-xx)}$$

Applying steady state assumption for the two oxidized sites and balancing the surface sites gives

$$r_{i,j} = \frac{k_{i,j} \cdot k_{ox,1} \cdot p_i \cdot p_{O_2}^{0.5}}{\left(k_{ox,1} + k_{ox,2} \cdot \frac{\sum_{i,j \neq CO} k_{i,j} \cdot p_i}{\sum_{i,j=CO} k_{i,j} \cdot p_i}\right) + \sum_{i,j \neq CO} k_{i,j} \cdot p_i \cdot \left(1 + K_{H_2O} \cdot p_{H_2O}\right)}$$

$i = \text{Bu, MA};\ \ j = \text{MA, CO}_2;\ \ i \neq j \qquad \text{(A-80)}$

$$r_{i,j} = \frac{k_{i,j} \cdot k_{ox,2} \cdot p_i \cdot p_{O_2}^{0.5}}{\left(k_{ox,2} + k_{ox,1} \cdot \frac{\sum_{i,j=CO} k_{i,j} \cdot p_i}{\sum_{i,j\neq CO} k_{i,j} \cdot p_i}\right) + \sum_{i,j=CO} k_{i,j} \cdot p_i \cdot \left(1 + K_{H_2O} \cdot p_{H_2O}\right)}$$

i = Bu, MA; *j* = CO (A-81)

Assuming that both types of oxidized sites exist in equal quantities on the catalyst surface under reacting conditions ($\frac{\theta_2}{\theta_1} = \frac{k_{ox,2}}{k_{ox,1}} \cdot \frac{\sum_{i,j\neq CO} k_{i,j} \cdot p_i}{\sum_{i,j=CO} k_{i,j} \cdot p_i}$ = 1) and that the rates of MA conversion are small as compared to the conversion of *n*-butane ($\sum_{Bu} k_{Bu,j} \cdot p_{Bu} \gg k_{MA,j} \cdot p_{MA}$), the final rate equations are

$$r_{i,j} = \frac{k_{i,j} \cdot p_i}{2 + K_{Bu,1} \frac{p_{Bu}}{p_{O_2}^{0.5}} \cdot \left(1 + K_{H_2O} \cdot p_{H_2O}\right)}$$

i = Bu, MA; *j* = MA, CO_2 ; $i \neq j$ (A-82)

$$r_{i,j} = \frac{k_{i,j} \cdot p_i}{2 + K_{Bu,2} \frac{p_{Bu}}{p_{O_2}^{0.5}} \cdot \left(1 + K_{H_2O} \cdot p_{H_2O}\right)}$$

i = Bu, MA ; *j* = CO (A-83)

A.5 Parameter estimations for other kinetic models

The following tables show the results of the parameter estimations applying the three other proposed kinetic models *HW1*, *HW2* and *RO*. Additionally the respective CO/CO_2-conversion plots are shown as this was one of the main selection criteria.

- ***HW1*-model:**

Tab. 18: Parameter estimation results for the *HW1* model

	Parameter	Unit	Optimal Estimate	Confidence Interval (95%)
1	$E^A_{Bu,MA}$	kJ/mol	99.3	7
2	$E^A_{Bu,CO}$	kJ/mol	124.1	9
3	E^A_{Bu,CO_2}	kJ/mol	125.5	13
4	$E^A_{MA,CO}$	kJ/mol	173.8	34
5	E^A_{MA,CO_2}	kJ/mol	137.0	37
6	K_{H_2O}	bar^{-1}	69.5	16
7	$K_{Bu,1}$	bar^{-1}	481.7	97
8	$k^{ref}_{Bu,MA}$	10^{-3} mol/s/kg/$bar^{1.5}$	695.6	130
9	$k^{ref}_{Bu,CO}$	10^{-3} mol/s/kg/$bar^{1.5}$	150.6	27
10	k^{ref}_{Bu,CO_2}	10^{-3} mol/s/kg/$bar^{1.5}$	84.6	16
11	$k^{ref}_{MA,CO}$	10^{-3} mol/s/kg/$bar^{1.5}$	12.9	4
12	k^{ref}_{MA,CO_2}	10^{-3} mol/s/kg/$bar^{1.5}$	12.8	3
13	τ	-	4.2	0.3

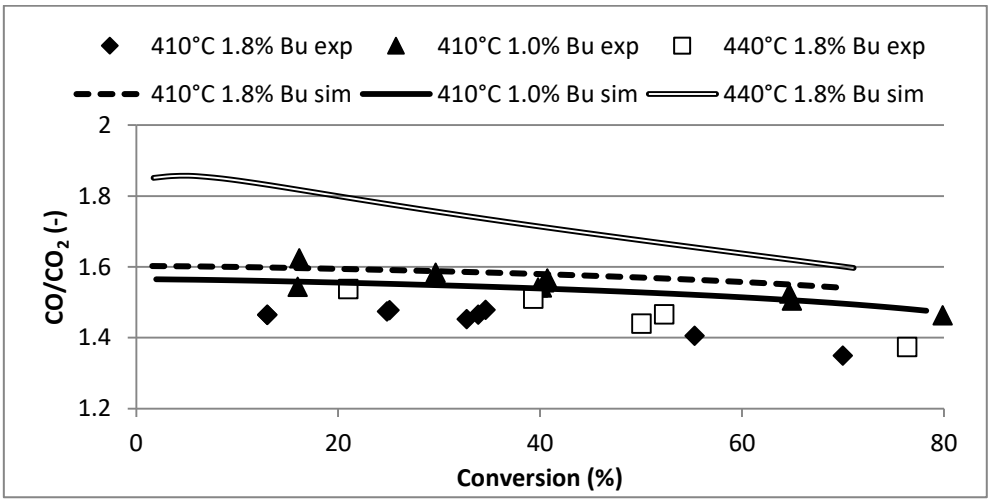

Fig. 64: Measured and simulated CO/CO_2-profiles at different SBT and *n*-butane inlet concentrations. Simulation: *HW1* model, 165 kg/m³ catalyst *C1*.

Tab. 19: Correlation matrix for the *HW1* model

	1	**2**	**3**	**4**	**5**	**6**	**7**	**8**	**9**	**10**	**11**	**12**	**13**
1	1.00												
2	-0.39	1.00											
3	-0.40	0.16	1.00										
4	-0.49	-0.85	-0.17	1.00									
5	0.42	-0.17	-0.91	0.20	1.00								
6	-0.10	0.08	0.04	0.03	0.03	1.00							
7	0.20	0.03	0.04	0.05	0.04	0.81	1.00						
8	0.10	0.10	0.08	0.01	0.00	0.92	0.92	1.00					
9	0.12	-0.14	0.02	0.22	0.06	0.83	0.97	0.91	1.00				
10	0.01	0.01	-0.21	0.08	0.30	0.79	0.93	0.86	0.92	1.00			
11	0.18	0.45	0.08	-0.39	-0.05	0.75	0.44	0.68	0.36	0.44	1.00		
12	0.06	0.12	0.44	-0.05	-0.46	0.71	0.44	0.65	0.46	0.23	0.67	1.00	
13	0.33	0.00	-0.02	0.10	0.06	0.27	0.29	0.47	0.33	0.30	0.32	0.29	1.00

- ***HW2*-model:**

Tab. 20: Parameter estimation results for the *HW2* model

	Parameter	Unit	Optimal Estimate	Confidence Interval (95%)
1	$E^A_{Bu,MA}$	kJ/mol	130.54	7
2	$E^A_{Bu,CO}$	kJ/mol	81.12	20
3	E^A_{Bu,CO_2}	kJ/mol	106.93	61
4	$E^A_{MA,CO}$	kJ/mol	167.92	11
5	E^A_{MA,CO_2}	kJ/mol	130.10	24
6	K_{H_2O}	bar^{-1}	68.24	15
7	$K_{Bu,1}$	bar^{-1}	145.17	25
8	$k^{ref}_{Bu,MA}$	10^{-3} mol/s/kg/$bar^{1.5}$	410.28	80
9	$k^{ref}_{Bu,CO}$	10^{-3} mol/s/kg/$bar^{1.5}$	167.90	40
10	k^{ref}_{Bu,CO_2}	10^{-3} mol/s/kg/$bar^{1.5}$	19.79	5
11	$k^{ref}_{MA,CO}$	10^{-3} mol/s/kg/$bar^{1.5}$	29.85	8
12	k^{ref}_{MA,CO_2}	10^{-3} mol/s/kg/$bar^{1.5}$	24.68	6
13	τ	-	4.619	0.5

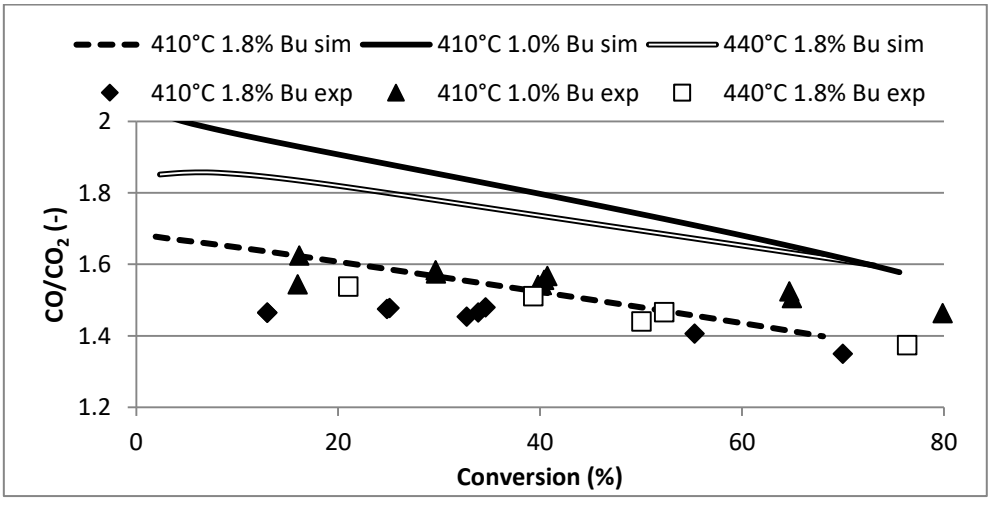

Fig. 65: Measured and simulated CO/CO_2-profiles at different SBT and *n*-butane inlet concentrations. Simulation: *HW2* model, 165 kg/m³ catalyst *C1*.

Tab. 21: Correlation matrix for the *HW2* model

	1	**2**	**3**	**4**	**5**	**6**	**7**	**8**	**9**	**10**	**11**	**12**	**13**
1	1.00												
2	-0.33	1.00											
3	-0.34	0.19	1.00										
4	0.25	0.59	-0.95	1.00									
5	0.46	0.38	0.04	0.32	1.00								
6	-0.02	0.02	0.07	0.32	0.02	1.00							
7	0.33	-0.03	0.08	0.01	0.07	0.44	1.00						
8	0.23	-0.02	0.12	-0.06	0.06	0.29	0.82	1.00					
9	0.35	0.29	0.06	-0.11	0.04	0.27	0.89	0.92	1.00				
10	0.10	-0.33	-0.08	0.36	0.04	0.97	0.59	0.43	0.45	1.00			
11	0.33	-0.16	0.09	0.01	0.25	0.33	0.83	0.96	0.91	0.48	1.00		
12	0.39	0.03	0.35	-0.40	0.01	-0.20	0.72	0.67	0.82	-0.04	0.64	1.00	
13	0.26	-0.02	0.13	-0.17	-0.30	0.26	0.79	0.54	0.74	0.40	0.45	0.72	1.00

- ***RO*-model:**

Tab. 22: Parameter estimation results for the *RO* model

	Parameter	Unit	Optimal Estimate	Confidence Interval (95%)
1	$E^A_{Bu,MA}$	kJ/mol	88.45	6
2	$E^A_{Bu,CO}$	kJ/mol	131.59	5
3	E^A_{Bu,CO_2}	kJ/mol	119.29	9
4	$E^A_{MA,CO}$	kJ/mol	91.96	99
5	E^A_{MA,CO_2}	kJ/mol	139.03	43
6	$K_{Bu,2}$	$bar^{-0.5}$	104.62	16
7	K_{H_2O}	bar^{-1}	61.85	19
8	$K_{Bu,1}$	$bar^{-0.5}$	51.80	14
9	$k^{ref}_{Bu,MA}$	10^{-3} mol/s/kg/bar	178.65	15
10	$k^{ref}_{Bu,CO}$	10^{-3} mol/s/kg/bar	66.82	7
11	k^{ref}_{Bu,CO_2}	10^{-3} mol/s/kg/bar	25.58	2
12	$k^{ref}_{MA,CO}$	10^{-3} mol/s/kg/bar	1.18	0.6
13	k^{ref}_{MA,CO_2}	10^{-3} mol/s/kg/bar	1.94	0.4
14	τ	-	3.853	0.2

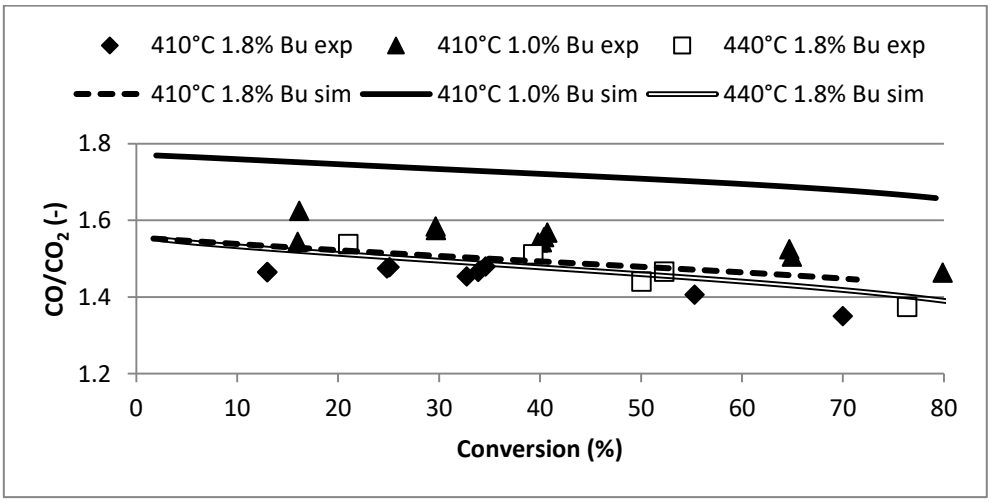

Fig. 66: Measured and simulated CO/CO_2-profiles at different SBT and *n*-butane inlet concentrations. Simulation: *RO* model, 165 kg/m³ catalyst *C1*.

Tab. 23: Correlation matrix for the *RO* model

	1	**2**	**3**	**4**	**5**	**6**	**7**	**8**	**9**	**10**	**11**	**12**	**13**	**14**
1	1.00													
2	0.13	1.00												
3	-0.13	0.19	1.00											
4	0.32	-0.72	-0.13	1.00										
5	0.29	-0.11	-0.89	0.17	1.00									
6	-0.10	-0.43	-0.18	0.19	0.09	1.00								
7	0.15	0.50	0.20	-0.18	-0.09	-0.89	1.00							
8	-0.08	-0.42	-0.15	0.17	0.08	0.80	-0.91	1.00						
9	-0.07	0.00	0.07	0.02	-0.04	0.26	-0.25	0.58	1.00					
10	0.04	-0.39	-0.10	0.30	0.07	0.82	-0.64	0.76	0.64	1.00				
11	0.14	-0.13	-0.35	0.12	0.34	0.37	-0.42	0.70	0.80	0.66	1.00			
12	-0.05	0.76	0.15	-0.67	-0.12	-0.46	0.47	-0.35	0.23	-0.36	-0.01	1.00		
13	-0.10	0.20	0.72	-0.10	-0.77	-0.19	0.25	-0.19	0.19	-0.04	-0.35	0.28	1.00	
14	0.26	0.21	0.06	0.07	0.01	-0.02	0.14	0.02	0.62	0.36	0.40	0.39	0.29	1.00

Notations

- **Latin Letters:**

Variable	Unit	Description
a	-	activity
a_P	m²/m³	specific particle surface per reactor volume
A	m²	area
A_W	-	Eisfeld correlation parameter
BET	m²/g	BET surface area
Bo	-	Bodenstein number
B_W	-	Eisfeld correlation parameter
c	mol/m³	molar concentration
c_p	J/kg/K	Mass specific heat capacity
C	-	constants
d	m	diameter
$\mathcal{D}_{i,j}$	m²/s	diffusion coefficient
e	-	error
E^A	J/mol	activation energy
f	-	fraction
h_i	J/mol	molar specific enthalpy
$\Delta_F H°$	J/mol	standard enthalpy of formation
$\Delta_R H°$	J/mol	standard enthalpy of reaction
$\dot{H}$	W/m²	heat flux by mass transport
$k_{i,j}$	various units	kinetic constant
K	Pa^{-1}	adsorption constant
l	M	mean free path
L	m	length
$\dot{M}$	kg/m²/s	mass flux
M_i	kg/mol	molecular weight
n	mol	mol number
$\dot{n}$	Mol/s	molar flow rate
N	-	correlation parameter for the radial bed conductivity

$\dot{N}$	mol/m²/s	molar flux
Nu	-	Nusselt number
p	Pa	pressure
Pe	-	Peclet number
Pr	-	Prandtl number
$\dot{Q}$	W/m²	heat flux by conduction
r	-	radial variable
r_j	mol/kg/s	reaction rate
r_P	-	radial pellet
r_W	-	radial wall
R	J/mol/K	gas constant (8.3145 J/mol/K)
Re	-	Reynolds number
R_P	m	particle radius
R_T	m	tube radius
RF_i	-	response factor
S_i	-	selectivity
S_v	m²/m³	specific surface per particle volume
Sc	-	Schmidt number
Sh	-	Sherwood number
t	s	time
T	K	temperature
u	m/s	velocity
V	m³	volume
$\dot{V}^N$	Nm³/h	normalized volumetric flow rate
x	mol/mol	molar fraction
X	-	conversion
Y_i	-	yield
z	-	axial variable

- **Greek Letters:**

Variable	Unit	Description

α	W/m²/K	heat transfer coefficient
β	m/s	mass transfer coefficient
γ	-	relative variance term
δ	-	constant variance term
Δ_v	-	diffusion volume
ε	-	void fraction
ε_{rad}	-	emissivity coefficient
η	Pa·s	viscosity
η^P	-	pore efficiency factor
θ	-	surface coverage
κ_x	-	correlation parameters for the radial bed conductivity
K_{ax}	-	correlation parameter for the dispersion coefficient
K_r	-	correlation parameter for the radial bed conductivity
λ	W/m/K	heat conductivity
μ	-	accommodation coefficient
$\nu_{i,j}$	-	stoichiometric coefficient
ξ	-	kinetic exponent
$o_{i,j}$	-	kinetic exponent
ρ	kg/m³	density
σ	-	variance
σ_{rad}	W/m²/K⁴	black body radiation coefficient ($5.67*10^{-8}$)
τ	-	tortuosity
φ	-	particle flattening coefficient
φ^{geo}	-	geometry factor
ψ	-	objective function value
Ψ_1	-	correlation parameter for the radial bed conductivity
ω	-	Eisfeld correlation parameters
Ω	-	Eisfeld correlation parameters

- **Superscript:**

ads	adsorption

act	activation
cond	conductive
conv	convective
deact	deactivation
des	desorption
disp	dispersive
eff	effective
eq	equivalent
f	fluid phase
isf	inner surface
lam	laminar
N	Normal conditions
osf	outer surface
ref	reference value
s	solid phase
SB	salt bath
sf	solid-fluid interface
ss	solid-solid interface
turb	turbulent
w	wall

- **Subscript:**

ax	axial
B	catalyst bed
cat	catalyst
fl	fluid variable
i	component number
K	Knudson
lam	laminar
j	reaction number
mix	mixture

P	particle
Ph	phosphorus
r	radial
rad	radiative
Sat	saturator
surf	sphere equivalent particle surface
turb	turbulent
T	tube
vol	sphere equivalent particle volume
W	wall
z	axial

References

[1] C. Systems, CHEMSYSTEMS PERP Progr. (2009).

[2] K. Lohbeck, H. Haferkorn, W. Fuhrmann, N. Fedtke, in Ullmann´s Encycl. Ind. Chem. (2005).

[3] J.C. Burnett, R.A. Keppel, W.D. Robinson, Catal. Today 1 (1987) 537–586.

[4] A. Neri, S. Sanchioni, Process for the Continuous Separation of Maleic Anhydride from Process Gases, US4314946 A, 1982.

[5] T.R. Felthouse, J.C. Burnett, B. Horrell, M.J. Mummey, Y. Kuo, Kirk-Othmer Encycl. Chem. Technol. (2001) 1–58.

[6] V. V Guliants, M.A. Carreon, Catal. Vol. 18, The Royal Society of Chemistry, 2005, pp. 1–45.

[7] J.K. Bartley, N.F. Dummer, G.J. Hutchings, in Metal Oxide Catalysis, Wiley-VCH Verlag GmbH & Co. KGaA, 2009.

[8] S.K. Wilkinson, M.J.H. Simmons, E.H. Stitt, X. Baucherel, M.J. Watson, J. Catal. 299 (2013) 249–260.

[9] M. Becker, J. Walden, Producing Maleic Anhydride, EP174173, 1986.

[10] G.T. Click, B.J. Barone, Steam Regeneration of Phosphorus Treated Vanadium-Phosphorus-Oxygen Catalysts, US4515899, 1985.

[11] R.C. Edwards, P.H. Kilner, C.A. Udovich, D.L. Stauffenberg, Reactivation of Phosphorus Vanadium Catalysts and Process for the Manufacture of Maleic Anhydride Catalysts Treated with Alkyl Esters of Orthophosphoric Acids in the Presence of Water, EP0123467, 1990.

[12] J.R. Ebner, Method for Improving the Performance of VPO Catalysts, WO 93/16027, 1993.

[13] M.S. Haddad, G. V Goeden, Phosphorus Addition Process for Improvement of Catalysts Suitable for Maleic Anhydride Production, US7629286, 2009.

[14] C.N. Satterfield, Mass Transfer in Heterogeneous Catalysis, Massachusetts Institute of Technology Press, Cambridge, Mass., 1970.

[15] M. Kleiber, R. Joh, Chapter Da in VDI-Wärmeatlas, Springer-Verlag, Berlin Heidelberg, 2006.

[16] M. Baerns, H. Hofmann, A. Renken, Chemische Reaktionstechnik, Georg-Thieme-Verlag, Stuttgart, 1992.

[17] C.A. Leon y Leon, Adv. Colloid Interface Sci. 76-77 (1998) 341–372.

[18] N.F. Dummer, J.K. Bartley, G.J. Hutchings, in Advanced Catalysis 54, Elsevier Inc., 2011, pp. 189–239.

[19] G. Centi, F. Trifirò, J.R. Ebner, V.M. Franchetti, Chem. Rev. 88 (1988) 55–80.

[20] B. Kubias, U. Rodemerck, H.W. Zanthoff, M. Meisel, Catal. Today 32 (1996) 243–253.

[21] W.M. Brandstädter, B. Kraushaar-Czarnetzki, Ind. Eng. Chem. Res. 44 (2005) 5550–5559.

[22] M.-J. Cheng, W.A.G. Goddard, J. Am. Chem. Soc. 135 (2013) 4600–4603.

[23] W.M. Brandstädter, Partial Oxidation of Raffinate II and other Mixtures of n-Butane and n-Butenes to Maleic Anhydride in a Fixed-Bed Reactor, PhD Thesis, Universität Karlsruhe, 2007.

[24] Z. Xue, G.L. Schrader, J. Pysical Chem. B 103 (1999) 9459–9467.

[25] M. Dente, S. Pierucci, E. Tronconi, M. Cecchini, F. Ghelfi, Chem. Eng. Sci. 58 (2003) 643–648.

[26] X.F. Huang, C.Y. Li, B.H. Chen, Am. Inst. Chem. Eng. J. 48 (2002) 846–855.

[27] S. Hess, H. Freund, M.A. Liauw, G. Emig, Stud. Surf. Sci. Catal. 133 (2001) 205–210.

[28] K. Uihlein, Butanoxidation an VPO-Wirbelschichtkatalysatoren, PhD Thesis, Universität Stuttgart, 1993.

[29] D. Wang, M. a Barteau, J. Catal. 197 (2001) 17–25.

[30] D. Wang, M.A. Barteau, Appl. Catal. A Gen. 223 (2002) 205–214.

[31] S.K. Bej, M.S. Rao, Ind. Eng. Chem. Res. 31 (1992) 2075–2079.

[32] J.S. Buchanan, S. Sundaresan, Appl. Catal. 26 (1986) 211–226.

[33] R.K. Sharma, D.L. Cresswell, E.J. Newson, Am. Inst. Chem. Eng. J. 37 (1991) 39–47.

[34] C. Becker, Katalytische Wandreaktorkonzepte Für MSA-Synthese und Methanol-Dampfreformierung, PhD Thesis, Universität Stuttgart, 2002.

[35] G. Centi, G. Fornasari, F. Trifiro, Ind. Eng. Chem. Prod. Res. Dev. 24 (1985) 32–37.

[36] J. Gascón, R. Valenciano, C. Téllez, J. Herguido, M. Menéndez, Chem. Eng. Sci. 61 (2006) 6385–6394.

[37] P. Schneider, G. Emig, H. Hofmann, Ind. Eng. Chem. Res. 26 (1987) 2236–2241.

[38] R.M. Contractor, A.W. Sleight, Catal. Today 3 (1988) 175–184.

[39] F. Cavani, D. De Santi, S. Luciani, A. Löfberg, E. Bordes-Richard, C. Cortelli, R. Leanza, Appl. Catal. A Gen. 376 (2010) 66–75.

[40] F. Cavani, S. Luciani, E.D. Esposti, C. Cortelli, R. Leanza, Chem. A Eur. J. 16 (2010) 1646–1655.

[41] E.W. Arnold, S. Sundaresan, Appl. Catal. 41 (1988) 225–239.

[42] G.W. Coulston, S.R. Bare, H. Kung, K. Birkeland, G.K. Bethke, R. Harlow, N. Herron, P.L. Lee, Science 275 (1997) 191–1933.

[43] M.J. Lorences, G.S. Patience, F. V. Díez, J. Coca, Appl. Catal. A Gen. 263 (2004) 193–202.

[44] N. Emberger, Zur Reaktionskinetik der Selektivoxidation von n-Butan an einem Technischen (VO)2P2O7-Katalysator, PhD Thesis, Universität Magdeburg, 2005.

[45] R.M. Contractor, H.S. Horowitz, G.M. Sisler, E. Bordes, Catal. Today 37 (1997) 51–57.

[46] R. Schlögl, Top. Catal. 54 (2011) 627–638.

[47] U. Rodemerck, B. Kubias, H.W. Zanthoff, G.U. Wolf, M. Baerns, Appl. Catal. A Gen. 153 (1997) 217–231.

[48] P.D. M. Abon, K.E. Bere, Catal. Today 33 (1997) 15–23.

[49] R.J. Berger, J. Pérez-Ramírez, F. Kapteijn, J. a. Moulijn, Chem. Eng. J. 90 (2002) 173–183.

[50] R.J. Berger, J. Pérez-Ramírez, F. Kapteijn, J.A. Moulijn, Appl. Catal. A Gen. 227 (2002) 321–333.

[51] M. Lopez Granados, J.L.G. Fierro, F. Cavani, A. Colombo, F. Giuntoli, F. Trifiro, Catal. Today 40 (1998) 251–261.

[52] T.P. Moser, R.W. Wenig, Schrader, Appl. Catal. 34 (1987) 39–48.

[53] L.M. Cornaglia, E.A. Lombardo, Appl. Catal. A Gen. 127 (1995) 125–138.

[54] O. Levenspiel, Chemical Reaction Engineering, John Wiley & Sons, Inc., New York, 1999.

[55] G.F. Froment, K.B. Bischoff, Chemical Reactor Analysis and Design, John Wiley & Sons, New York, 1990.

[56] E. Tsotsas, Chapter Dee in VDI-Wärmeatlas, Springer-Verlag, Berlin Heidelberg, 2006.

[57] V. Gnielinski, Chapter Gj in VDI-Wärmeatlas, Springer-Verlag, Berlin Heidelberg, 2006.

[58] R. Guettel, T. Turek, Chem. Eng. Sci. 65 (2010) 1644–1654.

[59] J. Frey, C. Lieder, T. Schölkopf, T. Schleid, U. Nieken, E. Klemm, M. Hunger, J. Catal. 272 (2010) 131–139.

[60] J. Volta, Catal. Today 32 (1996) 29–36.

[61] G. Koyano, T. Okuhara, M. Misono, J. Am. Chem. Soc. 120 (1998) 767–774.

[62] G. Koyano, T. Saito, M. Misono, J. Mol. Catal. A Chem. 155 (2000) 31–41.

[63] R.W. Wenig, G.L. Schrader, J. Pysical Chem. 91 (1987) 5674–5680.

[64] H. Bluhm, M. Hävecker, E. Kleimenov, A. Knop-Gericke, A. Liskowski, R. Schlögl, D.S. Su, Top. Catal. 23 (2003) 99–107.

[65] F. Richter, H. Papp, T. Götze, G.U. Wolf, B. Kubias, Surf. Interface Anal. 26 (1998) 736–741.

[66] F. Richter, H. Papp, G.U. Wolf, T. Götze, B. Kubias, Fresenius J. Anal. Chem. 365 (1999) 150–153.

[67] E.A.L. L.M. Cornaglia, Appl. Catal. A Gen. 127 (1995) 125–138.

[68] R.M. Blanco, A. Shekari, S.G. Carrazán, E. Bordes-Richard, G.S. Patience, P. Ruiz, Catal. Today 203 (2013) 48–52.

[69] Z. Xue, G.L. Schrader, J. Catal. 184 (1999) 87–104.

[70] H.W. Zanthoff, M. Sananes-Schultz, S.A. Buchholz, U. Rodemerck, B. Kubias, M. Baerns, Appl. Catal. A Gen. 172 (1998) 49–58.

[71] http://webbook.nist.gov/chemistry/ (2011).

[72] M. Abon, K.E. Bere, A. Tuel, P. Delichere, J. Catal. 156 (1995) 28–36.

[73] G.S. Patience, R.E. Bockrath, J.D. Sullivan, H.S. Horowitz, Ind. Eng. Chem. Res. 46 (2007) 4374–4381.

[74] D.J. Thompson, M.O. Fanning, B.K. Hodnett, J. Mol. Catal. A Chem. 198 (2003) 125–137.

[75] M. Willinger, D. Su, R. Schlögl, Phys. Rev. B 71 (2005) 155118.

[76] F. Girgsdies, T. Ressler, R. Schlögl, W.S. Dong, J.K. Bartley, G.J. Hutchings, Solid State Sci. 8 (2006) 807–812.

[77] F. Girgsdies, M. Schneider, A. Brückner, T. Ressler, R. Schlögl, Solid State Sci. 11 (2009) 1258–1264.

[78] M.G. Willinger, Electronic Structure of Vanadium Phosphorus Oxides, PhD Thesis, Technische Universität Berlin, 2005.

[79] U. Rodemerck, B. Kubias, H.W. Zanthoff, M. Baerns, Appl. Catal. A Gen. 153 (1997) 203–216.

[80] V. V Guliants, J.B. Benziger, S. Sundaresan, I.E. Wachs, J.M. Jehng, J.E. Roberts, Catal. Today 28 (1996) 275–295.

[81] T. Okuhara, M. Misono, Catal. Today 16 (1993) 61–67.

[82] F.K. Hannour, A. Martin, B. Kubias, B. Lücke, E. Bordes, P. Courtine, Catal. Today 40 (1998) 263–272.

[83] F. Castellino, S.B. Rasmussen, A.D. Jensen, J.E. Johnson, R. Fehrmann, Appl. Catal. B Environ. 83 (2008) 110–122.

[84] G. Mestl, T. Ilkenhans, D. Spielbauer, M. Dieterle, O. Timpe, J. Kröhnert, F. Jentoft, H. Knözinger, R. Schlögl, Appl. Catal. A Gen. 210 (2001) 13–34.

[85] S. Ergun, Chem. Eng. Prog. 48 (1952) 89–94.

[86] B. Eisfeld, K. Schnitzlein, Chem. Eng. Sci. 56 (2001) 4321–4329.

[87] E. Tsotsas, Chemie Ing. Tech. 72 (2000) 313–321.

[88] J.N. Papageorgiou, G.F. Froment, Chem. Eng. Sci. 50 (1995) 3043–3056.

[89] O. Bey, G. Eigenberger, Chem. Eng. Sci. 52 (1997) 1365–1376.

[90] M. Bauer, R. Adler, Chemie Ing. Tech. 74 (2002) 804–808.

[91] H. Hofmann, Chemie Ing. Tech. 51 (1979) 257–265.

[92] R.J. Wijngaarden, K.R. Westerterp, Chem. Eng. Sci. 48 (1993) 1273–1280.

[93] R. Marx, Kinetics of the Selective Oxidation of O-Xylene to Phthalic Anhydride, PhD Thesis, Technische Universität Clausthal, 2013.

[94] E. Tsotsas, Chapter Mh in VDI-Wärmeatlas, Springer-Verlag, Berlin Heidelberg, 2006.

[95] R.J. Wijngaarden, K.R. Westerterp, Chem. Eng. Sci. 44 (1989) 1653–1663.

[96] T. Daszkovski, G. Eigenberger, Chem. Eng. Sci. 47 (1992) 2245–2250.

[97] J. Diedenhoven, A. Reitzmann, G. Mestl, T. Turek, Chemie Ing. Tech. 84 (2012) 517–523.

[98] Y. Cheng, F. Lopez-Isunza, T. Mongkhonsi, L. Kershenbaum, Appl. Catal. A Gen. 106 (1993) 193–199.

[99] Y.S. Cheng, T. Mongkhonsi, L.S. Kershenbaum, Chem. Eng. Sci. 51 (1996) 1909–1918.

[100] A.I. Anastasov, Chem. Eng. Process. 42 (2003) 449–460.

[101] E. Riedel, Anorganische Chemie, Walter de Gruyter GmbH, Berlin/Boston, 2004.

[102] D. Wen, Y. Ding, Chem. Eng. Sci. 61 (2006) 3532–3542.

[103] G.F. Froment, Chemie Ing. Tech. 46 (1974) 374–386.

List of Figures

List of Tables